

An Updated High Precision Measurement of the Neutral Pion Lifetime via the Primakoff Effect

December 10, 2007

THIS ALL NEEDS TO BE UPDATED

Bracilians, new Kharkov people, Bitao

A. Ahmidouch, S. Danagoulian (spokesperson),

A. Gasparian (spokesperson and contact person), C. Jackson, S. Mtingwa, J. Underwood
North Carolina A&T State University; Greensboro, NC

E. Clinton, R. Hicks, D. Lawrence, R. Miskimen (spokesperson)
University of Massachusetts, Amherst, MA

D. Dale (spokesperson), M. Gabrielyan, B. Hu, W. Korsch, A. Teymuracyan, P. Zolnierczuk
University of Kentucky; Lexington, KY

A. Afanasev, E. Chudakoff, H. Egiyan, R. Ent, V. Gyurjyan, M. Ito, J.P. Chen,
Y. Sharabian, E. Smith
Thomas Jefferson National Accelerator Facility; Newport News, VA

K. Baker, M. Christy, J. Goity, P. Gueye, C. Keppel, L. Tang, L. Yuan
Hampton University; Hampton, VA

L. Gan, M. Alexanian, T. Black
University of North Carolina at Wilmington; Wilmington, NC

A.M. Bernstein, D. Hasell, S. Kowalski, R. Suleiman
Massachusetts Institute of Technology; Cambridge, MA

D. Sober, H. Crannell, R. Hakobyan
The Catholic University of America; Washington, DC

J. Ball, M. Dugger, E. Pasyuk, B.G. Ritchie
Arizona State University; Tempe, AZ

R. Minehart, B. Stevens
University of Virginia; Charlottesville, VA

A. Asratyan, O. Chernyshov, G. Davidenko, A. Dolgolenko, G. Dzyubenko, A. Evdokimov,
V. Goryachev, A. Kamenskii, M. Kubantsev, I. Larin, V. Matveev, V. Semyachkin,
A. Sitnikov, V. Verebryusov, V. Vishnyakov

Institute for Theoretical and Experimental Physics, Moscow, Russia

Yu. Goncharenko, V. Kubarovsky, A. Meschanin, L. Soloviev, A. Vasiliev

Institute for High Energy Physics, Protvino, Russia

M. Khandaker, V. Punjabi, C. Salgado

Norfolk State University, Norfolk, VA

A. Glamadzin, A. Omelaenko, +++++++

Kharkov Institute of Physics and Technology, Kharkov, Ukraine

P.L. Cole

University of Texas at El Paso, El Paso, TX

A. Nathan

University of Illinois, Urbana, IL

C. Li, Z. Liu, S. Lu, J. Yuan, J. Zhou, S. Zhou, X. Zhu

Chinese Institute of Atomic Energy, Beijing, China

J. He

Institute of High Energy Physics, Chinese Academy of Sciences, Beijing, China

W. Briscoe

George Washington University, Washington, DC

I. Achnuryan, S. Gevorgyan, A. Margaryan, K. Egiyan,

H. Voskanyan, A. Ketikyan, A. Shahinyan, A. Petrosyan

Yerevan Physics Institute, Yerevan, Armenia

B. Milbrath

Eastern Kentucky University, Richmond, KY

A.I. Fix, V.A. Tryaschev

Tomsk Polytechnical University, Tomsk, Russia

M. Elaasar

Southern University at New Orleans, New Orleans, LA

Contents

1	Motivation	6
2	Theoretical Developments	6
3	Neutral Pion Photoproduction via the Primakoff Effect	8
4	Instrumentation and Experimental Techniques – Current Status and Planned Upgrades	12
4.1	Targets	12
4.2	The neutral pion detector	12
4.2.1	Charged particle veto detector	12
4.2.2	The hybrid electromagnetic calorimeter <i>HYCAL</i>	17
4.3	The Calorimeter Frame and Transporter	20
4.4	Performance of the Calorimeter	21
4.5	HYCAL Gain Monitoring System	23
4.6	Luminosity monitoring	24
4.6.1	Absolute tagging ratios	27
4.6.2	Relative tagging ratios measured with pair production	29
4.7	Photon beam position monitor	30
4.8	Data acquisition and trigger	31
4.8.1	Trigger	32
5	Preliminary Results from the 2004 Run	33
5.1	π^0 Photoproduction Cross Section Extraction	33
5.2	Theoretical Calculations on Nuclear Form Factors and Backgrounds	35
5.3	Determination of $\Gamma_{\pi^0 \rightarrow \gamma\gamma}$	35
5.4	Results of high precision calibration experiments	35
5.4.1	The absolute cross section for pair production	35
5.4.2	Absolute cross section for electron Compton scattering	58
6	Plans for a future run	65
6.1	New improvements	65
6.2	Run time and schedule	65
7	Summary	65
8	Appendix I: Previous Experiments	68
8.1	The direct method	68
8.2	Measurements using $\gamma\gamma$ collisions	68
8.3	Measurements using the Primakoff effect	69
9	Appendix II: Systematic Effects Relating to Photon Flux Determination	70
9.1	Effects of incident electron beam intensity on absolute tagging ratios	70
9.2	Effects of collimator size	70

9.3	Effects of collimator position misalignment	70
9.4	Effects of HyCal scraping due to beam mis-steering (uncollimated beam) . .	72
9.5	Long and short term reproducibility with uncollimated beam	75
9.6	Effects of the PS dipole field with collimated beam	77
9.7	Absorption in the target	78
10	Appendix III: Target thickness determination	79

Abstract

The PrimEx Collaboration has proposed to perform a high precision measurement on the two photon decay width of the neutral pion ($\Gamma_{\pi^0 \rightarrow \gamma\gamma}$). This measurement will provide a stringent test of the predictions of the U(1) axial anomaly in quantum chromodynamics. The first experimental data set was collected in 2004. A new level of experimental precision has been achieved by using a high intensity and high resolution photon tagging facility in Hall B of Jefferson Lab, and by developing and constructing a state-of-the-art, high resolution electromagnetic calorimeter. A preliminary result on the π^0 lifetime with a precision of $\sim 3\%$ was released at the American Physical Society April meeting in 2007 through an invited presentation as well as at an American Institute of Physics press conference. The desired precision on this measurement is driven by the precision of recently available theoretical calculations performed both in the context of chiral perturbation theory and the QCD sum rule approach. Here, we discuss the analysis status on the existing data and the improvement which can be made with a future run, and thereby request an extension of the π^0 lifetime measurement from PAC 33 to reach the ultimate goal of $\simeq 1.4\%$ accuracy.

1 Motivation

An effect of color confinement in quantum chromodynamics(QCD) is that traditional perturbation theory breaks down at large distances and low energies. A quantitative understanding of the strong interaction in this region remains one of the greatest intellectual challenges in physics. Symmetries of QCD in the chiral limit (massless quark limit) provide a promising framework for resolving this problem. As the lightest particle in the hadron spectrum, the neutral pion represents the most sensitive platform to study fundamental symmetry issues in quantum chromodynamics at low energy. Spontaneous chiral symmetry breaking gives birth to the π^0 as one of the Goldstone particles and the chiral axial anomaly primarily determines the π^0 lifetime. As such, a precision measurement of the lifetime of the π^0 will provide a fundamental test of QCD at the confinement scale.

2 Theoretical Developments

The two-photon decay mode of the π^0 reveals one of the most profound symmetry issues in quantum chromodynamics, namely, the explicit breaking of a classical symmetry by the quantum fluctuations of the quark fields coupling to a gauge field[1]. This phenomenon, called anomalous symmetry breaking, is of pure quantum mechanical origin. In QCD, there are several observable phenomena that originate from anomalies. One is connected with the couplings of the quarks to the gluons. This is the so called axial anomaly by which the conservation of the axial U(1) symmetry of the classical Lagrangian of QCD is broken even in the limit where two or more quarks are massless, and the so called anomalous divergence of the corresponding axial-vector current becomes proportional to the product $\vec{E}^a \cdot \vec{B}^a$ of the chromo-electric and chromo-magnetic fields. The axial anomaly of interest to us involves the corresponding coupling of the quarks to photons[2]. In the limit of exact isospin symmetry, the π^0 couples only to the isotriplet axial-vector current $\bar{q} I_3 \gamma_\mu \gamma_5 q$, where $q = (u, d)$, and I_3 is the third isospin generator. If we limit ourselves to two quark flavors, the electromagnetic current is given by $\bar{q}(1/6 + I_3/2)\gamma_\mu q$. When coupling to the photon, the isosinglet and isotriplet components of the electromagnetic current lead to an anomaly that explicitly breaks the symmetry associated with the axial-vector current $\bar{q} I_3 \gamma_\mu \gamma_5 q$, and this in turn directly affects the coupling of the π^0 to two photons. The conservation of the axial U(1) current, to which the η' meson couples, as well as the $\bar{q} \frac{1}{2} \lambda_8 \gamma_\mu \gamma_5 q$, to which the η meson couples, are similarly affected by the electromagnetic field.

In the limit of vanishing quark masses, the anomaly leads to the $\pi^0 \rightarrow \gamma\gamma$ decay amplitude [1, 2]:

$$\mathcal{A}(\pi^0 \rightarrow \gamma\gamma) = \frac{\alpha_{em}}{4\pi F_\pi} \epsilon_{\mu\nu\rho\sigma} k^\mu k'^\nu \epsilon^{\rho\sigma}, \quad (1)$$

or the reduced amplitude,

$$A_{\gamma\gamma} = \frac{\alpha_{em}}{\pi F_\pi} = 2.513 \cdot 10^{-2} GeV^{-1} \quad (2)$$

where $F_\pi = 92.42 \pm 0.25 MeV$ [3] is the pion decay constant, and k and ϵ are respectively photon momenta and polarization vectors.

The width of the $\pi^0 \rightarrow \gamma\gamma$ decay predicted by this amplitude is

$$\Gamma = M_\pi^3 \frac{|A_{\gamma\gamma}|^2}{64\pi} = 7.725 \pm 0.044 \text{ eV}, \quad (3)$$

with a 0.6% uncertainty due to the experimental error in F_π . The crucial aspect of this expression is that it has no free parameters that need to be determined phenomenologically. In addition, since the mass of the π^0 is the smallest in the hadron spectrum, higher order corrections to this prediction are small and can be calculated with a sub-percent accuracy.

The current experimental value is 7.84 ± 0.56 eV[3] and is in good agreement with the predicted value with the chiral limit amplitude. This number is an average of several experiments[3] which are discussed in Appendix I. The error of 7% quoted by the Particle Data Book is most likely too low since each of the quoted experiments appears to have understated their errors and also, as can be seen in figure 1, from the much larger dispersion between the different measurements. Even at the 7% level, the accuracy is not sufficient for a test of such a fundamental quantity, and in particular for the new calculations which take the finite quark masses into account. The level of precision of $\simeq 1.4\%$, which is the goal of *PrimEx*, will satisfy these requirements.

The decay amplitude given above is exact only in the chiral limit, i.e., when the u - and d -quark masses vanish. In this case, the anomaly is saturated by the π^0 pole and the result for the decay amplitude given above is exact. However, the current-quark masses are non-vanishing and are approximately $m_u \simeq 4 \text{ MeV}$ and $m_d \simeq 7 \text{ MeV}$ [6]. There are two sources of corrections due to this explicit breaking of chiral symmetry. The first and dominant one results from a combined effect that involves the corrections to the decay constants (because of isospin breaking there is a decay constant matrix in the subspace of the π^0 , η and η') and an isospin breaking mixing that gives the physical π^0 a non-vanishing component along the pure $U(3)$ states η and η' . In the absence of isospin breaking this source of chiral symmetry breaking boils down to merely replacing the value of F_π in the chiral limit by the measured value determined from π^+ decay[4, 5]. The second source of corrections is due to the fact that the saturation of the matrix elements of the divergence of the axial current also involves excited mesonic states when chiral symmetry is broken by quark masses. This effect is estimated using QCD sum rules[11] and turns out to be much smaller than the mixing effects.

Stimulated by the *PrimEx* project, several new theoretical calculations have been published in recent years, and are shown in figure 1. The first two independent calculations of the chiral corrections have been performed in the combined framework of chiral perturbation theory (ChPT) and the $1/N_c$ expansion up to $\mathcal{O}(p^6)$ and $\mathcal{O}(p^4 \times 1/N_c)$ in the decay amplitude[7][8]. The η' is explicitly included in the analysis as it plays as important a role as the η in the mixing effects. It was found that the decay width is enhanced by about 4% with respect to the value stated in equation (1). This enhancement is almost entirely due to the mixing effects. The result of this next-to-leading order analysis is $\Gamma_{\pi^0 \rightarrow \gamma\gamma} = 8.10$ eV with an estimated uncertainty of less than 1%. Another theoretical calculation based on QCD sum rules[9], also inspired by the *PrimEx* experiment, has recently been published with a theoretical uncertainty less than 1.5%. Here, the only input parameter to the calculation is the eta width. The measurement of the decay width of π^0 with a comparable precision will provide an important test of the fundamental QCD predictions.

The quantity $1/R = (m_d - m_u)/m_s$ which enters into these calculations is of considerable interest, since it characterizes the size of the $SU(2)$ breaking in the quark mass matrix. However, it is notoriously difficult to extract reliably. The standard procedure is to utilize the kaon mass difference, and to subtract the electromagnetic component of the mass difference using Dashen's theorem (kaon and pion EM mass shifts are identical in the chiral limit). When this procedure is followed one obtains $R \simeq 42$. Explicit calculations of the kaon-pion EM mass difference by Donoghue, Holstein, and Wyler and by Bijmns show a significant breaking of Dashen's theorem, and they conclude that $m_d - m_u$ is larger than what is given by the usual analysis, with $R \simeq 30$. There is also evidence from the $\eta \rightarrow 3\pi$ reaction that $m_d - m_u$ is underestimated by the conventional Dashen's theorem analysis. An important feature of the $\pi^0 \rightarrow \gamma\gamma$ decay rate is that it depends upon R in a known way, and that a precise measurement of the lifetime, as proposed in the *PrimEx* experiment, could provide a useful and independent value for this interesting and important parameter.

The proposed measurement at the $\simeq 1.4\%$ accuracy level fills an important experimental gap, namely a precision verification of the predictions of the axial anomaly and the chiral corrections to the decay rate. The so-called "direct" method of determination of $\Gamma_{\pi^0 \rightarrow \gamma\gamma}$ lies below the prediction of the axial anomaly[14] and is therefore even more in disagreement with the new predictions which are based on both next-to-leading order chiral theory[7][8] and QCD sum rules[9]. This makes the *PrimEx* experiment even more compelling. It is indeed extremely important that effects of chiral symmetry breaking by the u - and d -quark masses, which can be rather precisely predicted theoretically, can actually be experimentally tested thanks to the projected level of precision of *PrimEx*. This would indeed be one of the most precise tests of fundamental aspects of QCD, namely anomalies and chiral symmetry breaking by quark masses, ever achieved.

3 Neutral Pion Photoproduction via the Primakoff Effect

We plan to use quasi-monochromatic photons of energy 4.6-5.7 GeV from the Hall B photon tagging facility to measure the absolute cross section of small angle π^0 photoproduction from the Coulomb field of complex nuclei. The invariant mass and angle of the pion will be reconstructed by detecting the π^0 decay photons from the $\pi^0 \rightarrow \gamma\gamma$ reaction.

For unpolarized photons, the Primakoff cross section is given by[42]:

$$\frac{d^3\sigma_P}{d\Omega} = \Gamma_{\gamma\gamma} \frac{8\alpha Z^2 \beta^3 E^4}{m^3 Q^4} |F_{e.m.}(Q)|^2 \sin^2\theta_\pi \quad (4)$$

where $\Gamma_{\gamma\gamma}$ is the pion decay width, Z is the atomic number, m , β , θ_π are the mass, velocity and production angle of the pion, E is the energy of incoming photon, Q is the momentum transfer to the nucleus, and $F_{e.m.}(Q)$ is the nuclear electromagnetic form factor, corrected for final state interactions of the outgoing pion.

As the Primakoff effect is not the only mechanism for pion photoproduction at high energies, some care must be taken to isolate it from competing processes. In particular, the full cross section is given by:

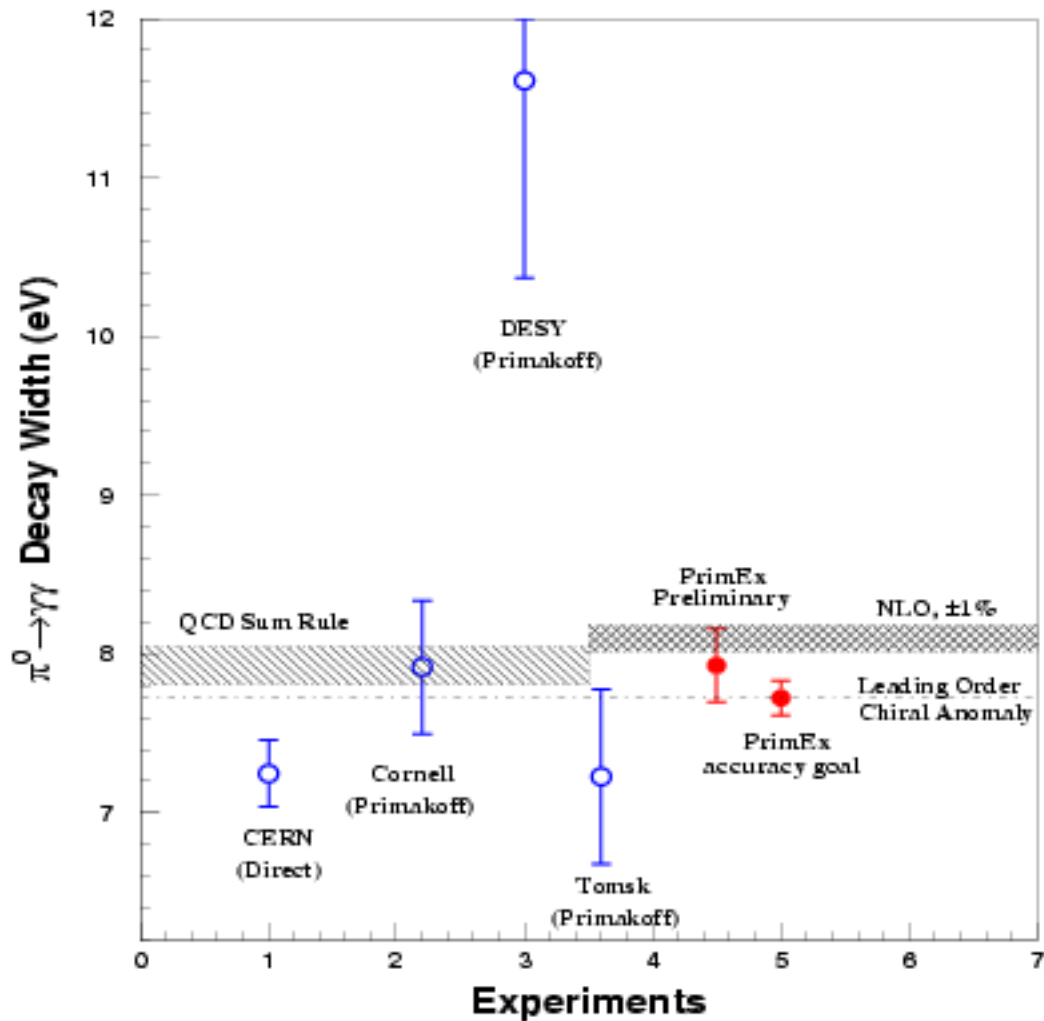


Figure 1: $\pi^0 \rightarrow \gamma\gamma$ decay width in eV. The dashed horizontal line is the leading order prediction of the axial anomaly (equation 3)[1, 2]. The left hand side shaded band is the recent QCD sum rule prediction and the right hand side shaded band is the next-to-leading order chiral theory predictions. The experimental results with errors are for : (1) the direct method[14]; (2, 3, 4) the Primakoff method [43, 42, 18]; (5) the preliminary result from the first *PrimEx* data set; (6) the expected error for the final goal of the *PrimEx* experiment, arbitrarily plotted to agree with the leading order prediction.

$$\frac{d^3\sigma}{d\Omega_\pi} = \frac{d\sigma_P}{d\Omega} + \frac{d\sigma_C}{d\Omega} + \frac{d\sigma_I}{d\Omega} + 2 \cdot \sqrt{\frac{d\sigma_P}{d\Omega} \cdot \frac{d\sigma_C}{d\Omega}} \cos(\phi_1 + \phi_2) \quad (5)$$

where the Primakoff cross section, $\frac{d\sigma_P}{d\Omega}$, is given by equation (4). The nuclear coherent cross section is given by:

$$\frac{d\sigma_C}{d\Omega} = C \cdot A^2 |F_N(Q)|^2 \sin^2\theta_\pi \quad (6)$$

and the incoherent cross section is:

$$\frac{d\sigma_I}{d\Omega} = \xi A(1 - G(Q)) \frac{d\sigma_H}{d\Omega} \quad (7)$$

where A is the nucleon number, $C \sin^2\theta_\pi$ is the square of the isospin and spin independent part of the neutral meson photoproduction amplitude on a single nucleon, $|F_N(Q)|$ is the form factor for the nuclear matter distribution in the nucleus, (corrected for final state interactions of the outgoing pion), ξ is the absorption factor of the incoherently produced pions, $1 - G(Q)$ is a factor which reduces the cross section at small momentum transfer due to the Pauli exclusion principle, and $\frac{d\sigma_H}{d\Omega}$ is the π^0 photoproduction cross section on a single nucleon. The relative phase between the Primakoff and nuclear coherent amplitudes without final state interactions is given by ϕ_1 , and the phase shift of the outgoing pion due to final state interactions is given by ϕ_2 .

Kinematical considerations enable one to separate the Primakoff effect from other photopion production mechanisms. The Primakoff cross section is zero for pions emitted along the incident photon direction, has a sharp maximum at an angle $\theta_\pi \sim m_\pi^2/2E_\gamma^2$, and falls rapidly to zero at larger angles. It is proportional to Z^2 , and its peak value is roughly proportional to E^4 . The nuclear coherent cross section for spin zero nuclei is also zero in the forward direction, but has a broad maximum outside the angular region of the Primakoff effect, and falls at larger angles as shown in figure 2, where the amplitudes are normalized to the Cornell data[43], and distortion effects are included. The angular dependence of Primakoff signal is different from the background processes, allowing $\Gamma(\pi^0 \rightarrow \gamma\gamma)$ to be extracted from a fit to the angular distribution of photo-produced π^0 . Measurements of the nuclear effects at larger angles are necessary to determine the unknown parameters in the production mechanism and thus make an empirical determination of the nuclear contribution in the Primakoff peak region. Consequently, this experiment requires a π^0 detector with good angular resolution to eliminate nuclear coherent production, and good energy resolution in the decay photon detection will enable an invariant mass cut to suppress multi-photon backgrounds.

The production of neutral pions via the Primakoff effect is primarily an electromagnetic phenomenon and, therefore, can be accurately calculated. The main features of the Primakoff effect listed above will be used to test the accuracy of our data: (1) We will take data with sufficient angular resolution to check the shape of the Primakoff peak after the coherent nuclear and nuclear-Primakoff interference amplitudes, which will be determined empirically by larger angle data, have been subtracted; (2) two spin zero targets (^{12}C , ^{208}Pb) will be used. These have form factors which have been well studied by electron scattering experiments, and can be used to test the Z^2 dependence of the cross section; and (3) the E^4 dependence of the peak cross section will be measured in the energy range from 4.6 to 5.7

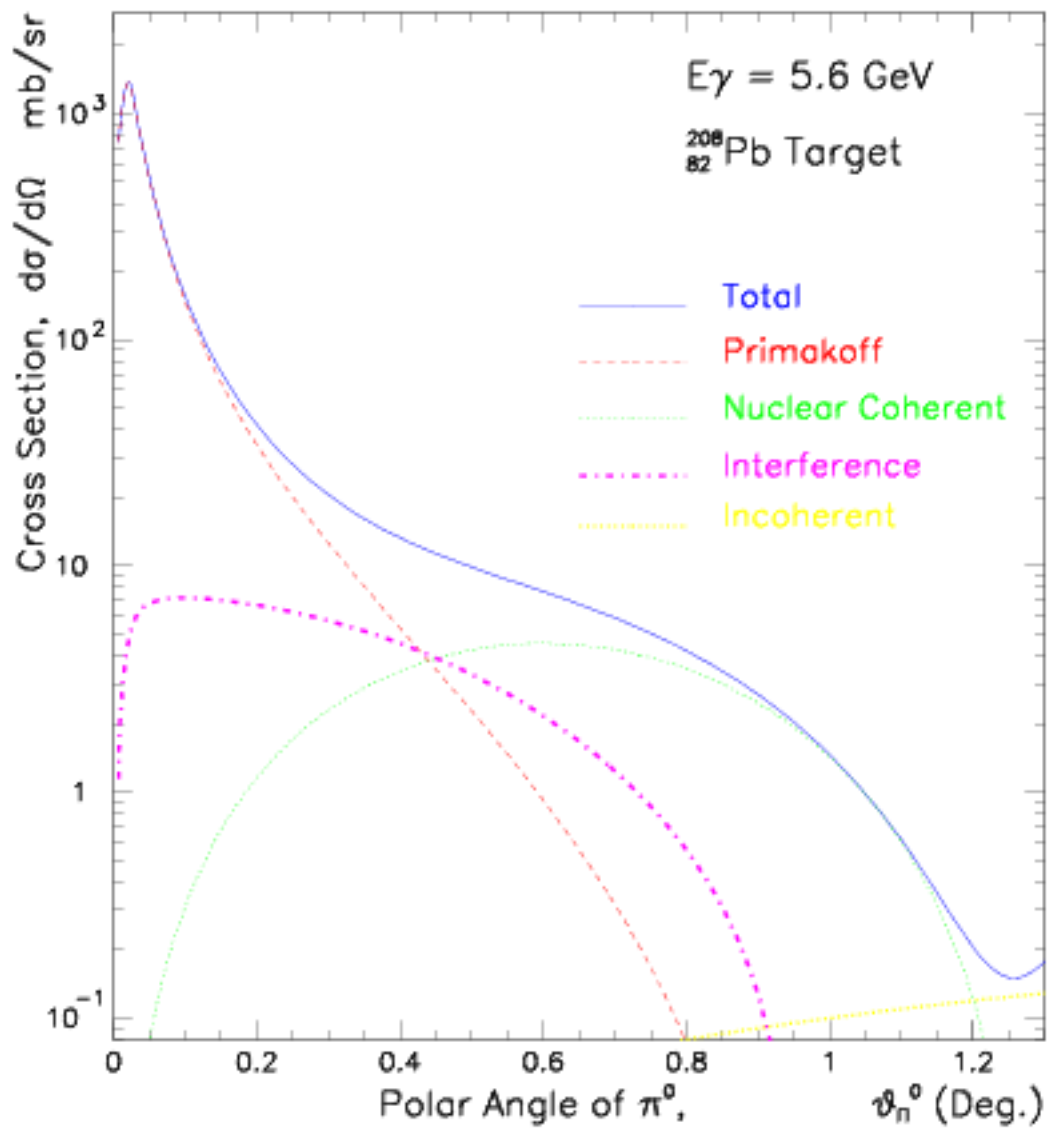


Figure 2: Angular behavior of the electromagnetic and nuclear π^0 photoproduction cross sections for ^{208}Pb in the 6.0 GeV energy range.

GeV. The study of the Primakoff peak as a function of these three variables should add a great deal of confidence to the measurement, and can be used to empirically determine the systematic errors.

We submitted our first proposal(E-99-014) to PAC15 in Dec 1998. It was approved by PAC15 and reconfirmed in jeopardy review later by PAC22 with an "A" rating. The first experiment on two targets (^{12}C and ^{208}Pb) was performed in 2004. The preliminary result demonstrates that we are able to control the systematic errors with designed precision and more beam time is needed to reach the proposed goal of $\sim 1.4\%$ accuracy. In the following sections, we will describe what we have achieved in the first *PrimEx* experiment and what we can improve in the future runs.

4 Instrumentation and Experimental Techniques – Current Status and Planned Upgrades

With strong support from Jefferson Lab and a \$1 million Major Research Instrumentation award (MRI, PHY-0079840) from the National Science Foundation, the *PrimEx* experimental setup was developed and constructed (See figure 3). The primary experimental equipment includes: (1) the existing Hall B photon tagger for tagged photon beam; and new development of (2) 5% radiation length solid π^0 production targets (^{12}C , ^{120}Sn , and ^{208}Pb); (3) a pair production luminosity monitor located just downstream of the π^0 production target; (4) a $1\text{m} \times 1\text{m}$ high resolution hybrid calorimeter (HYCAL) with a plastic scintillator charged particle veto for detecting π^0 decay photons; (5) a scintillator fiber based photon beam profile and position detector located behind HYCAL for on-line beam position monitor. Here, we describe the performance of each equipment during the first *PrimEx* run in 2004.

4.1 Targets

We propose to use two targets in this experiment, ^{12}C and ^{208}Pb . The carbon target is approximately 380 mil thick (5% R.L.) and uses Highly Ordered/Oriented Pyrolytic Graphite (HOPG) as the target material. The lead target is a rolled metal target approximately 12 mils thick (5% R.L.) and uses 99% enriched ^{208}Pb as the target material. The uncertainties in the effective areal densities of the carbon and lead targets are 0.05% and 0.43%, respectively. Both targets were utilized in the first *PrimEx* run. The methodology for mapping the effective areal densities of the targets (*atoms/cm²*) and the estimated errors are described in an Appendix to this proposal.

4.2 The neutral pion detector

4.2.1 Charged particle veto detector

The veto counter system consists of twelve scintillation paddles with dimensions $120 \times 10 \times 0.5\text{cm}^3$ which cover the front face of the HYCAL calorimeter. The purpose of the veto counters is to reject charged particle backgrounds incident on the calorimeter. They are designed to have good efficiency for charged particle detection, and be sufficiently thin so

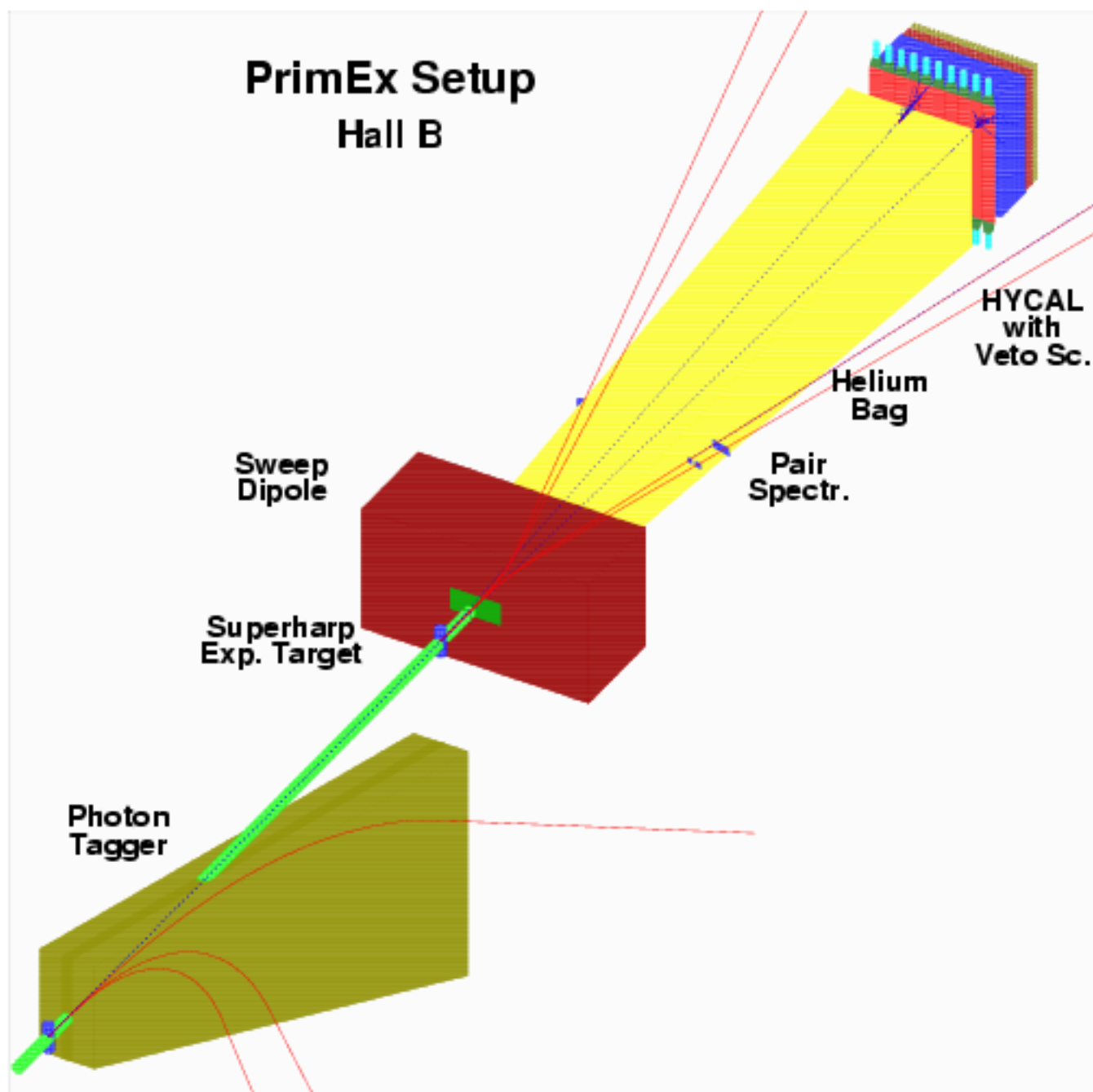


Figure 3: Layout of the experimental setup.

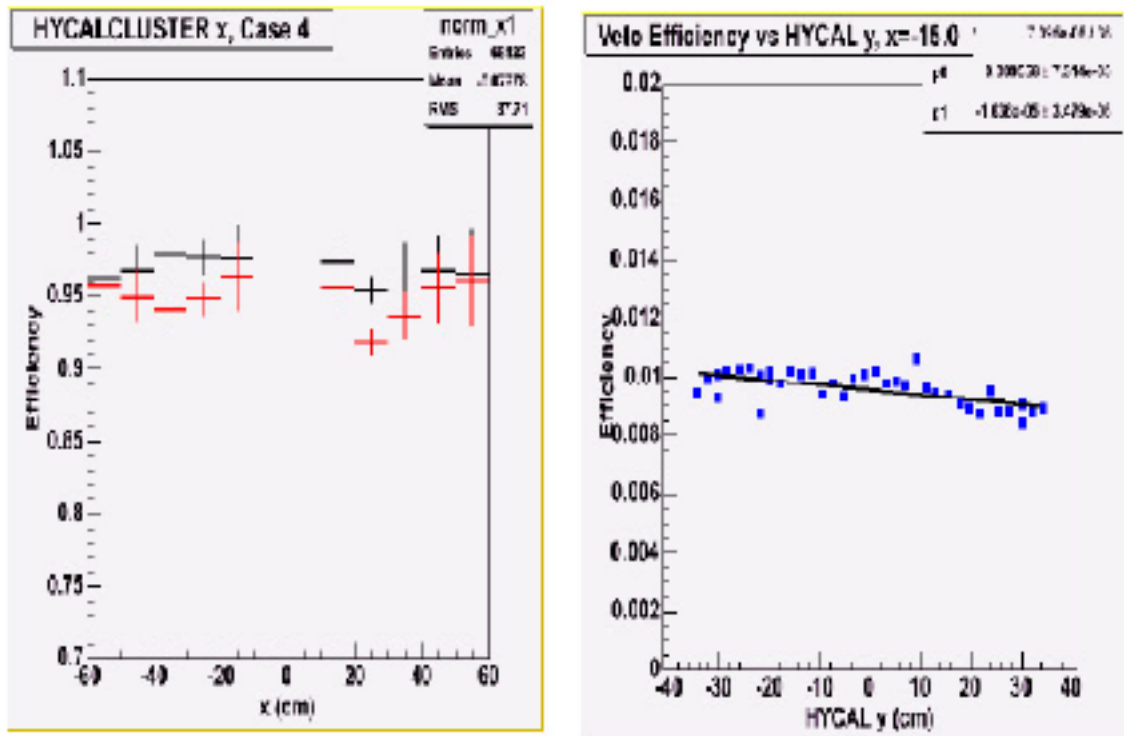


Figure 4: .

that the probability for photon conversion in the paddles is small. Light is collected from both ends of the paddles using XP2262B PMTs from Photonis and tube bases from Vorg Electronics. The time difference between flight times to the two PMTs is used find the longitudinal coordinate (y) of the hit. The counters were wrapped with an inner layer of Tyvek, and an outer layer of black Tedlar. During the first *PrimEx* run, the PMT gains were matched using special runs where e^+e^- pairs produced at the target were swept into the veto paddles by the pair spectrometer magnet, and we propose to take similar data during our next run. The time-walk effects due to varying signal sizes were observable, but were found to be small and had little effect on the y -position resolution. The veto y -positions, which were calculated from the time difference between the top and bottom PMTs, were calibrated against the hit positions given by HYCAL. The average resolution was determined to be $\pm 4.5\text{cm}$, which is within the tolerance of the experiment and corresponds to the width of the counters.

The pair production runs were also analyzed for the charged-particle efficiency. The efficiencies were determined by dividing the number of particles detected by a veto counter by the number of particles detected in the region of HYCAL covered by the acceptance of the given veto. Figure 4 shows that the charged-particle efficiency for the veto counters is approximately 95%. For the neutral misidentification analysis, data with low intensity photon beams incident on each veto counter were utilized. Figure 5 (left) shows the neutral misidentification probability for the counter at $x = -15\text{cm}$ versus the y -position given by

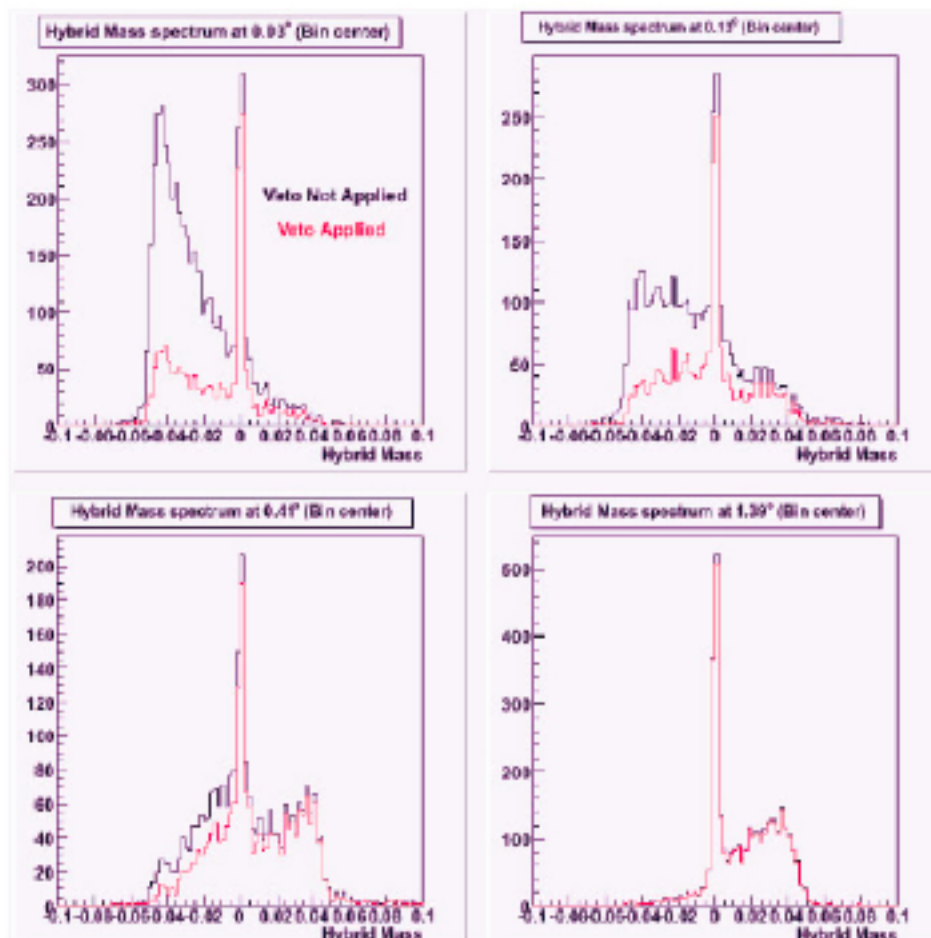
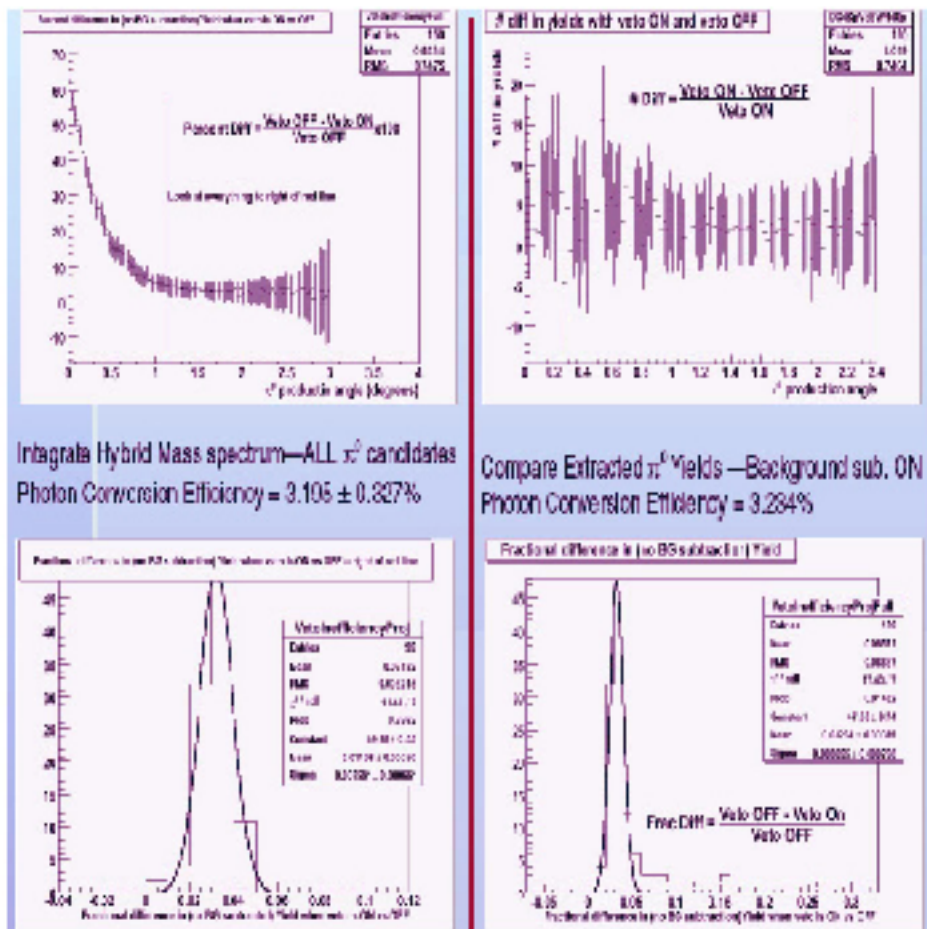


Figure 5: .

HYCAL. The plot shows that the conversion probability is low ($\sim 1\%$) and constant over the length of the counter. The other eleven counters show similar results.

Figure 5 (right) presents “hybrid” mass distributions taken during the 2004 run with the veto cut not applied, and then applied. The hybrid mass is closely related to the two-photon invariant mass distribution, and includes information on the elasticity of the event. In applying the veto cut, there was a requirement that the veto x - y coordinate should match the hit position in HYCAL, and also that there is a timing correlation between the veto counter and HYCAL. The plots are at π^0 angles which range from the Primakoff peak to the nuclear coherent region. The figure shows there is a very significant reduction in the background under the π^0 mass peak when the veto cut is applied at low angles.

In our π^0 analysis effort to date, we have used a global average derived from the π^0 analysis to account for photon conversion in the veto counters. We have investigated two methods to obtaining a global average from the data. The first involves integrating the hybrid mass distributions, examples of which are shown in figure 5, without and with the veto cut applied. The percent deviation with the veto cut applied is plotted as a function of angle in the top-left plot of figure 6. Note that figure ?? indicates the veto has a progressively



Integrate Hybrid Mass spectrum—ALL π^0 candidates
 Photon Conversion Efficiency = $3.105 \pm 0.827\%$

Compare Extracted π^0 yields—Background sub. ON
 Photon Conversion Efficiency = 3.284%

Figure 6: .

weaker effect on the hybrid mass distributions, and this is borne out in the top-left plot of figure ??, where the veto “effect” asymptotically approaches 3.20% at large angles. The second approach to fixing the average effect of photon conversion involves finding the number of events in the hybrid mass peaks without and with the veto cut applied. The percentage difference as a function of angle is plotted on the top-right plot of figure 6, and those data points are summed into a histogram on the bottom-right plot of figure 6. From this distribution, the average veto conversion effect on the π^0 analysis is estimated at 3.23%, which is in good agreement with method #1.

4.2.2 The hybrid electromagnetic calorimeter *HYCAL*

At the incident photon energies of this experiment ($E_\gamma = 4.6 - 5.7$ GeV), the Primakoff cross section peaks at extremely small angles ($\theta_{peak} \simeq 0.02^\circ$). Therefore, in order to identify and extract the Primakoff amplitude, the experimental setup must have sufficient angular resolution for detecting forward produced pions. The pions are identified by detecting the decay photons ($\pi^0 \rightarrow \gamma\gamma$) in the multi-channel electromagnetic calorimeter. Good invariant mass resolution in the $\gamma\gamma$ system also required for the selection of pions from the experimental background. These kinematical variables have strong dependence on both the position and energy measurement accuracies of the calorimeter. In addition, the kinematical constraints imposed by the knowledge of the initial photon energy provided by the tagging system results in a significant improvement of the angular resolution and invariant mass. The combination of photon tagging facility and a high resolution calorimetry is one of the important advantages of our experiment over the previous Primakoff type of experiments. It provides significantly improved invariant mass resolution, which is important for the clean identification of photoproduced pions and high resolution in production angle to extract the Primakoff amplitude from the competing background nuclear processes. A precision experiment also requires a large geometrical coverage for the decayed photons. At this energies, in order to detect 70% of the events the calorimeter must have over 1×1 m² cross-sectional size on a distance of 7 m from the production target. To optimize the cost and performance of the calorimeter we have made a decision to construct an hybrid type of calorimeter combining the traditional lead glass shower detectors and newly developed high resolution $PbWO_4$ crystal scintillators. The lead glass part of the calorimeter was made of TF-1 GAMS-type Cherenkov detectors ($3.82 \times 3.82 \times 45.0$ cm³ in size) and was provided by our collaborators from IHEP, Protvino Russia. Each lead glass was wrapped into aluminized Mylar and viewed with FEU-84 PMT’s. These detectors have been used in many other experiments and characteristics are well understood. They provide stable performance with a moderate resolutions in both position and energy [?]. For the high resolution crystal part of the calorimeter we have done an extensive R&D work to select the crystal type, the manufacturer as well as the detector structure. In the past few decades, $PbWO_4$ has become a popular inorganic scintillator material for precision and compact electromagnetic calorimetry in high and medium energy physics experiments. The performance characteristics of the $PbWO_4$ crystals before our tests had been well known mostly for high energies (>10 GeV)[28] and at energies below one GeV[29]. In order to check the performance of the crystals at the few GeV region and to select the manufacturer, we have carried out beam tests with a 6×6 prototype detector consisting of crystals from two different manufacturers: Bogoroditsk (BTCP), Russia

and Shanghai (SIC), China. The upper 3×6 section of the detector was assembled from crystals made in Russia, and the bottom section consists of Chinese crystals from SIC. The scintillation light from the electromagnetic shower was detected with Hamamatsu R4125HA photomultiplier tubes coupled to the back of the crystals with optical grease. The prototype detector was moved by remote control in two dimensions perpendicular to the secondary electrons, which were selected by the PrimEx/Hall B dipole magnet and the scintillating telescopes. A x and y coordinate scintillation fiber detector (2 mm in fiber size) was used on the front of the detector to define the impact points of the electrons. The performance of the crystal prototype was studied with secondary electrons with energy from $E_e = 2$ to 4 GeV. Results on energy and position resolution, and the dependence of crystal detector response on radiation rate were presented at the Calor-2002 International Conference[31]. We have procured 1250 from SIC based on the high performance they exhibited in these tests as well as the comparatively lower price per crystals, which was achieved through our collaborators in China (Chinese Institute of Atomic Energy, CIAE). This has enabled us to increase the number of crystals in the calorimeter by more than a factor of two over that envisioned in the original proposal and funded by the NSF MRI award. The increased size of the crystal detectors significantly enhanced the high resolution part of the calorimeter and played a critical role for the π^0 decay width extraction in the current experiment. Each crystal arrived at JLab from the manufacturer was first tested for the mechanical properties (visual inspection and dimensions at four points). A typical distribution of measured size at front side of the crystals from one shipment is shown in Figure 7. For those crystals passed the mechanical specifications the optical transmission *versus* the wavelength was measured using the JLab Detector Group's photospectrometer. A typical transmission spectra are shown in Figure 8 and Figure 9

Two important criteria had been set for the development of lead tungstate detector module development: to optimize the light collection from the back side of the crystal and to minimize the mechanical structure in tangential dimensions. A complete module of the $PbWO_4$ crystal detector is shown in Figure 10. The scintillation light from the electromagnetic shower in the crystals was detected with Hamamatsu R4125HA photomultiplier tubes (PMT) coupled at the back with optical grease. Each crystal was first wrapped in $\sim 63 \mu\text{m}$ VM-2000 reflector (from 3M company), then with a $38.1 \mu\text{m}$ black Tedlar for optical isolation between the blocks. The PMT housings were attached to the crystals with two specially designed brass flanges on the front and back of the crystals, stretched with two $25 \mu\text{m}$ brass strips.

One of the challenging problems of the hybrid type calorimeters is the potential deterioration of the energy and position resolutions at the boundary region between the two type of radiators (for HYCAL, $PbWO_4$ crystals and lead-glass detectors). The difference in electromagnetic shower development both in longitudinal and lateral directions in $PbWO_4$ and lead glass also requires optimization of the position of the crystal radiators along the lead glass blocks. The first experimental results for the calorimeter characteristics *versus* the crystal z -position for 10-70 GeV electrons have been presented in [32]. Since the longitudinal development of shower is energy dependent, the optimization of the z -position is energy dependent also. We have performed extensive Monte Carlo simulations to define the optimum z -position of the $PbWO_4$ radiators along the lead glass blocks for the HYCAL calorimeter. These simulations, which are cross-checked with the experimental data

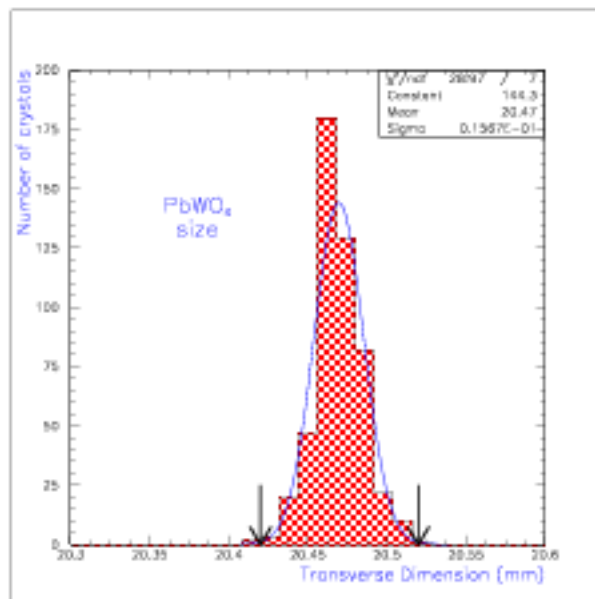


Figure 7: Distribution of front size of crystals from one shipment. Tolerance in size are shown by arrows.

from Ref. [[32]], showed that for the few GeV energy region the optimum for the τ -position is within the 7-10 cm interval. In order to investigate the performance of the calorimeter at the transition region between the $PbWO_4$ crystals and lead glass detectors, and, also to check the calorimeter's engineering concepts in real conditions, a prototype hybrid calorimeter (HYCAL-0) was constructed and tested in 2002 using the intense tagged photon beam. It consisted of 96 lead glass and 77 lead tungstate shower detectors and was assembled in a light-tight iron frame maintained at a stable temperature of $T = 11^\circ C$. After the two stages of prototyping and successive beam tests, the PrimEx collaboration constructed and assembled 1152 $PbWO_4$ crystal shower detectors (shown in Figure 10) and 576 lead glass Cherenkov counters as described above ($116 \times 116 \text{ cm}^2$ area). All individual detector modules have been stacked in a specially designed light-tight iron frame, as shown in Figure 11. The light yield of the crystal is highly temperature dependent ($\sim 2\%/^\circ C$). In order to keep the detector array at a stable temperature, the detector assembly was surrounded by thick copper plates with circulating coolants. Temperature stability at the level of $\Delta T = \pm 0.1^\circ C$ was achieved during the entire period of data collection. To optimize the shower leakage in the transition region the lead tungstate detector assembly, which is in the central part of the calorimeter, is shifted downstream of the lead glass modules by 10 cm. Four crystal detectors are removed from the central part of the calorimeter ($4.1 \times 4.1 \text{ cm}^2$ hole in size) for the passage of the incident photon beam through the calorimeter.

The calorimeter is furnished with rear end readout electronics, with signal cables (two from each channel, for anode and dynode signals), high voltage cables and fiber optics cables

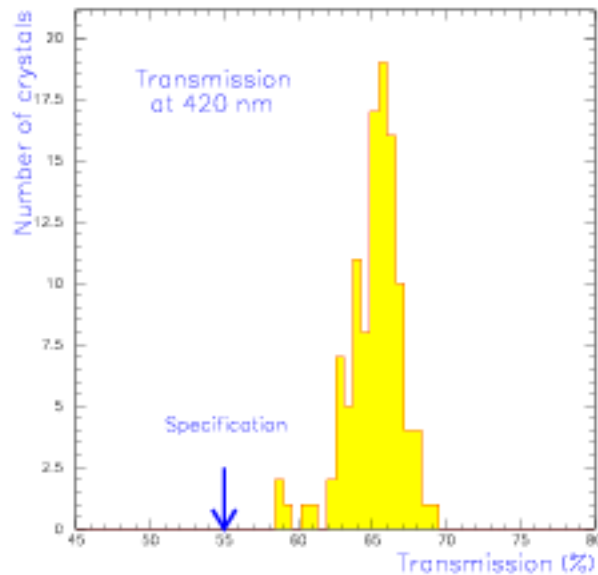


Figure 8: Optical transmission of crystals at 420 nm.

from the front part of the calorimeter for gain monitoring system. The anode signals after 300 ns delay were digitized by means of a 14-bit charge-sensitive ADC (LeCroy 1881M, integration width=240 ns). The positive dynode signals were summed group by group to form a total sum from the entire calorimeter for the trigger organization as it described in the next sections.

4.3 The Calorimeter Frame and Transporter

The individual modules of the HYCAL are assembled in a rectangular box inside of the calorimeter frame. The entire assembly weighs over five tons, and is movable in both horizontal and vertical directions in order to place each module in the beam for energy calibration. The transporter, shown in figure 4.2.2, has been designed and constructed to provide movement of the entire assembly of the support frame with detectors and thermostabilization system, the delay cables, the gain monitoring system mounted on the bottom of the HYCAL frame and the veto counters on the front of the HYCAL.

The calorimeter is remotely movable so that during the calibration and checkout of each module it can be positioned in the beam of tagged photons with an accuracy of $\pm 2mm$. A schematic drawing for this system is shown in figure 13. After the calibration and channel by channel checkout procedure the calorimeter was moved to a specially designed support stand for the experiment. A drawing of the calorimeter in the data taking position is shown in figure 14. In this configuration, the accuracy of centering the detector transverse to the

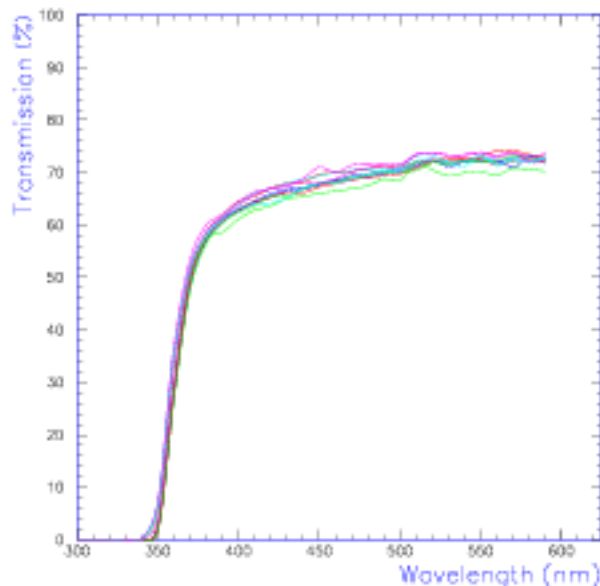


Figure 9: Typical optical transmission of crystals versus wavelength.

beam is $\pm 0.7\text{mm}$. In addition, this system also provides the capability to move the detector along the beamline for the different Z-position from the physical target.

When the calorimeter is not being used in the beam or in experiment, the transporter system provides positioning of the entire calorimeter a few meters above the beam center, on the level 2 of the Hall B beamline. In addition to storage, this configuration allows the HYCAL to be available for re-assembly, maintenance, and testing with cosmic rays.

4.4 Performance of the Calorimeter

As it mentioned above, the calibration of the HYCAL was performed with low intensity tagged photon beam of selected energies ($E_\gamma = 0.5 - 5.5\text{ GeV}$) irradiating the centers of each detector module while the calorimeter was on the transporter configuration. Then, a tagged photon beam was scanned across the boundary with 2 mm step size to get a data for the position and energy resolutions for the both type of detectors as well as for the transition region between them.

The reconstructed energy distribution for the 4.3 GeV electrons is shown in figure 15 for three different calibrated ADC sums: the central module; the inner section comprising 3×3 crystals and the array of 6×6 crystals. The energy resolution is obtained using a Gaussian fit of the 6×6 distribution. As can be seen from the figure, an excellent energy resolution of $\sigma_E/E = 1.3\%$ has been achieved for 4.3 GeV.

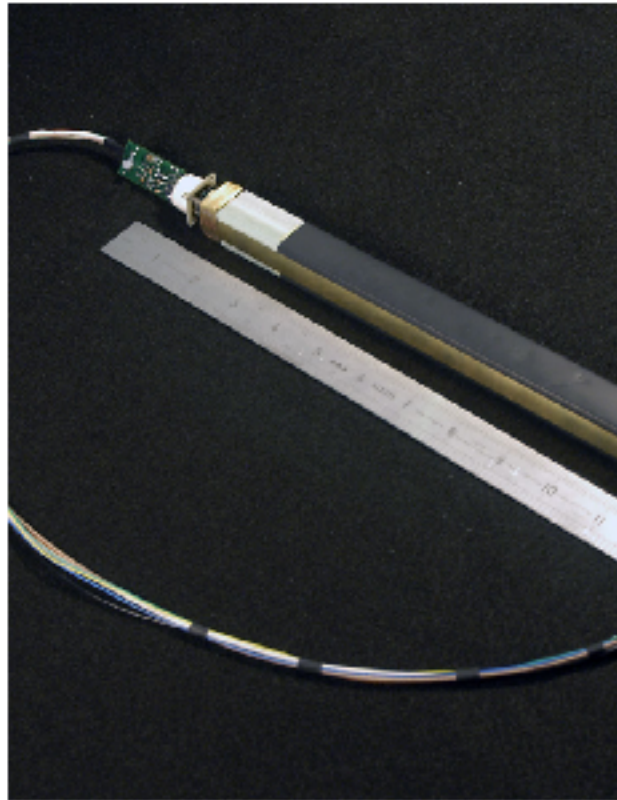


Figure 10: A single $PbWO_4$ crystal shower detector module.

The measured energy resolution versus initial photon energy is shown in figure 16. The resolution of the lead glass part of detector is shown in figure 17

Using the data from the transition region the energy resolution of the shower cluster was extracted as a function of position. Dependence of the energy resolution versus photon impact position is shown in Figure 18. Degradation in resolution as the photon beam passes from the last lead tungstate module to the lead glass region is evident and well described by the Monte Carlo simulation. Figure 18 (bottom) shows the relative reconstructed total energy for the same transition region. The $\sim 3\%$ dip at the interface predominantly arises from shower leakage from the uncovered backs and sides of the lead glass blocks.

The impact coordinates of the electromagnetic particles incident on the segmented hodoscopic calorimeters are being determined from the energy deposition of the electromagnetic shower in several neighboring counters. In the case of the $PbWO_4$ crystals, the transverse size of the shower is about two times smaller than that in lead glass. As a result, the position resolution in the $PbWO_4$ detector with an optimal cell size should be about twice smaller than that of lead glass detectors. To maximize the position resolution, we have optimized the crystals' transverse dimensions, and have selected it to be $2.05 \times 2.05 \text{ cm}^2$. This size is comparable to the Molière radius (2.2 cm) of the crystal material.

The distribution of the reconstructed coordinates for 4.3 GeV electrons hitting a crystal cell boundary is shown in Figure 19. The linear dependence of the reconstructed coordinates obtained from a logarithmically weighted average of the cell signals versus the impact positions is shown in Figure 20. As is well known, there is a rather strong correlation between

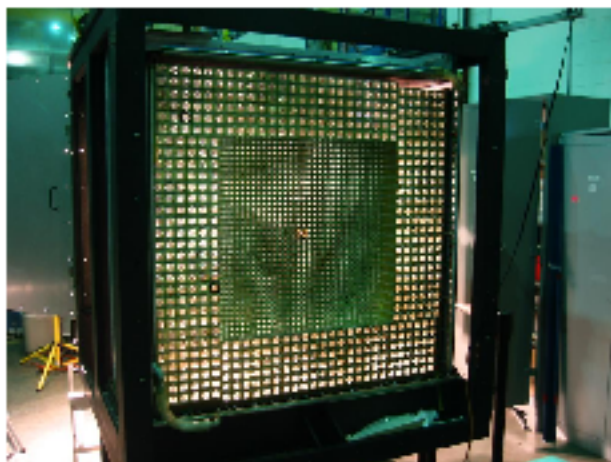


Figure 11: Front view of the HYCAL Calorimeter with all modules in place and before installation of fiber optics cables on front of each channel for the gain monitoring system.

the position resolution (σ_x) and the point at which the incoming electrons or photons hit the detector face. The bottom plot of the figure shows this dependence for the $PbWO_4$ crystals. The σ_x is smaller (1.28 mm) near the edge of the cell and increases to 2.1 mm at the cell center.

Similar to the energy reconstruction one can expect degradation in the position resolution in the transition region as the photon beam passes from the last lead tungstate crystal module to the lead glass region. This dependence is shown in Figure 21. Though the simple center-of-gravity reconstruction exhibits typical oscillation of reconstructed *versus* impact position with a relatively larger amplitude, the corrected logarithmic method shows a good linear transition from lead tungstate to lead glass regions.

Good position and energy resolutions achieved for the HYCAL calorimeter provided critical improvements in both two gamma invariant mass and production angle reconstructions. As an example in Figure 22 is shown the two gamma invariant mass distribution extracted from the experimental data set for one angular bin only. An excellent resolution of $\sigma_{\gamma\gamma} = 2.3$ MeV provided precision extraction of events over the experimental background.

4.5 HYCAL Gain Monitoring System

To control the stability of gains for each channel of the calorimeter during the long data taking periods a gain monitoring system was developed and constructed. This system is based on feeding light pulses from a central LED based light source distributed by fiber optics cables to the front part of each module. The main components of the Light Monitoring System (LMS) are: (1) a light source, (2) a mixing box, (3) a light distribution system, (4) filter wheel, (5) reference detectors and (5) a dedicated data acquisition system. The optical components and the reference detectors, as it shown in Figure 23, are mounted in a thermally insulated box whose temperature is controlled at a level of 0.1°C .

A long term stability tests of the prototype LMS system as well as several beam test have been performed to finalize the design and characteristics of the system. For this tests,



Figure 12: The HYCAL transporter in Hall B.

the light intensity was monitored with a PIN photodiode and three reference PMTs. In figure 24, top picture, the distribution of the ratio, PMT_1/PMT_3 , for the period of time of 540 hours is shown. The same ratio plotted versus time, is presented in the bottom picture.

During the data taking period it was observed that the LMS reference detectors are somehow still partially sensitive to the change of magnetic field from the pair spectrometer dipole. This change of signals was observed on the level of 1.5reference PMT signals [31]. We plan to fix this problem by adding more magnetic insulation and/or try to replace the PMTs on the reference detectors with less sensitive photodetectors.

4.6 Luminosity monitoring

The primary advantages of the *PrimEx* experiment over the previous Primakoff experiments arise from the use of the Jefferson Lab Hall-B photon tagging facility to carefully control systematic errors and reduce backgrounds. First, the tagging technique allows for a significantly more accurate knowledge of the photon flux. Second, due to the energy dependence of the Primakoff cross section, it is critical to have a good knowledge of the absolute photon beam energy.

In order to determine the energy of the decaying π^0 , each event is recorded in coincidence with a signal from the tagger. The experimental cross section for neutral pion photo-production is given by:

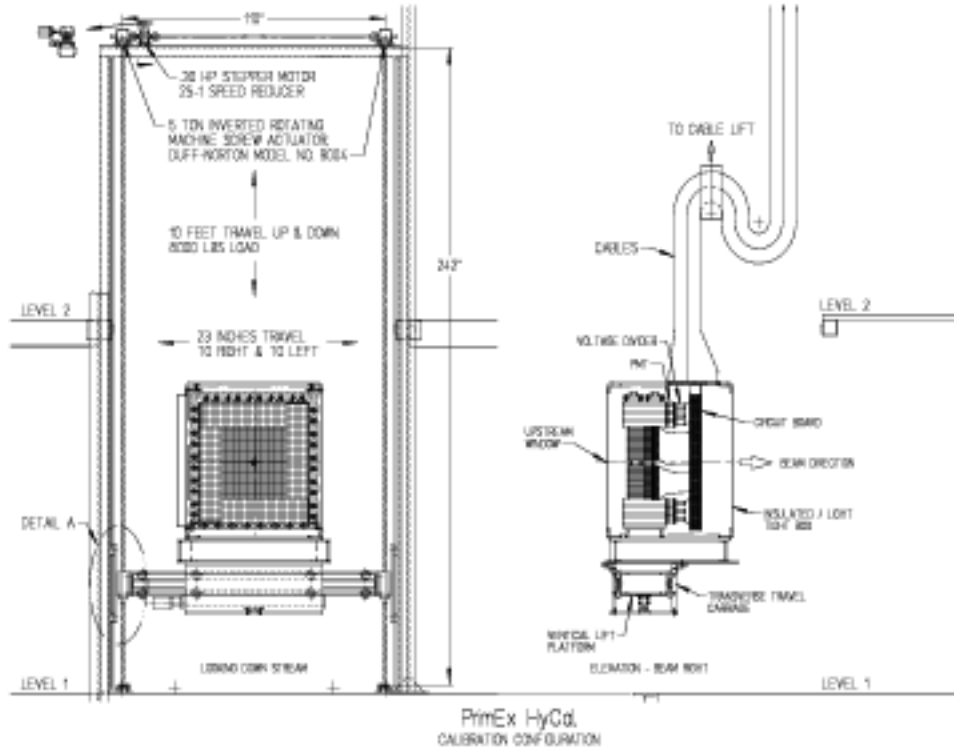


Figure 13: The HYCAL mounted on its transporter.

$$\frac{d\sigma}{d\Omega} = \frac{dY_{\pi^0}^{\text{tagged}}}{N_{\gamma}^{\text{tagged}} \cdot \epsilon \cdot t \cdot d\Omega} \quad (8)$$

where $d\Omega$ is the element of solid angle of the pion detector, $dY_{\pi^0}^{\text{tagged}}$ is the yield of tagged π^0 -s within solid angle $d\Omega$, t is the target thickness, ϵ is a factor accounting for geometrical acceptance and energy dependent detection efficiency and $N_{\gamma}^{\text{tagged}}$ is the number of tagged photons on the target.

The number of tagged photons per post bremsstrahlung electron can be measured in a calibration run by removing the physics target and placing a lead-glass total absorption counter (TAC) directly in the photon beam. Assuming that the total absorption counter is 100% efficient in detecting photons in the energy range relevant for the experiment, TAC the ratio of Tagger-TAC coincidences to the number of tagger hits, the so called absolute tagging ratio, is then recorded:

$$R_{\text{absolute}} = \frac{N_{\gamma}^{\text{TAC}}}{N_e} \Big|_{\text{calibration}} \quad (9)$$

where N_{γ}^{TAC} is the number of photons registered by the TAC in coincidence with a tagging signal and N_e is the number of electrons registered in tagging counters.

Knowing this ratio, one can determine the tagged photon flux in the data taking run by counting the number of post bremsstrahlung electrons in the tagging counters:

$$N_{\gamma}^{\text{tagged}} \Big|_{\text{experiment}} = N_e \Big|_{\text{experiment}} \times R_{\text{absolute}} \quad (10)$$

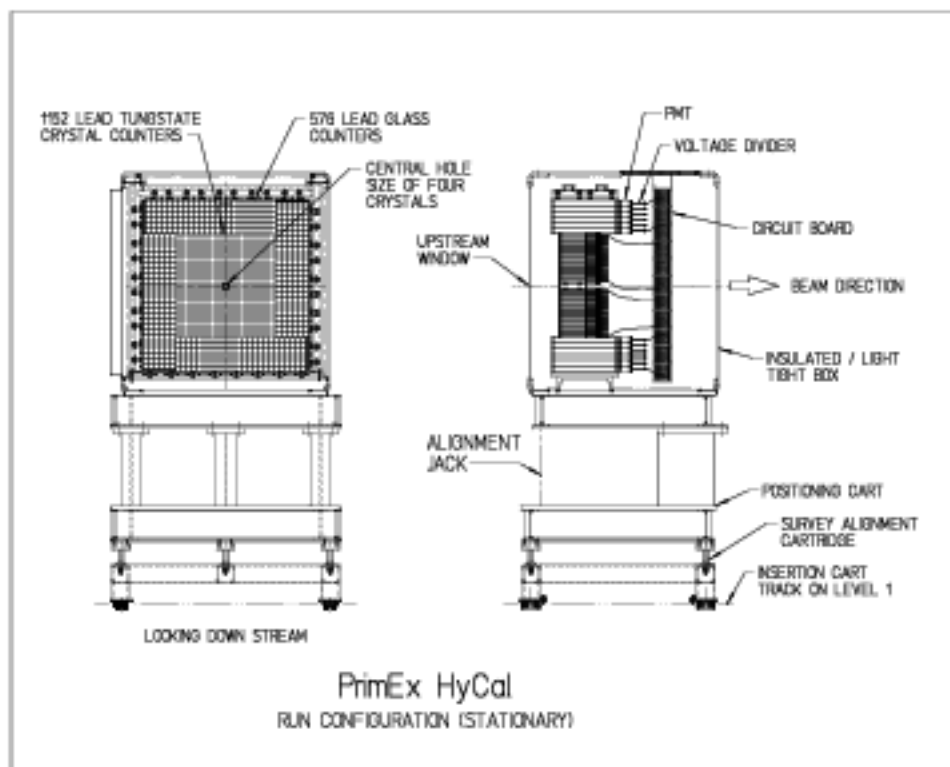


Figure 14: The HYCAL detector on its support stand in the run configuration.

The use of the total absorption counter to calibrate the number of tagged photons per electron in the tagger provides an absolute normalization of the photon flux incident on the π^0 production target. However, these measurements can be performed only at intervals between the data taking. Also in the calibration run, the rate of the total absorption counter is limited, and therefore, the tagging ratio can only be measured at a rate which is reduced by a factor of about one thousand as compared to the data taking run. A pair production luminosity monitor was constructed (see Section ??) which is able to measure the relative tagged photon flux over a range of all relevant intensities, and operate continuously throughout the data taking runs. The PS uses the physics target as a converter to measure the ratio of the number of $\gamma + A \rightarrow A + e^+ + e^-$ reactions in coincidence with a tagging signal to the number of hits in the tagging counters (see Equation 11),

$$R_{\text{relative}} = \frac{N_{e^+e^-}^{PS}}{N_e} \quad (11)$$

while this is a relative number, its absolute normalization can be fixed with the TAC. The advantages of the pair spectrometer are that it can operate over the entire range of intensities (of both the flux calibration and data taking runs) and has a smooth, relatively flat acceptance in E_γ covering the entire tagging range.

The main contribution to the error bar in the PrimEx measurement comes from the knowledge of the photon flux. To achieve the desired precision in the measurement of the π^0 decay width it is necessary to know the photon flux to 1% or better. It should be noted that

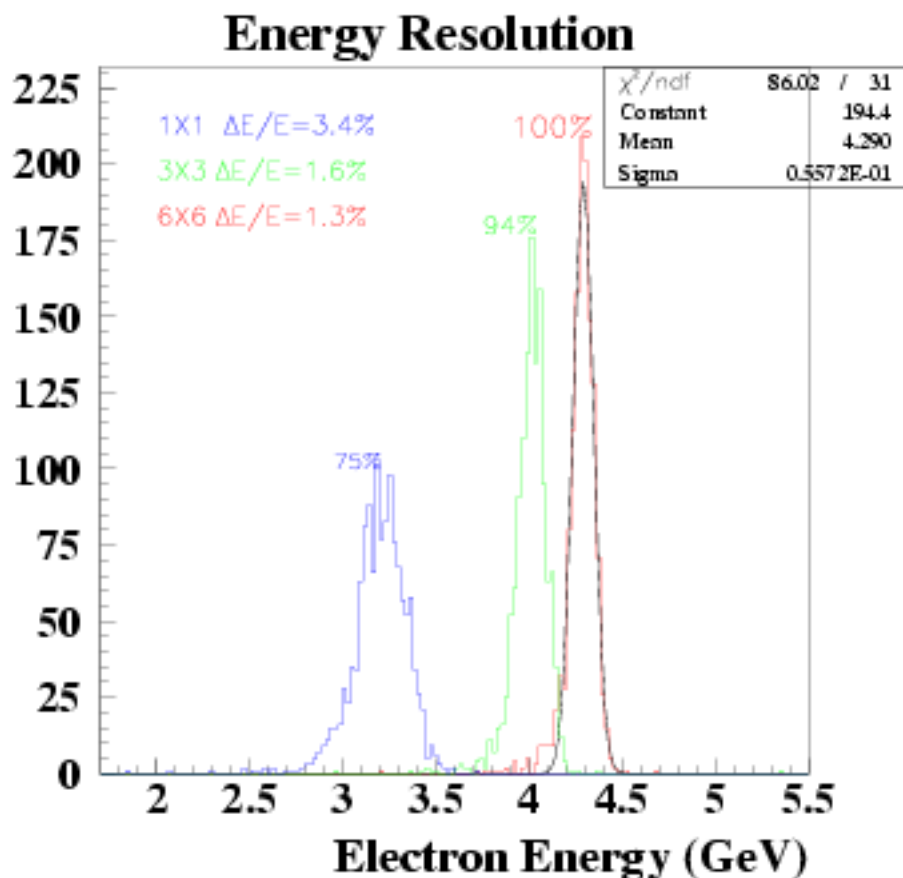


Figure 15: Energy response of a $PbWO_4$ crystal array to 4.3 GeV electrons. Left peak: single crystal; center peak: 3×3 array; right peak: 6×6 array.

such a high precision measurement of the photon flux has not been previously attempted at Jefferson Lab Hall-B. As indicated by equation 10 the problem of cross section normalization is reduced to the determination of the number of electrons in tagging counters and measuring the absolute tagging ratio. The constant online monitoring of the relative photon flux is also crucial for the precision tagged photon flux measurement.

4.6.1 Absolute tagging ratios

During *PrimEx* data taking in the Fall of 2004, specialized calibration runs were periodically performed to determine the absolute normalization of the photon flux. For a calibration run, the experimental target is retracted and a Total Absorption Counter (TAC) is placed in the path of the photon beam. To avoid the radiation damage to the TAC, the electron beam intensity is lowered to $\sim 70 - 80 pA$. The low intensity of calibration runs enables the use of the Tagger Master OR (MOR) signal as the data acquisition trigger. The MOR signal is formed by OR-ing the timing information from all or any of the 61 T-counters. Using

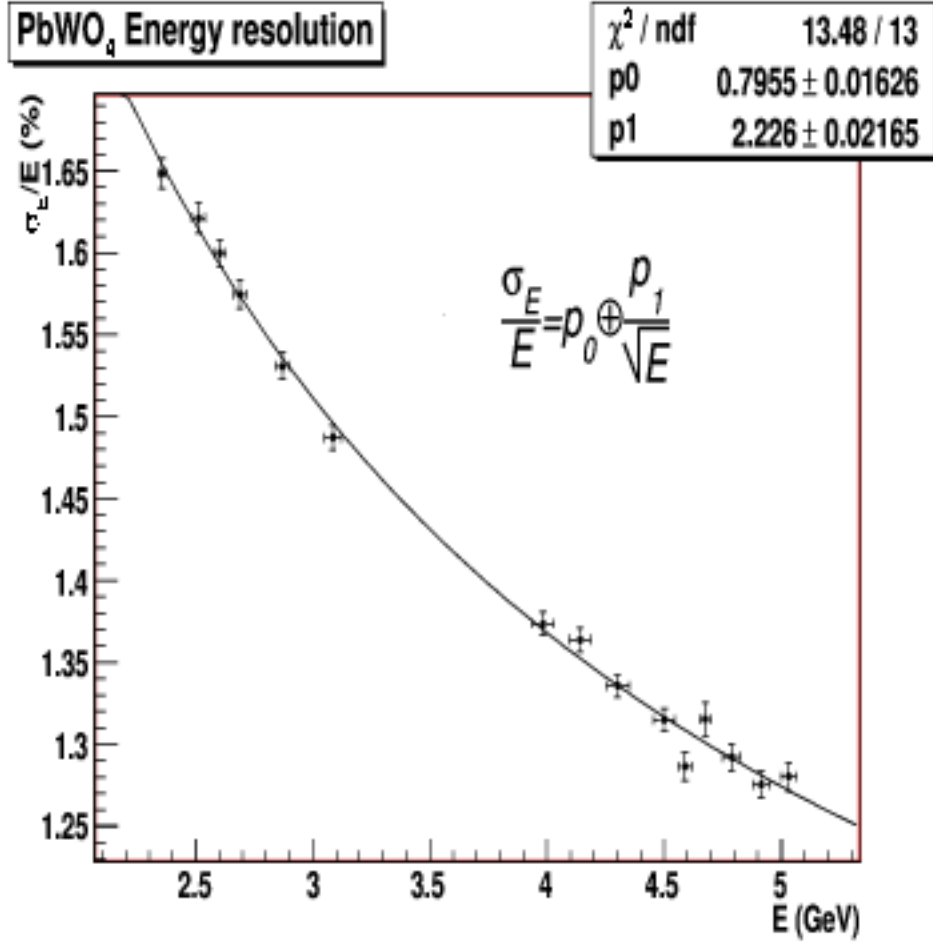


Figure 16: Measured energy resolution versus photon beam energy for the $PbWO_4$ part of the calorimeter.

the MOR trigger enables one to directly count the number of electrons that hit the tagging counters.

Absolute tagging ratios are defined for each of the T-counters as:

$$R_{absolute}^i = \frac{N_{\gamma e^+}^{TAC}}{N_e^i} \quad (12)$$

where N_e^i is the number of electrons registered in the T-counter i and $N_{\gamma e^+}^{TAC}$ is the number of photons registered by the TAC in coincidence with an electron in the T-counter i .

A number of possible systematic errors associated with the determination of the absolute tagging ratios were studied in our 2004 run. These included:

- Effects of incident electron beam intensity on absolute tagging ratios
- Effects of photon collimator size
- Effects of collimator position misalignment

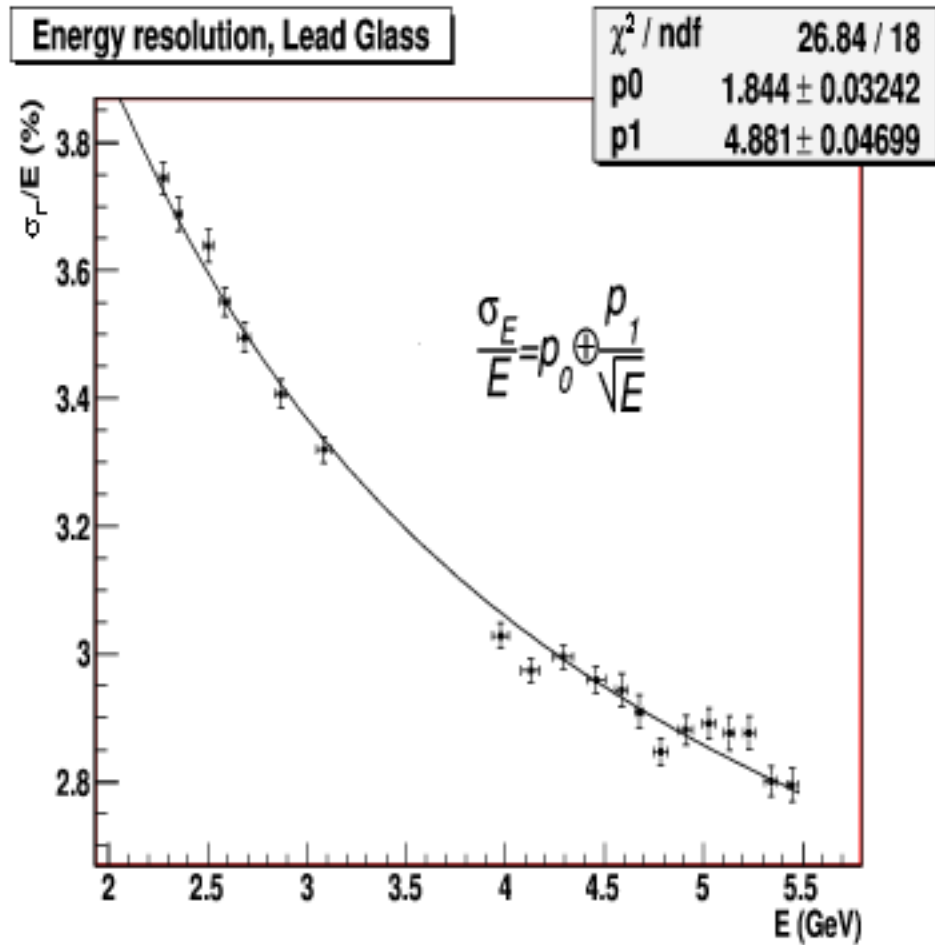


Figure 17: Measured energy resolution versus photon beam energy for the $PbWO_4$ part of the calorimeter.

- Effects of HYCAL scraping due to beam mis-steering
- Long and short term reproducibility of tagging ratios
- Effects of the pair spectrometer dipole field on the tagging ratios
- Absorption in the target

While the details of these studies are given in the appendix, the overall systematic uncertainty in the flux determination was found to be 1%.

4.6.2 Relative tagging ratios measured with pair production

The Pair Spectrometer is an essential part of PrimEx experimental apparatus designed for relative in-situ monitoring of the photon flux. It uses the experimental target to convert a fraction of photons into e^+e^- pairs which are deflected in the field of a dipole magnet downstream of the target and are registered in plastic scintillator detectors on both sides of the beam-line. The relative tagging ratios per T-counter are defined as:

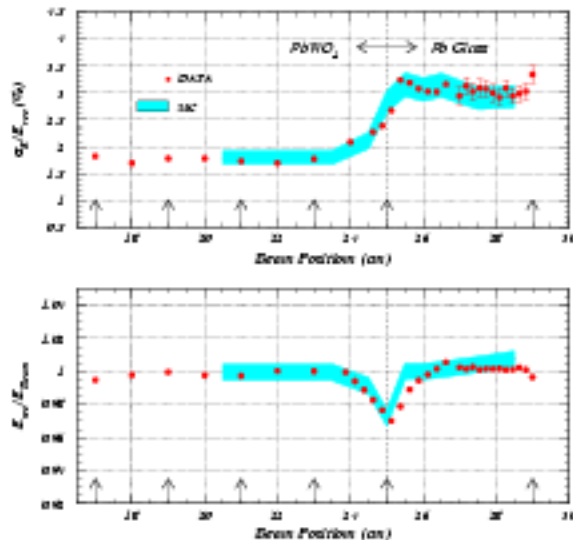


Figure 18: Beam test results for the transition region between $PbWO_4$ and lead glass modules. Top: energy resolution. Bottom: relative reconstructed energy versus position. The gray bands indicate Monte Carlo simulations.

$$R_{\text{relative}}^i = \frac{N_{e^+e^-}^{PS}}{N_e^i} \quad (13)$$

where N_{e_i} is the number of electrons registered in T-counter i and $N_{e^+e^-}^{PS}$ is the number of e^+e^- pairs registered by PS in coincidence with an electron in T-counter i .

During our production data taking, in Fall of 2004, we had random, *i.e.* not related to the particles in the beam, clock trigger set up to measure R_{relative}^i . The use of the random trigger allows to directly count the number of electrons in the tagging counters and it gives the advantage of being insensitive to beam intensity variations.

4.7 Photon beam position monitor

A photon beam position detector was constructed by the collaboration that had provided continuous real time photon beam position and profile information during the first experiment, as well as information in the data stream for off-line data analysis. This detector consists of two identical modules crossed at right angles to each Other (shown in 25 to give the beam profile along both x and y directions). Each module is a linear hodoscope of multi-channel Bicron scintillating fibers (X module has 61 channels and Y module has 62) forming a plane perpendicular to the photon beam. This detector is mounted on a remote controlled table with the X and Y motion placed just the HYCAL at nominal beam path. Each scintillating fiber has dimension of $2 \times 2 \times 13 \text{ mm}^3$. The scintillating light from the fibers transmit through the light guide and is detected by four 16-channel R5600-M16 Hamamatsu PMTs. A compact electronics module provides 64 channels of amplifier and discriminators for anode

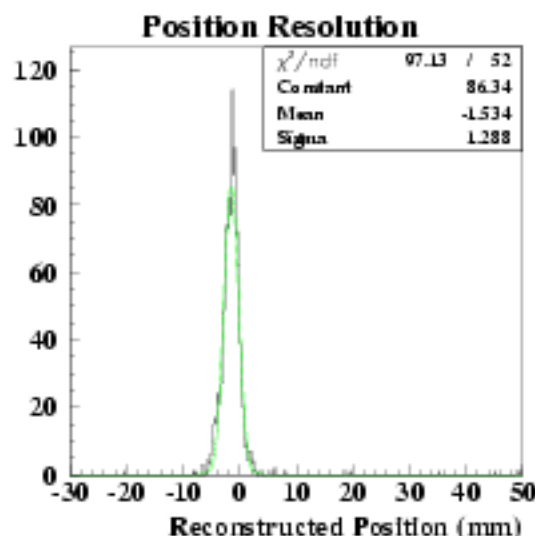


Figure 19: Distribution of reconstructed positions at the boundary between two lead tungstate crystal detectors.

signals, then convert them to ECL readout through a time-over-threshold circuit. The ECL signals are sent over to SIS3801-256-flat scalars and read into epics systems. During the run, the x and y beam profiles were displayed through a GUI for on-line beam control (shown in figure ??) and read into DAQ for off-line analysis. This device performed beautifully during the experiment and provided an excellent beam diagnosis tool.

4.8 Data acquisition and trigger

The *PrimEx* data acquisition system must read out over 2200 channels of ADC and TDC information coming from five different detector systems. These include the HYCAL calorimeter, the HYCAL veto, the pair spectrometer, the total absorption counter, and the Hall B photon tagger. The digitization electronics will span at least three Fastbus crates which must be coordinated for proper event reconstruction.

The *PrimEx* data acquisition system is a CODA based Fastbus system utilizing the JLab designed Trigger Supervisor module. In addition to the three Fastbus crates, this system includes one CAMAC crate, one VME crate, and one hybrid VME/VXI crate. Electronics occupying six NIM crates are also needed for the first stages of the trigger. A big advantage of the CODA/Trigger Supervisor system is the ability to run in fully buffered mode. In this mode, events are buffered in the digitization modules themselves allowing the modules to be live while being readout. This significantly decreases the deadtime of the experiment. All of the electronics needed for the *PrimEx* DAQ and trigger electronics has been procured and is onsite at JLab.

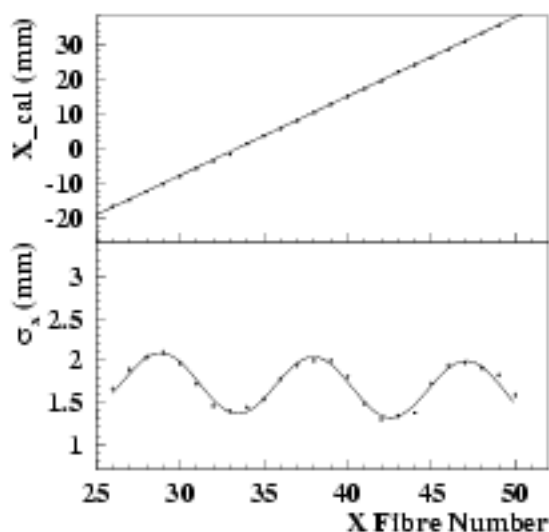


Figure 20: Reconstructed versus actual position (top) and position resolution (bottom) across the face of $PbWO_4$ crystal array.

4.8.1 Trigger

The *PrimEx* trigger is formed from the last stage dynode signals from HYCAL. The anode signals are sent directly to the Fastbus ADC modules via long RG58 cables. The trigger initially constructed for the 2004 PRIMEX run would have looked for multiple clusters in HYCAL separated by at least 15 cm. This was done by fanning in strips of like detectors ($PbWO_4$ and Pb-glass are done separately) which span the calorimeter in both the horizontal and vertical directions. In the $PbWO_4$ region of the calorimeter the strips are either 7 or 8 detector units wide, and in the Pb-glass the strips are either 3 or 4 detector units wide. There are 7 such strips in the horizontal direction, and 7 strips in the vertical direction. Using strips in this fashion ensures at least 50 energy deposited in one cluster will be seen by a discriminator. Each strip was discriminated at a level of on half of the minimum energy π^0 decay photon we wish to detect. This level was set to 0.5 GeV since we wish to accept all events with photon energies 1 GeV or higher. The 7 strips of each direction are taken to form a 14-bit word which was then used to access an address of a Memory Mapping Unit (CAEN C542). Patterns in which (i) two non-adjacent strips fire in one direction or (ii) two adjacent strips fire in both directions would have created a trigger.

However, the commissioning period preceding the 2004 run, it was discovered that reasonable trigger rates are obtained using a trigger based on the total energy sum in HYCAL. For this reason, it was decided to take data with the more conservative and conceptually much simpler total energy sum trigger. By using the energy sums already established for the trigger strips, only one additional level of signal fan-in was required to form the total energy sum. The energy sum trigger threshold was set at approximately 2 GeV for the 2004 run, and the trigger rate for the ^{12}C running was a modest, by Hall B standards, 1.2 kHz. We propose to use the same total energy sum trigger for the next *PrimEx* run.

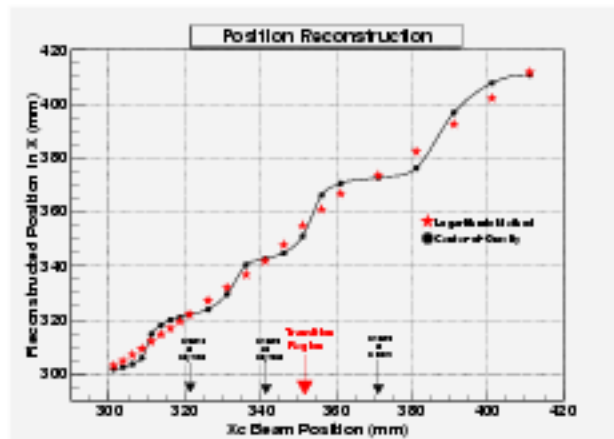


Figure 21: Reconstructed *versus* impact coordinate at the transition region of the HYCAL calorimeter.

The UVA120 and 125 linear fan-in and discriminator modules were chosen for the *PrimEx* trigger electronics because of the large number of channels (36 for the UVA120 module) and the economic advantage over commercial modules. The specific needs of the PRIMEX trigger required some special modifications to both the UVA120 and its sister module, the UVA125. One significant modification in the UVA120 design was to make both outputs inverting. This allows the module itself to be used as both a splitter and inverter for the dynode signals, eliminating the need for additional hardware. The UVA125 is used for the last stage of fan-in and discrimination, and has 4 separate sections; each section has a 9-input linear fan-in and two built-in discriminators. The timing of the discriminators is determined by the discriminator with the lower threshold, making the timing properties better than single leading edge discriminators. The UVA125 modules can have the discriminator thresholds set via externally supplied voltages. These voltages will be supplied via a CAMAC DAC module (digital-to-analog converter) so that the thresholds may be adjusted remotely without making an access to the experimental hall.

The only user controlled part of the trigger is the DAC, which is housed in a CAMAC crate in Hall B. The DAC is used to set the threshold for the energy sum trigger. The CAMAC crate is controlled remotely over the internet, through a Kinetic Systems GPIB CAMAC controller and National Instruments GPIB E-Net device.

5 Preliminary Results from the 2004 Run

5.1 π^0 Photoproduction Cross Section Extraction

The *PrimEx* Collaboration has implemented three parallel data analysis procedures to extract the neutral pion lifetime. The primary considerations in event selection involve (1)HYCAL - Tagger timing information, (2) the invariant mass of the photons detected in the HYCAL, and (3), the elasticity of the candidate π^0 events, where elasticity is defined as $\frac{E_{\gamma 1} + E_{\gamma 2}}{E_{\text{tagger}}}$.

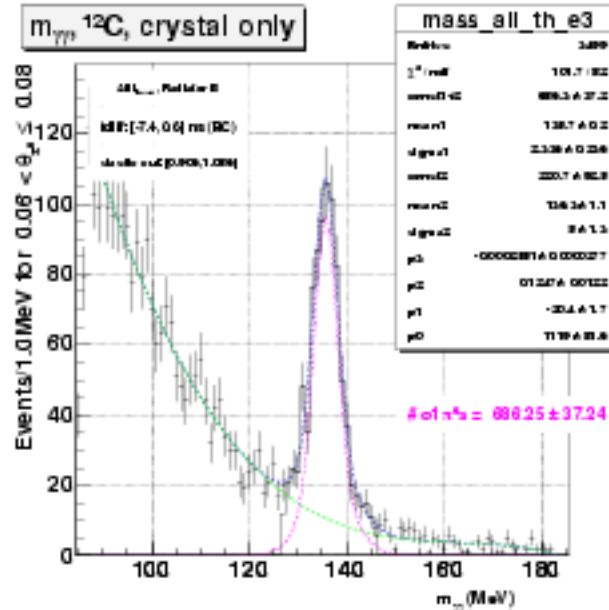


Figure 22: Distribution of two gamma invariant mass from the experimental data set for one production angle bin.

The first analysis involves an event selection procedure which utilizes normalized probability distributions for each of the above mentioned quantities. In this analysis, the total probability of a valid event is given by the product of each of these probabilities as follows:

$$TotalProbability = Timing \times InvariantMass \times Elasticity \quad (14)$$

An example of such a likelihood spectrum is shown in figure 27. For pion candidate events which are in coincidence with multiple photons on the tagger, this enables the selection of the best photon. Extensive studies of the inefficiencies of this selection procedure have been performed and found to have negligible effect on the resulting yield.

With this event selection procedure, the correlation between elasticity and reconstructed invariant mass is examined, and a new quantity, termed the “hybrid mass” is defined for each event. As indicated in figure 28, the hybrid mass is quantity which contains combined information on the elasticity and invariant mass.

A plot of the hybrid mass versus pion angle is shown in figure 29. A cut on the hybrid mass provides a clean separation of the pion events and the resulting angular distribution is shown in figure 30.

Dustin’s analysis

Ilia’s analysis.

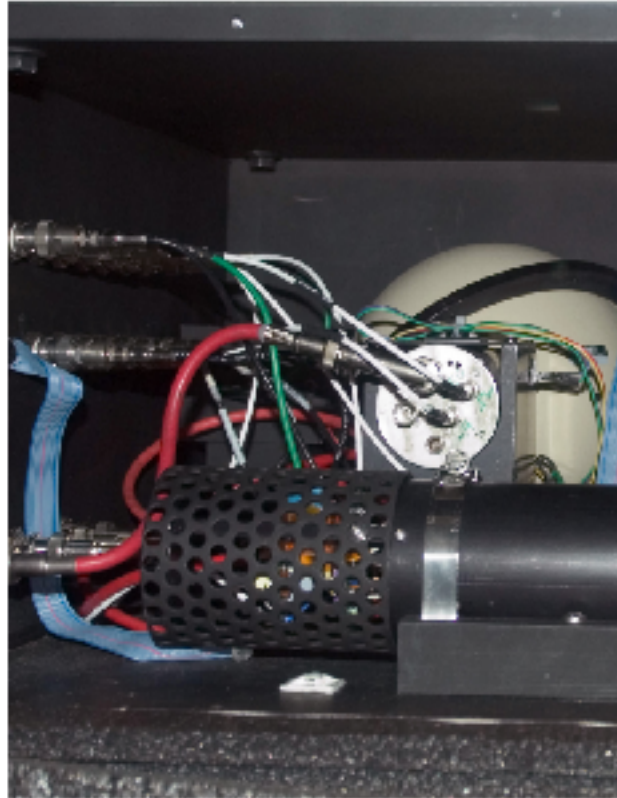


Figure 23: The light monitoring box mounted under seat of HYCAL.

5.2 Theoretical Calculations on Nuclear Form Factors and Backgrounds

5.3 Determination of $\Gamma_{\pi^0 \rightarrow \gamma\gamma}$

5.4 Results of high precision calibration experiments

5.4.1 The absolute cross section for pair production

The PrimEx experimental setup provides a unique opportunity to verify the luminosity normalization procedure (including both photon flux and target thickness) by measuring the absolute cross-section for a well known electromagnetic process, namely $(e^+ e^-)$ pair-production, without any additional hardware development.

Cross-section calculations for the photo-production of e^+e^- - pairs on ^{12}C at photon energies of few GeV and small momentum transfer $|\vec{Q}| \sim 10\text{keV}$ relevant for the PrimEx experiment were provided by A. Korchin¹[?]. A summary of different contributions included in the cross-section calculation are listed below in decreasing order of significance:

- Bethe-Heitler mechanism for pair production on the nucleus. Two models, Thomas-Fermi-Moliere and Hartree-Fock, for the atomic form factor describing charge distribution of electrons were considered to account for screening effects due to atomic

¹A. Korchin, Kharkov Institute of Physics and Technology, Kharkov 61108, Ukraine.

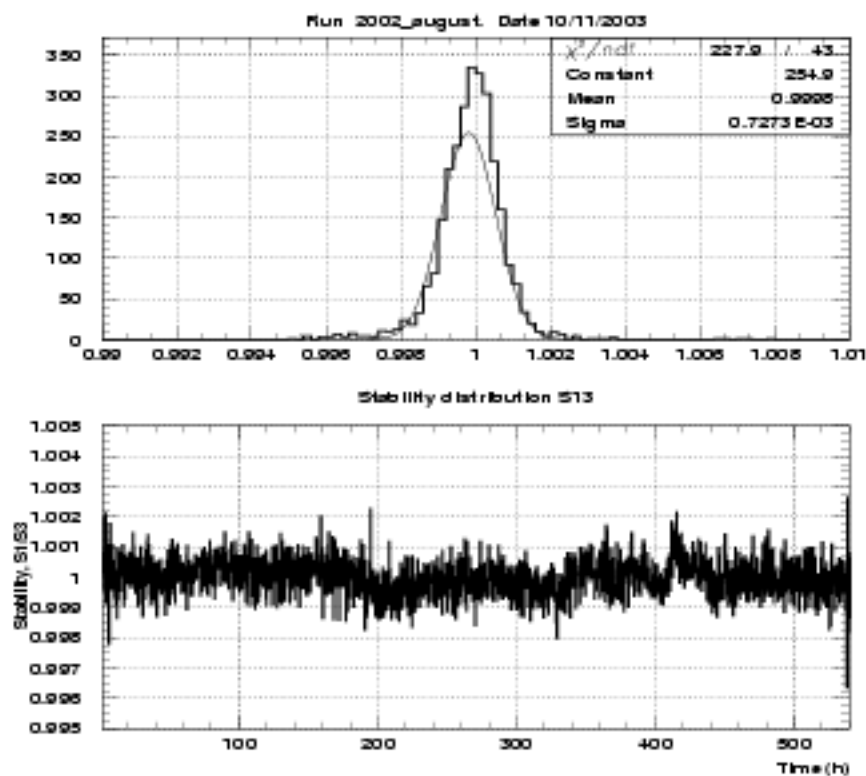


Figure 24: Stability of the light monitoring system.

electrons. The Coulomb distortion effects have been included according to work of Bethe and Maximon (contribution to the e^+e^- cross-section of $\sim 80\%$).

- Pair production on atomic electrons taking into account the excitation of all atomic states and correlation effects due to presence of other electrons and the nucleus (contribution of $\sim 20\%$).
- QED radiative corrections (of order α/π with respect to the dominant contributions): (i) virtual-photon loops and (ii) real-photon process $\gamma + A \rightarrow e^+ + e^- + A + \gamma'$, (contribution of $\sim 1 - 2\%$).
- Nuclear incoherent contribution - quasi-elastic, or quasi-free process on the proton $\gamma + p \rightarrow e^+ + e^- + A + p$ (contribution of $< 0.05\%$).
- Nuclear coherent contribution, *i.e.* virtual Compton Scattering, a two-step process $\gamma + A \rightarrow \gamma^* + A \rightarrow e^+ + e^- + A$ (contribution of $\sim 10^{-5}\%$).

As an example, figure 40 shows the calculated energy distribution of electrons produced by 5.46GeV photons on ^{12}C target. The calculations based on three different models of atomic form factors are shown: Hartree-Fock (HF), Thomas-Fermi-Moliere (TFM) and a simpler monopole approximation introduced by Tsai. As one can see from the figure, the



Figure 25: The PrimEx photon beam position detector.

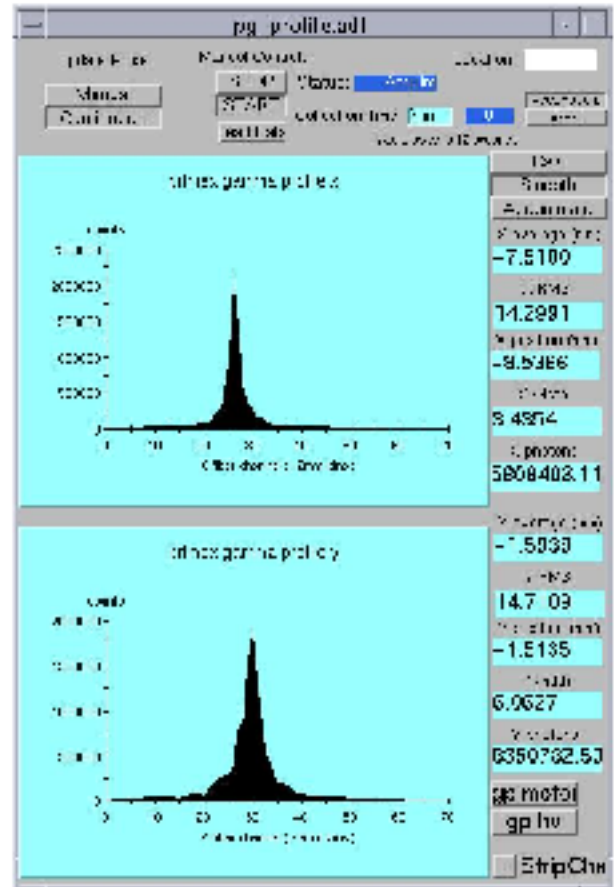


Figure 26: Photon beam position on-line display.

cross section slightly decreases compared to TFM if the HF form factor is used. The difference between the cross-section based on Hartree-Fock atomic form factor and the one based on Thomas-Fermi-Moliere model is of the order of $< 1\%$ which is indicative of the accuracy of the calculations.

A schematic of a pair-production event as seen by the PrimEx experimental setup (upstream of the tagger) is shown in Figure 41. For pair-production cross-section measurements, both the incident photon energy and timing information were determined by the tagger. The strength of the magnetic field of the PS dipole was lowered (to ~ 0.220 and $0.293 \text{ Tesla} \times \text{m}$) and the electron-positron pairs were swept into the calorimeter where the energy and position of the each particle was measured. The trigger signal, a coincidence between Tagger MOR and HyCal, recorded in a TDC provides timing information of the $e^+ e^-$ pair (see Figure ??).

Figure 42 shows distribution of X and Y coordinates and the energy position correlation for events with incident photon energy in the range $5.145 - 5.201 \text{ GeV}$, i.e. energy bin 5 after a timing cut of $(-5\sigma, +8\sigma)$. The negative X coordinates correspond to positrons and the positive X coordinates represent electrons.

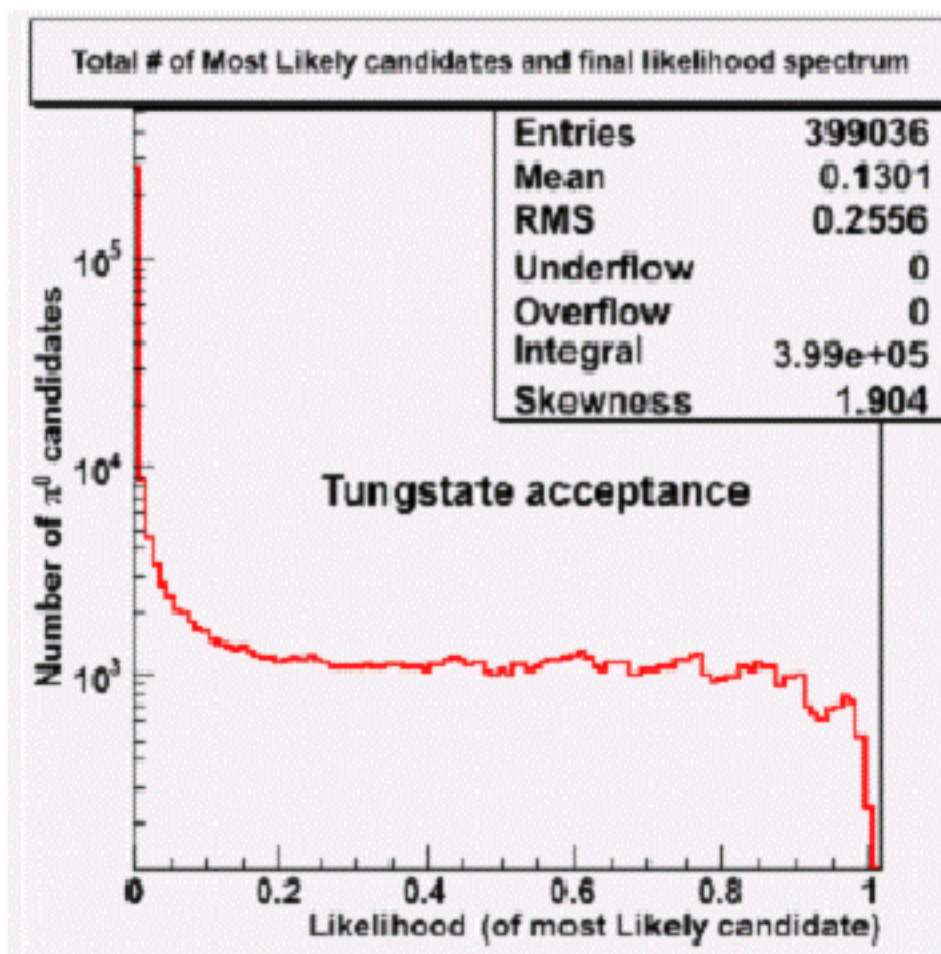


Figure 27: .

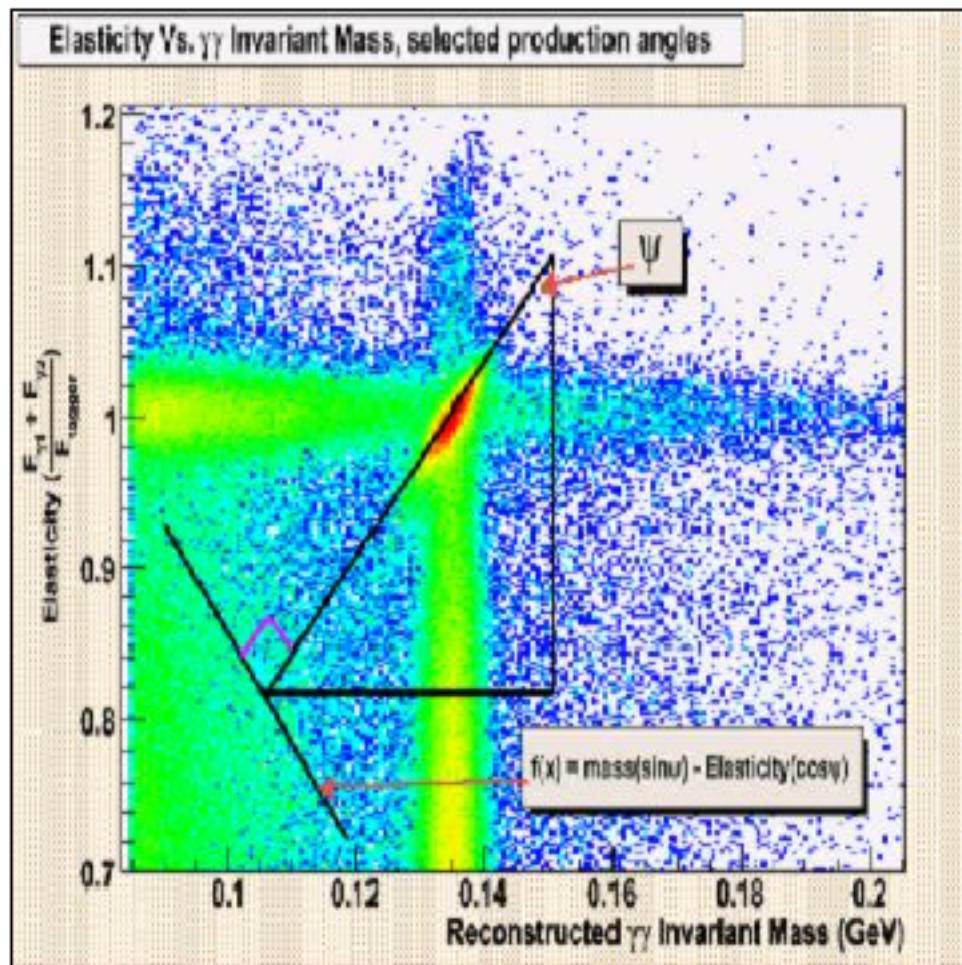


Figure 28:

2-D data rotated onto single orthogonal axis -- Hybrid Mass

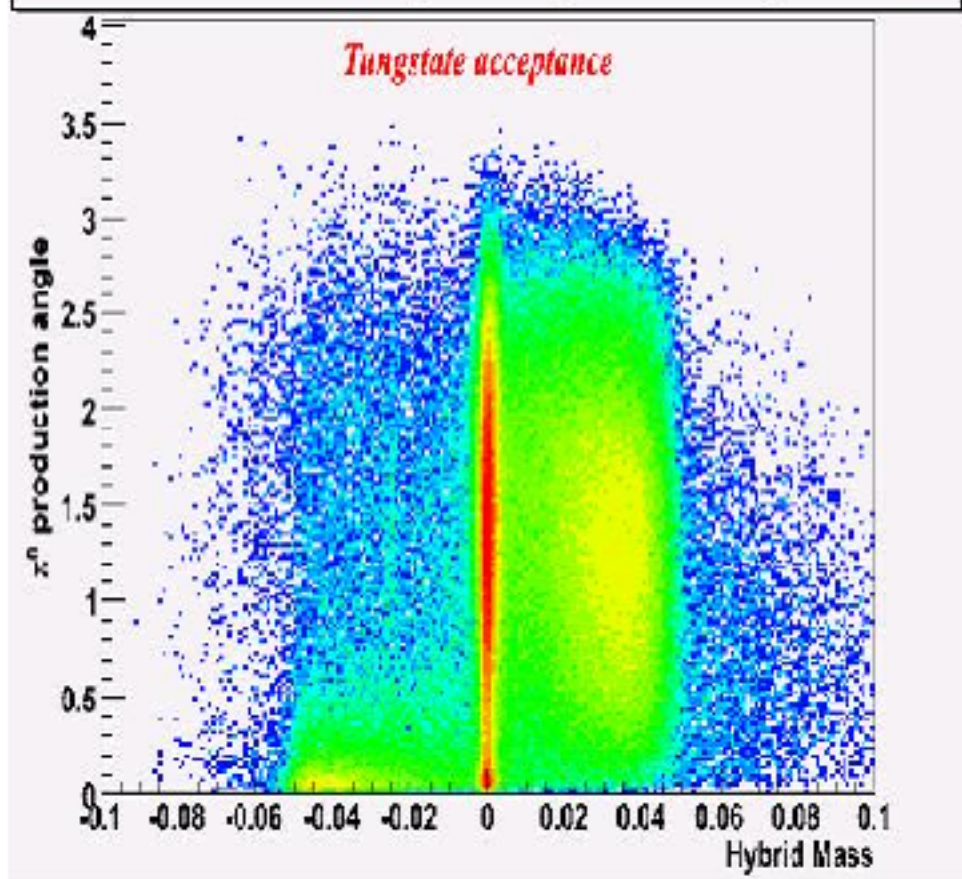


Figure 29:

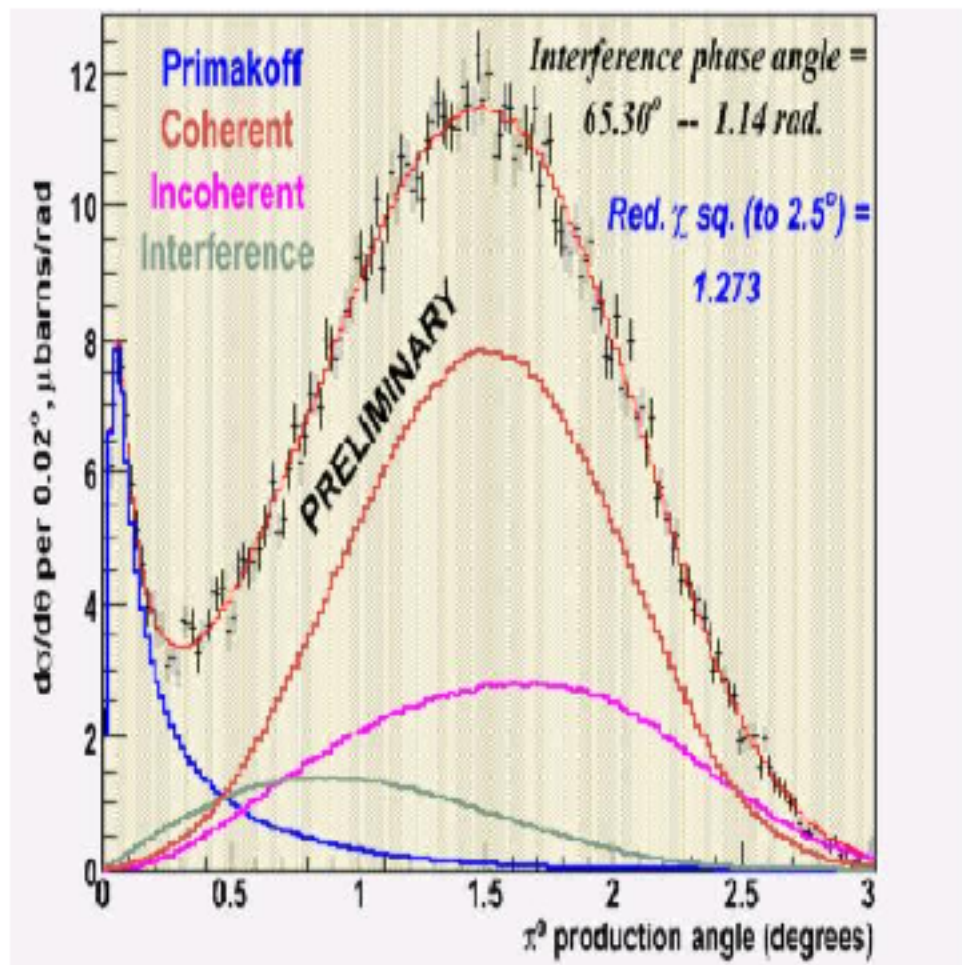


Figure 30:

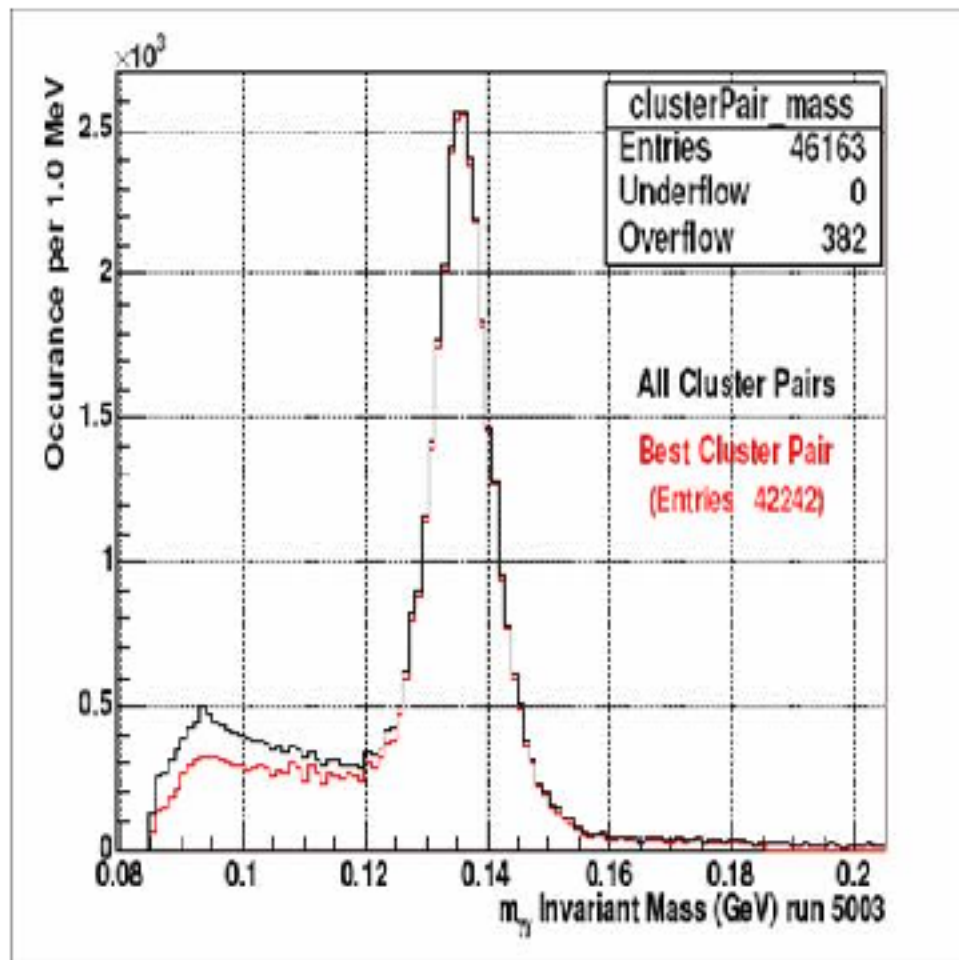


Figure 31:

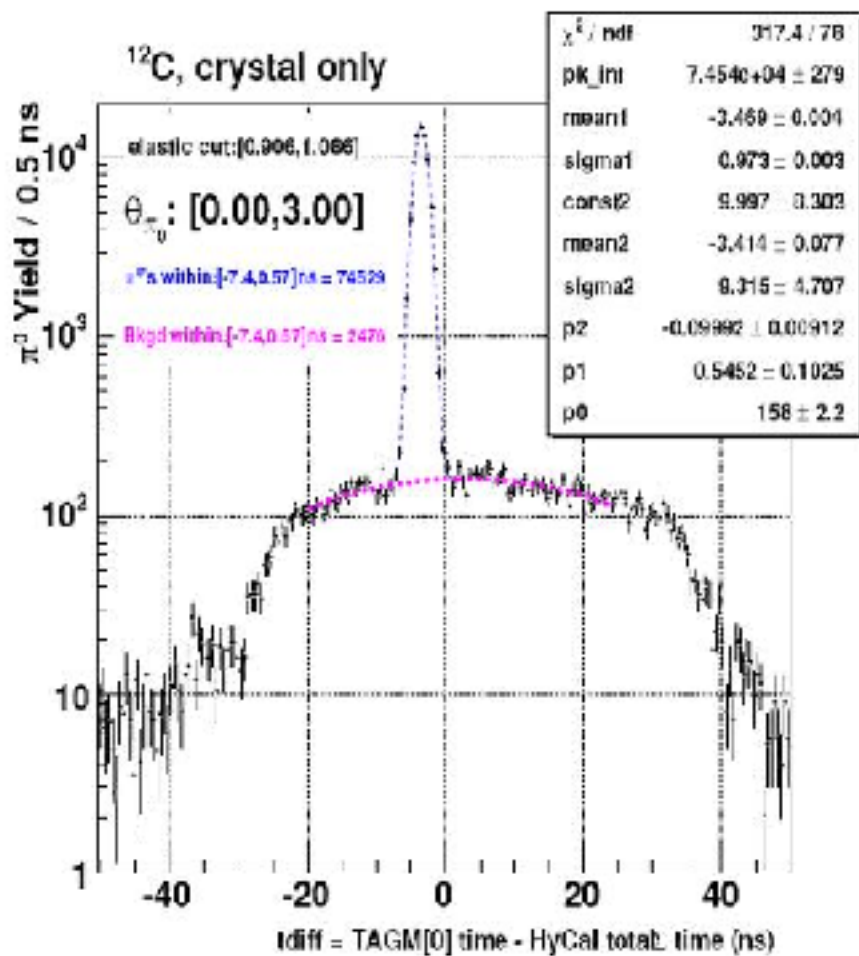


Figure 32:

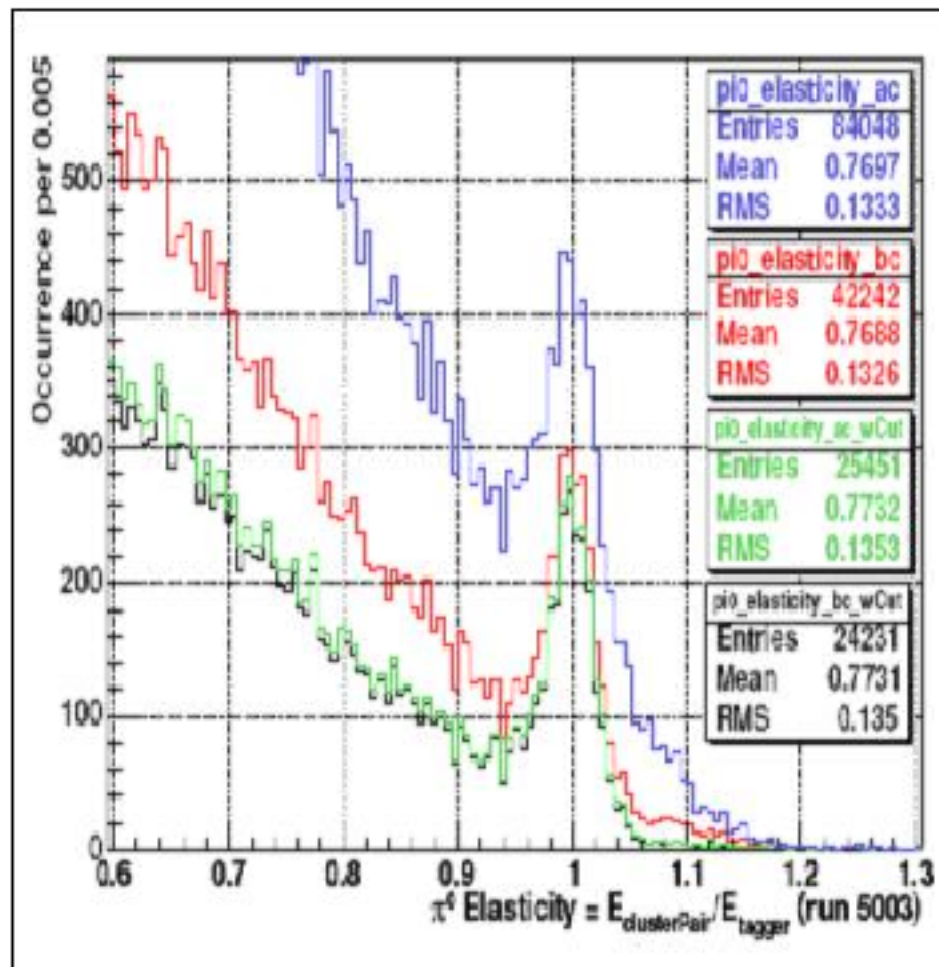


Figure 33:

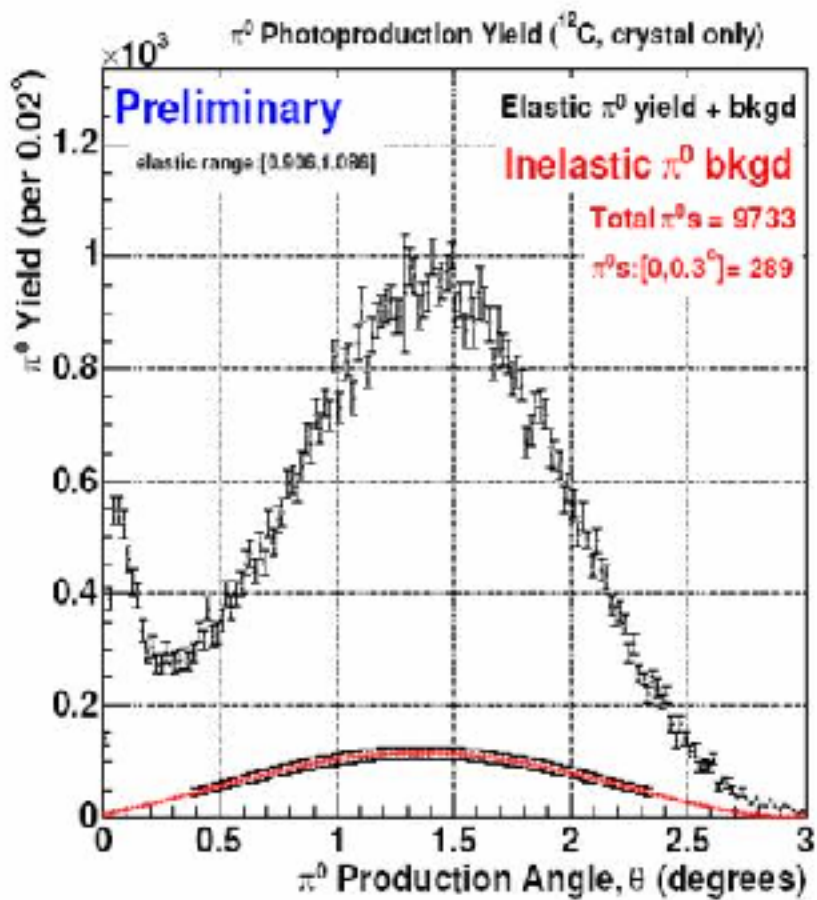


Figure 34:

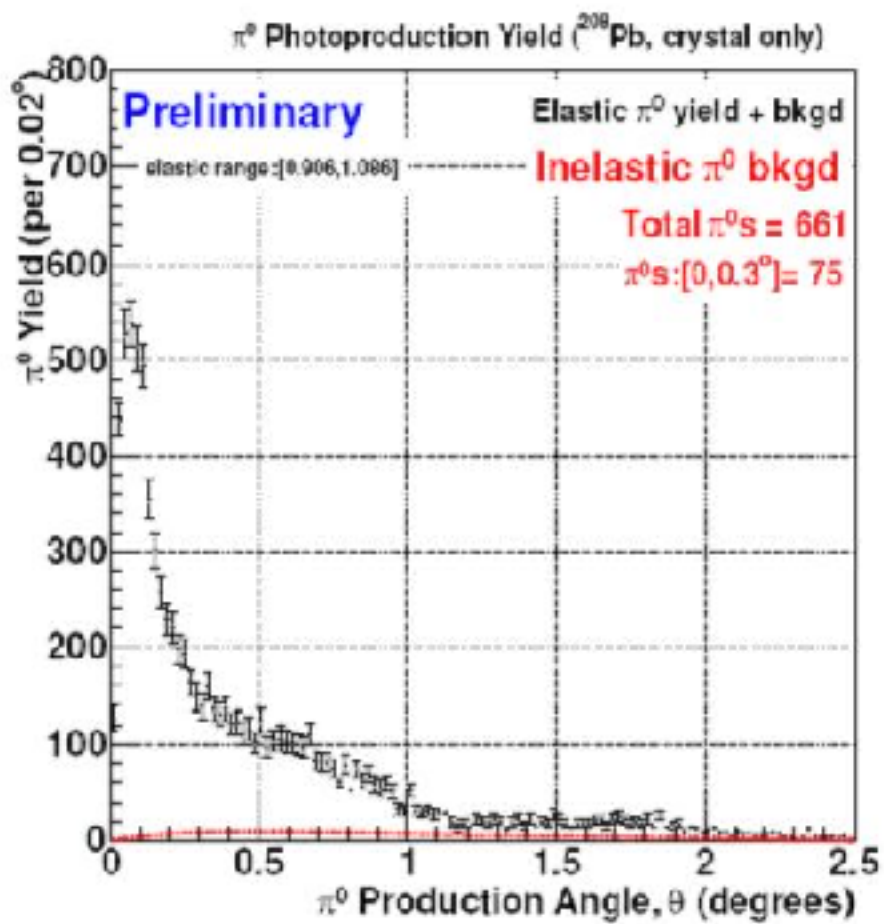


Figure 35:

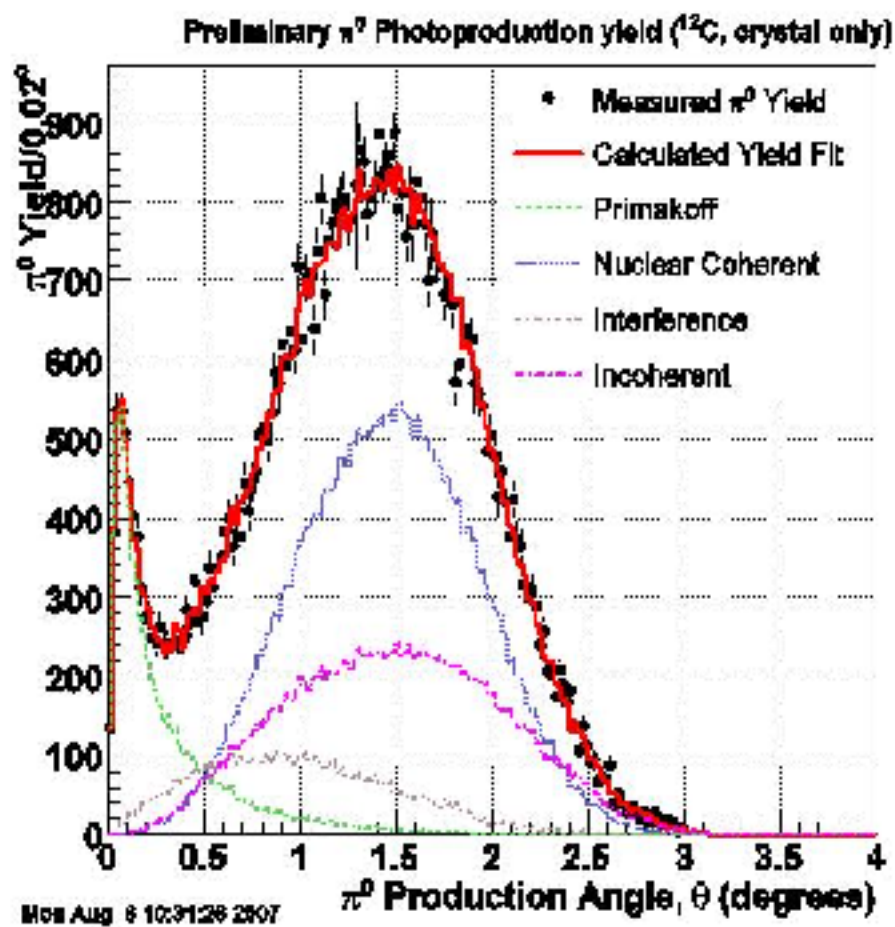


Figure 36:

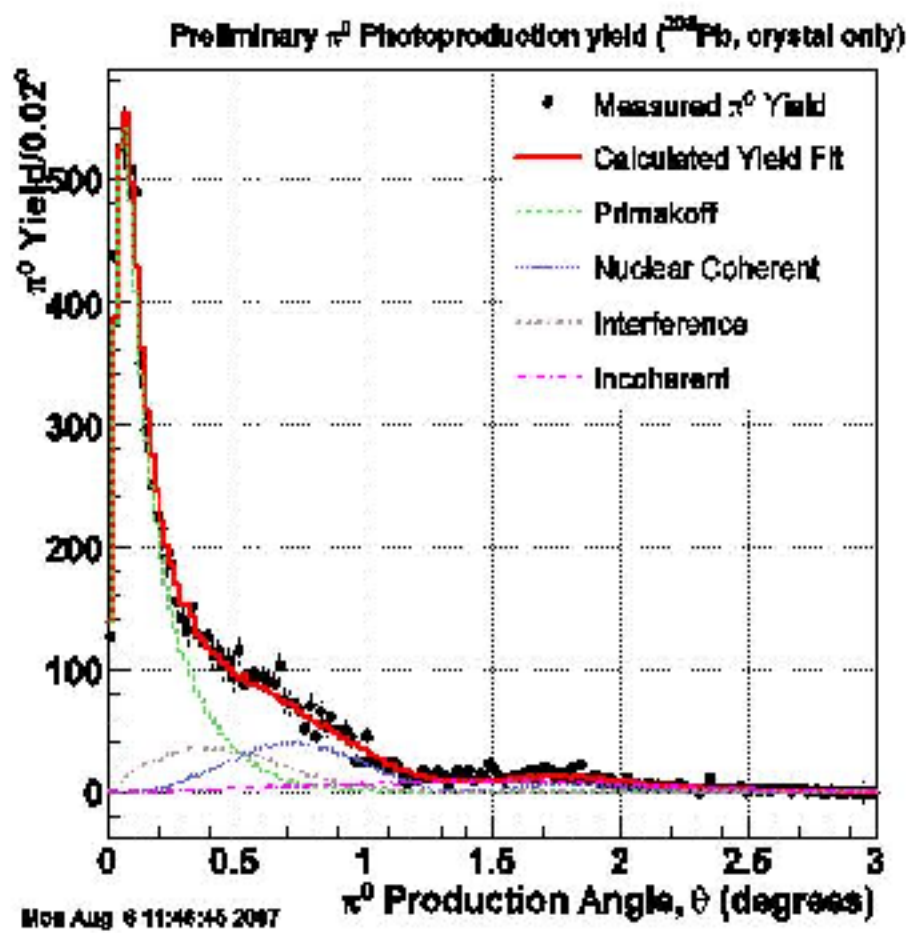


Figure 37:

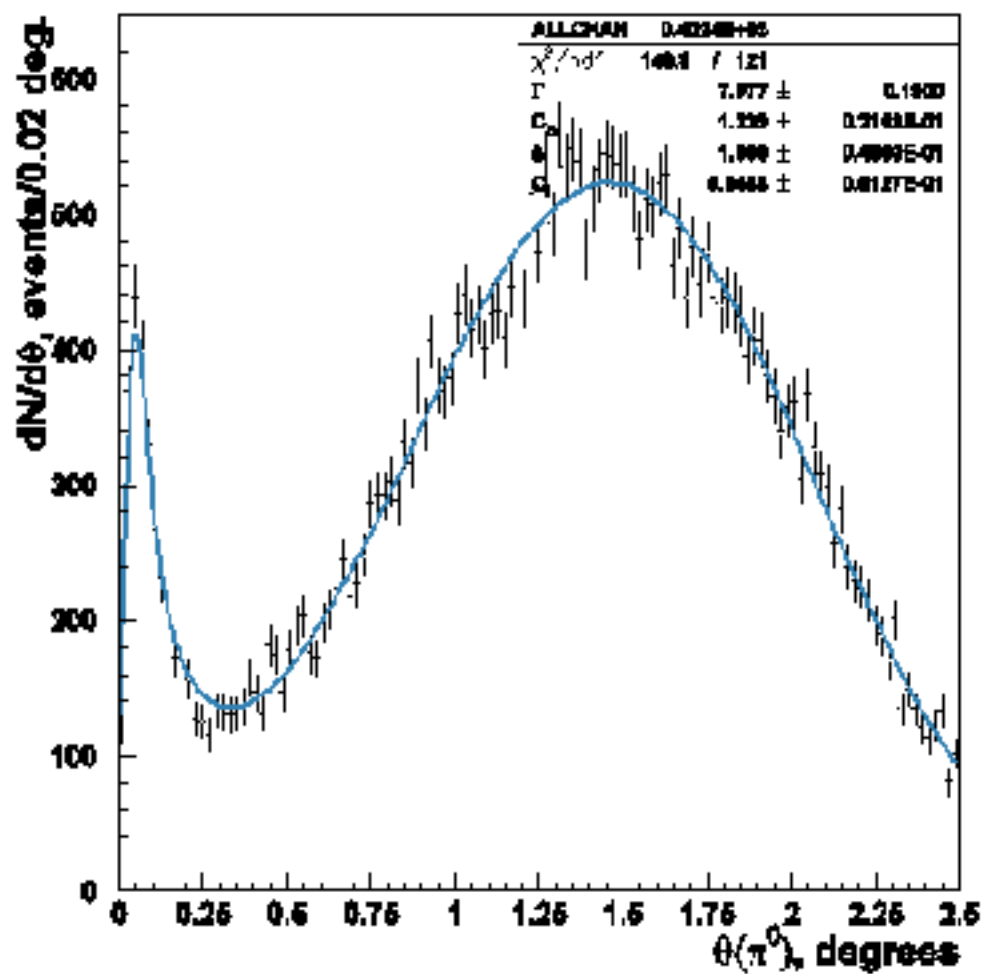


Figure 38:

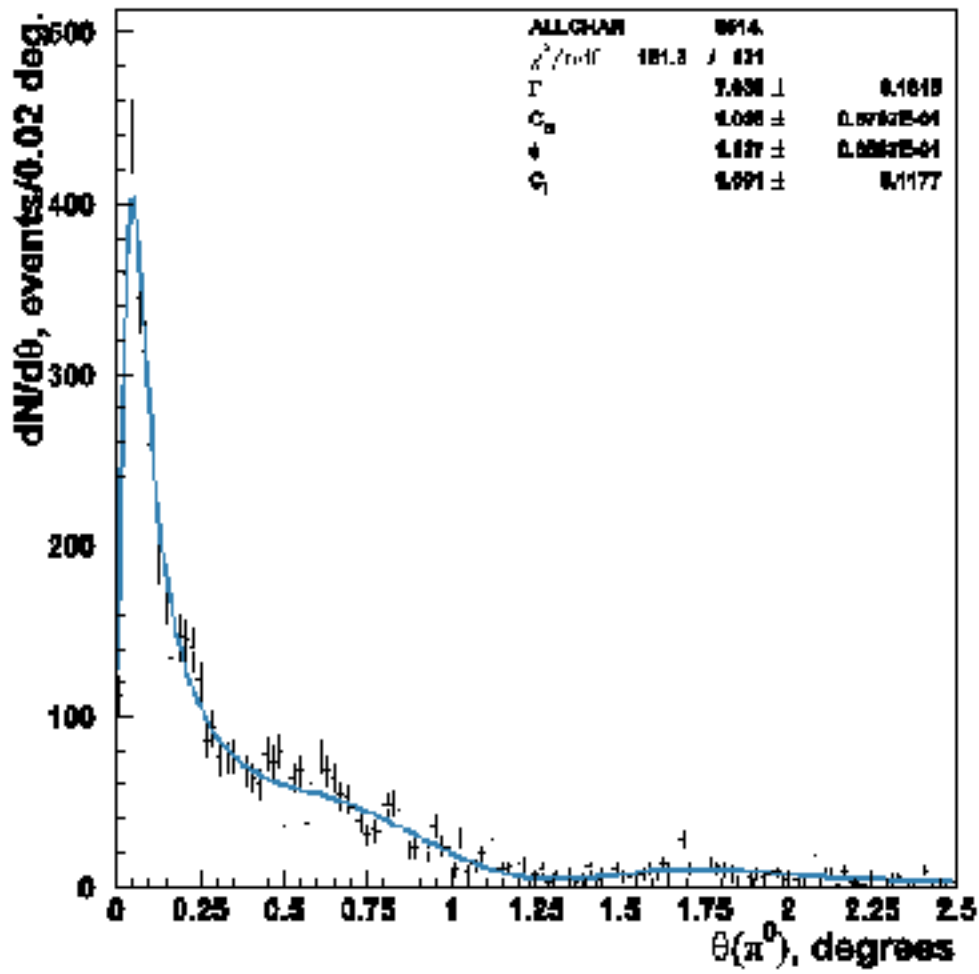


Figure 39:

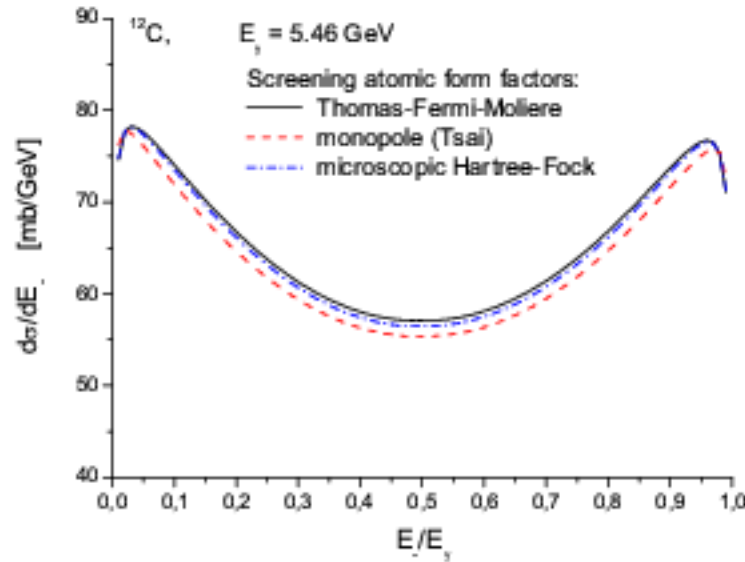


Figure 40: Calculated energy spectrum of electrons in pair-production on ^{12}C for 5.46GeV photons.

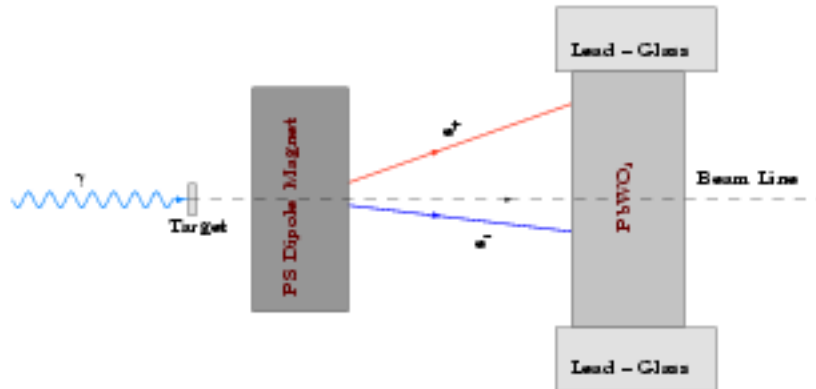


Figure 41: Schematic of a pair-production event as seen by PrimEx experimental setup (top view).

In part (a) of Figure 42 one can see a ring of “Compton” photons around the central opening of the HyCal and a faint line with negative slope due to pair-production generated by the halo of the beam hitting the photon beam collimator upstream of the experimental target. The electrons and positrons created by the halo on the collimator are first deflected in the field of the permanent magnet in the vertical direction and then by the Pair Spectrometer dipole magnet in horizontal direction creating the sloped line.

To eliminate the e^+e^- -pairs created by beam halo and most of Compton photons, a cut on the Y coordinate of particles $|y| < 5\text{cm}$ was used. Pair production data were taken with various settings of Pair Spectrometer dipole. For the highest field setting of $\sim 0.293\text{ Tesla}\times\text{m}$ momenta of 1.6GeV and less correspond to deflections of particles in the field of the dipole of $\sim 37.17\text{cm}$ or more, *i.e.* deflections into the outer Lead-Glass layer of the calorimeter. A cut

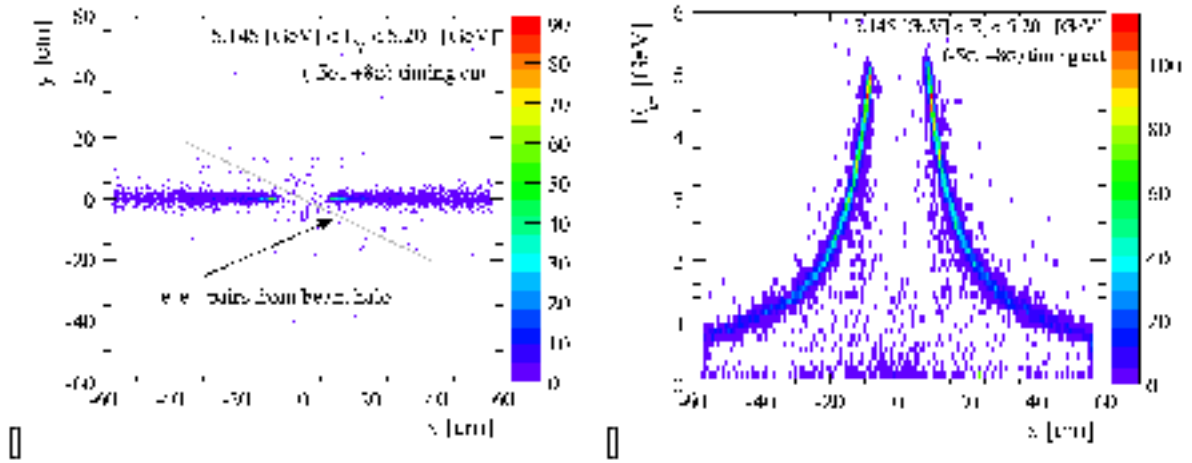


Figure 42: (a) Distribution of X and Y coordinates of clusters reconstructed in HyCal. (b) Correlation of energy and deflection in the magnetic field for clusters reconstructed in HyCal.

of $E_{e\pm} > 1.695\text{GeV}$ on the energy of leptons limits the analysis to the inner, high resolution, lead-tungstate layer of the HyCal which extends out to $\pm 35.275\text{cm}$ and enables comparison of data from runs with different field setting.

Compton electrons take most of the energy at the kinematic regime of the PrimEx experiment, thus a cut $E_{e\pm} > 1.2\text{GeV}$ would also eliminate a large amount ($\sim 59.9\%$) of Compton photons, some of which would otherwise be reconstructed in lead-tungstate part of the calorimeter. It is worth noting that the distributions of x and y coordinates for Compton photons are identical due to azimuthal symmetry of Compton scattering.

The final step toward the yield extraction is the subtraction of the background due to Compton scattering under the electron arm. For this purpose the energy distribution of Compton electrons was generated for each photon energy bin and smeared with the detector resolution function. The resulting distribution, shown in Figure ??, is subtracted from data with appropriate scaling factor.

The number of atoms per unit area in Carbon target is: $0.1066 \times 10^{24} (\pm 0.053\%) \left[\frac{1}{\text{cm}^2}\right]$. Knowing the photon flux one can easily convert yields into cross-sections. But before the cross-section obtained in the experiment can be compared to the one calculated by theory, one needs to take into account the effects of HyCal resolution and the energy losses of electrons and positrons before they reach the calorimeter due to secondary interactions in the target and the helium. To do so the *GEANT4* has been utilized.

First a photon energy is picked according to the spectrum of photons present in the data. Then an electron is generated with a fraction of photon energy according to the theoretical spectrum. The energies of the electrons, recorded in the simulation at the surface of the calorimeter, are smeared according to resolution function of the calorimeter. The generated yields were normalized to obtain a differential cross-section according to the calculated total cross-section for $E_{\gamma} = 5.18\text{GeV}$.

One can see that, for electrons or positrons with energy fraction $0.9 < x < 1.0$ the percent difference between calculated cross-section and one modified by energy losses and

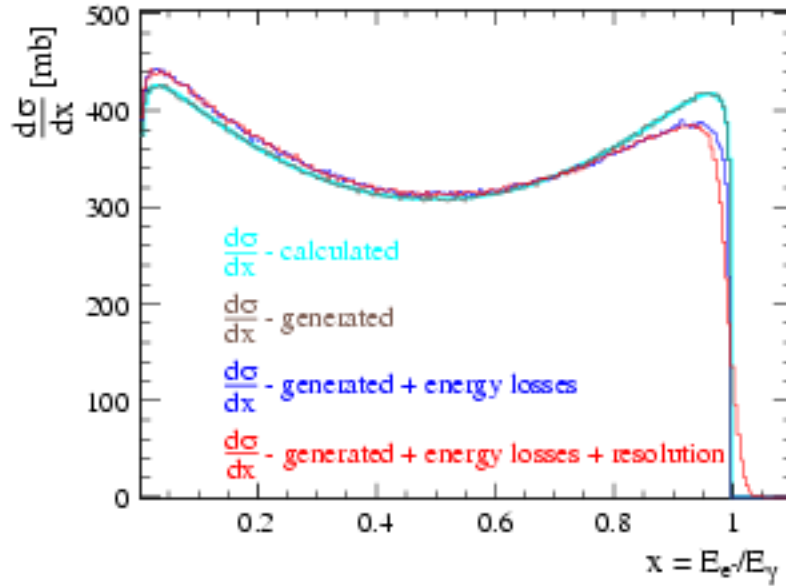


Figure 43: Absolute cross-section for pair-production differential in fraction of energy of photon taken by the electron for $E_\gamma = 4.91 - 5.46 \text{ GeV}$. The effect of energy losses in the target and the helium “buffer” is also shown as blue histogram.

Table 1: Total cross-section for pair-production calculated for the central values of the 10 energy bins.

Energy bin ID	E_γ avg. GeV	$\sigma_{\text{total}}^{e^+e^-}$ mb
1	4.91	351.106
2	4.97	351.176
3	5.03	351.244
4	5.11	351.328
5	5.18	351.408
6	5.23	351.461
7	5.28	351.513
8	5.34	351.574
9	5.41	351.644
10	5.46	351.692

detector resolution is changing rapidly ($5\% < \tau < 50\%$). Hence, for this region of x one could expect up to 2 – 5% discrepancy between experimental cross-sections and theory (modified by energy losses and resolution) due to the uncertainty of the *GEANT4* calculation of the energy losses. To minimize the potential systematic errors it is preferable to compare the experiment and theory for $0.3 < x < 0.85$ where the effect of the energy losses on the cross-section is less than 5%.

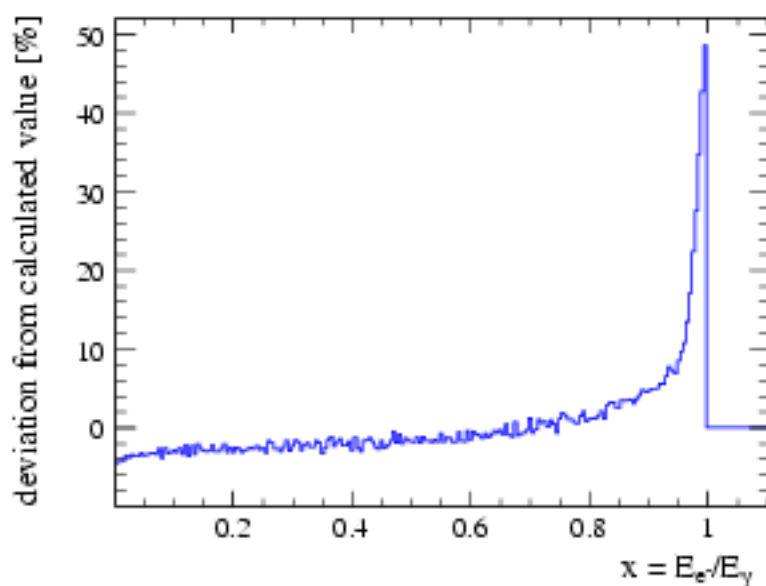


Figure 44: Percent deviation of the differential cross-section convoluted with energy losses and detector resolution from the calculated value.

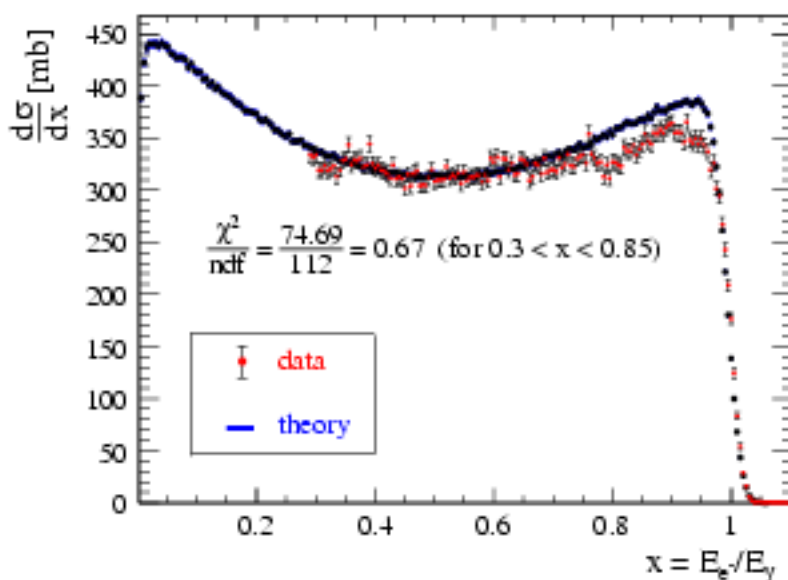


Figure 45: Differential cross-section for e^+e^- -production extracted on electron arm.

Table 2 lists the theoretical and experimental pair production cross-sections for various runs integrated between x_{min} and x_{max} . Where x is the fraction of energy of the incident photon taken by the electron ($x = E_{e^-}/E_\gamma$).

Table 2: Pair production cross-section integrated between x_{\min} and x_{\max} .

Run Number	x_{\min}	x_{\max}	$\sigma_{\text{experiment}}[mb]$	$\sigma_{\text{theory}}[mb]$	$(1 - \sigma_{\text{experiment}}/\sigma_{\text{theory}})[\%]$
5142	0.3	0.85	181.897	185.754	2.10
5314	0.3	0.85	188.568	185.754	-1.52
5142	0.4	0.85	149.311	152.7	2.22
5314	0.4	0.85	154.711	152.7	-1.32
5141	0.4	0.85	152.281	152.7	0.27

- Yield Statistics.

- Number of carbon atoms per unit area - (0.05%).

The number of atoms per unit area - n is given by:

$$n = \frac{N_{\text{atoms}}}{A} = \frac{\rho \ell}{m} \quad (15)$$

where A is the cross-section of the beam, ρ is the density of the target material, ℓ is the target thickness and m is the mass of the atom of the target material.

- Photon Flux.

The systematic error in photon flux determination, arising from the systematic uncertainty in the measurement of the absolute tagging ratios and the uncertainty in electron counting due to beam intensity variations, is 0.97%.

The statistical error on the photon flux in the pair-production data has a small contribution (0.06%) arising from the error on the absolute tagging ratios and is dominated by the electron counting statistics. The combination of both is given in Table ??:

- Background subtraction.

As previously discussed the background from Compton electrons is significant in the region of $x = E_e-/E_\gamma > 0.9$ (see Figure ??). Figure 46 shows that the relative contribution of the Compton electrons under electron arm for $0.3 < x < 0.85$ is not larger than 0.3%. Hence, a conservative 50% error in determination of the Compton electron background, due to low statistics of generated events, results in 0.15% or lesser error on the pair-production cross-section.

The background due to Compton photons in region $0.3 < x < 0.85$ is completely eliminated by cuts: $E_{\text{lepton}} > 1.2\text{GeV}$ and $|Y_{\text{lepton}}| < 5\text{cm}$.

- HyCal Resolution.

To study the effect of the HyCal resolution the *GEANT4* simulation was used. The integrated cross-section for pair-production was calculated for $0.3 < x < 0.85$ while smearing the energy of the particles with a gaussian. The width of the gaussian has

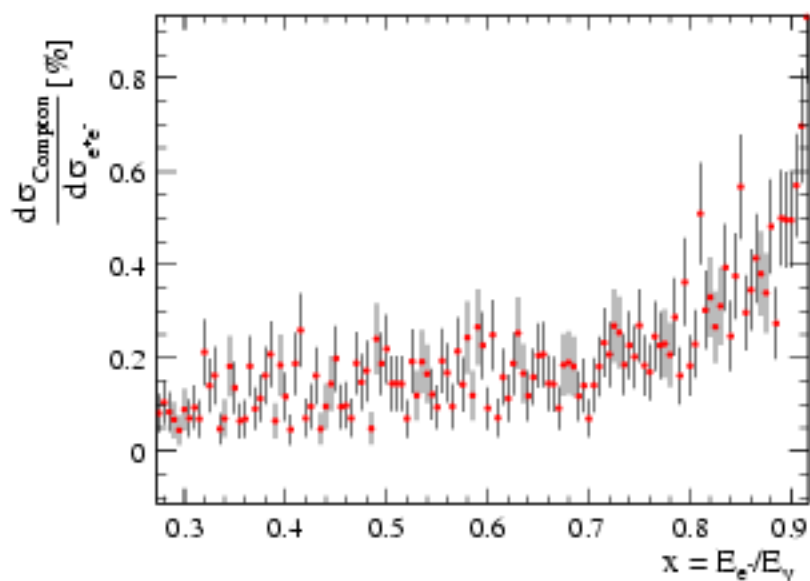


Figure 46: Ratio of Compton and pair-production yields for $0.3 < x < 0.85$.

been varied between 0.016 and 0.03 in increments of 0.002 to mimic the resolution of the calorimeter (1.6 – 3.0%). As one see from Table 3 the effect of the detector resolution on the cross-section is less than 0.12%.

Table 3: Effect of detector resolution on e^+e^- cross-section integrated between $x_{min} = 0.3$ and $x_{max} = 0.85$.

Smearing parameter [%]	σ [mb]
1.6	185.746
1.8	185.788
2.0	185.856
2.2	185.833
2.4	185.828
2.6	185.841
2.8	185.957
2.6	185.896

- Multi-photon events

The cross-section calculation was repeated accepting only events with 1 photon reconstructed in the tagger. The photon flux was recalculated. The procedure resulted in e^+e^- cross-section of 182.014 [mb] for $x_{min} = 0.3$ and $x_{max} = 0.85$ with a statistical error on the yield of (0.35%). The obtained cross-section is in excellent agreement (within

the statistical errors) with the value listed in Table 2. However, to be conservative one can assume an error of 0.06% due to photon reconstruction ambiguity.

- HyCal calibration.

If one assumes that all other effects have been accounted for or they are constant over time, the error on the cross-section, due to drifting detector gains, can be inferred by comparing the cross-sections from various runs integrated between same values of x_{min} and x_{max} (see Table 2). Assuming independent errors, for error due to detector calibration (plus all other time dependent systematic effects) one has an upper limit of 1.92%.

Table 4 summarizes the error on the experimental cross-sections listed in Table 2.

Table 4: Summary of errors.

	Effect	Error (%)
Statistical	Yield statistics	run dependent (~ 0.25)
	Photon flux ($R_{absolute}$ and electron counting)	run dependent (~ 0.37)
Systematical	Photon flux ($R_{absolute}$ and electron counting)	0.97
	Number of Carbon atoms in the target	0.05
	Background subtraction	0.15
	HyCal resolution	0.12
	Photon misidentification/double counting	0.06
	HyCal calibration	< 1.92
Total		$\sim \pm 0.44(stat.) \pm 2.16(sys.)$

- Error on the theoretical cross-section.

As previously mentioned, the error on the theoretical value of the cross-section due to the choice of the atomic screening form factor is on the order of $\sim 1\%$.

The experiment is being compared to a theoretical cross section convoluted with energy losses in the target. *GEANT4* provides an accuracy of 5 – 10%. To evaluate the effect of this error on convoluted theory, the energy losses in the simulation were artificially varied by $\pm 10\%$ and the theoretical cross section was recalculated for region $0.3 < x < 0.85$ resulting in a $\sim 0.32\%$ difference.

Thus the estimated uncertainty on the theory convoluted with energy losses in the target is 1.05%.

Given the above considerations the experimentally obtained cross-section, for $0.3 < x < 0.85$ is in remarkable agreement with theory.

5.4.2 Absolute cross section for electron Compton scattering

The key of the PrimEx experiment is to measure the absolute cross section of small angle π^0 photoproduction from complex nuclei. The invariant mass and angle of the pion will be reconstructed by detecting two decay photons from the $\pi^0 \rightarrow \gamma\gamma$ reaction in the HYCAL calorimeter. It is crucial to calibrate the overall systematic errors of the experimental setup by well known physics processes with similar kinematics and the same setup. We used atomic electron Compton scattering and the e^+e^- pair-production as tools to control systematic errors on absolute cross section measurement and the stability of the experimental setup.

The scattering of photons by free electrons $\gamma + e \rightarrow \gamma' + e'$ is one of the simplest and most basic quantum-electrodynamic processes that is experimentally accessible. The lowest order Compton scattering diagrams were first calculated by Klein and Nishina in 1929 [34], and by Tamma in 1930 [35]. There are two types of corrections to the basic Klein-Nishina formula which must be considered when studying Compton scattering at energies above 0.1 GeV. These are radiative corrections, and double Compton scattering contributions. The interference between the basic first-order single Compton scattering amplitude and the radiative and double Compton scattering amplitudes have been studied extensively in the literature [36]-[38], [39]-[40], and the errors on theoretical calculation are less than 1%. The total Compton cross section and forward cross section on ^{12}C with radiative and double Compton corrections calculated by different numeric methods[44][45] are compared as shown in figure 47 and figure 48. In the case of total cross section it is also compared to NIST values. They are in good agreement within 0.5%. As a result, Compton scattering provides an excellent mean to control the systematic error of PrimEx experiment on the cross section measurement, including the photon flux, target thickness, and HYCAL calorimeter detection efficiency.

The Compton data taken periodically once a week during our experiment in 2004. The pair-spectrometer magnet was off in order to detect both scattering photons and electrons in the HYCAL, and the lower beam intensity was used due to higher Compton cross section comparing with the π^0 production. The rest of the setup was the as same as the π^0 production runs. Detection of a Compton event is shown schematically in Figure 49. The energy and positions of the scattering photon and electron measured from the calorimeter, along with the beam energy determined by the photon tagger, provided a full kinematics on Compton event selection.

There are three groups in the collaboration analyzed the Compton data independently. The results of different analysis are in good agreement within their error bars. The preliminary result from one of the groups will be described in detail as below.

The Compton data set in this analysis were collected on a 5% R.L. carbon target with incident photon beam energies of 4.85 - 5.45 GeV. To select Compton events, the data were processed in two stages: (1) reduced skim data files, where loose cuts were applied on the raw data, and (2) Compton events selection, where optimized set of cuts were applied on skim data.

The cuts in the stage one included:

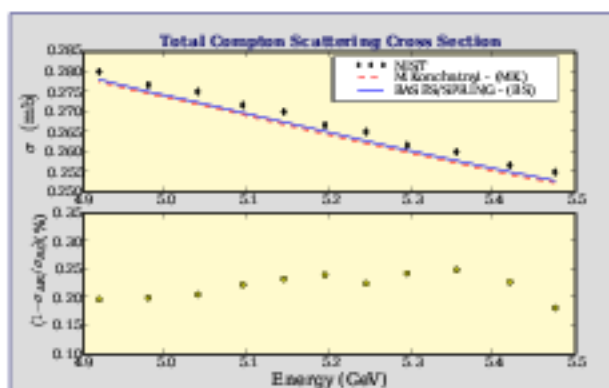


Figure 47: Comparison of theoretical calculations on Compton total cross with radiative corrections by different methods. The bottom plot shows the deviation between two different calculations is less than 0.3%.

Figure 48: Radiated Klein-Nishina cross section integrated over HYCAL solid angle.

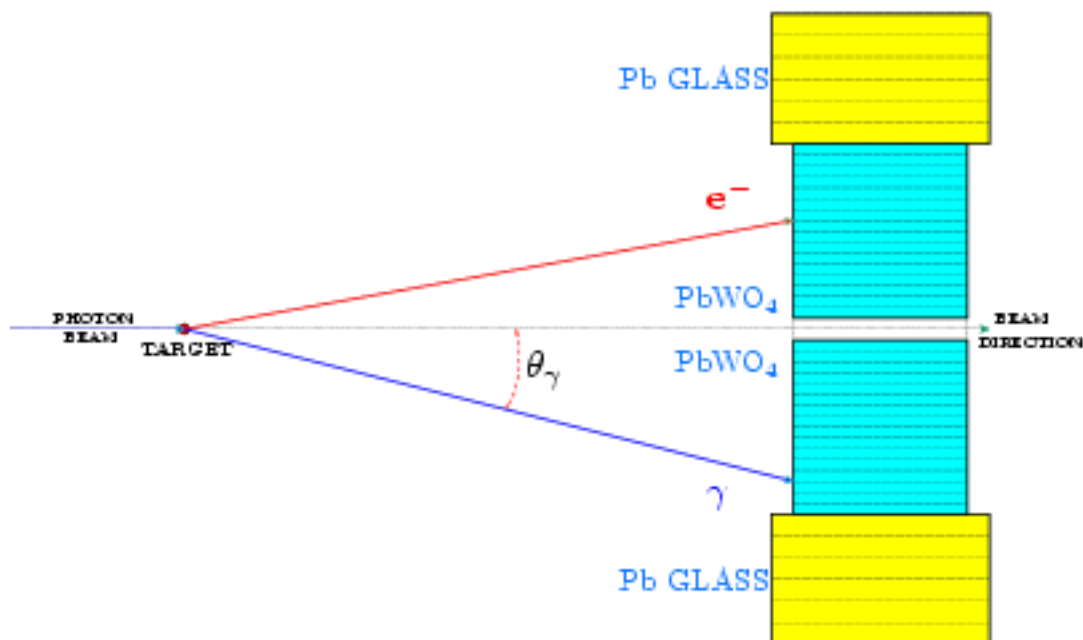


Figure 49: Detection of a single Compton event in HYCAL.

- $|tdiff| < 20$ ns, where $tdiff$ is the coincidence time between the photon tagger and HYCAL total sum,

- Total energy deposited on HYCAL $\sum_i E_i > 3.5$ GeV,
- $E_i > 0.5$ GeV, where $i = e', \gamma'$

The cuts in the stage two included:

- $|\text{tdiff}| < 5.35$ ns - 5σ coincident timing cut,
- $\Delta\phi < 25^\circ$ - 5σ coplanarity of e' , and γ' cut,
- 4.154 cm $< |x_i| < 33.232$ cm - HYCAL fiducial cut, $i = e', \gamma'$,
- 4.150 cm $< |y_i| < 33.200$ cm - HYCAL fiducial cut, $i = e', \gamma'$,
- -0.6 GeV $< E_{\text{TACG}} - E_0(E_1, x, y) < 1.2$ GeV - momentum conservation cut,
- 625 cm $< z_v < 825$ cm - interaction vertex cut,
- $R_{\text{min}} > 16.0$ cm - minimal separation of scattering e and γ on HYCAL,
- *criss-cross* cut aimed at removing the pair production background.

where z_v is the distance from the target to HYCAL calculated by using two cluster coordinates on the calorimeter; $E_0(E_1, x, y)$ is the initial photon energy derived from the knowledge of the energy of the higher energy cluster and the position information of both clusters on HYCAL. The GEANT Monte Carlo simulation indicates that the air production background shown in figure 50 mainly come from the collimator located upstream of the PrimEx target. The permanent magnet located between the collimator and the target bent the trajectories of electrons and positrons to HYCAL. Without the presence of magnetic field the pairs would had been undetected through the central opening in the calorimeter. About 25% of statistics were lost due to the cut to eliminate the pair production background. We plan to solve this problem in the future runs by increasing the magnetic field or replacing the permanent magnet with an active magnet. The last two cuts are shown in the figure 50.

To extract final Compton yield, the elasticity distribution ($\Delta E = E_0 - (E'_\gamma + E_e)$, where E_0 , E'_γ and E_e are measured energy of incident photon, scattering photon and electron) of the events, selected by using the cuts described above, were fitted with the signal and background distributions for every $\sim 1\%$ energy bin defined by one photon tagger T-counter. The signal distribution is generated by Monte Carlo simulation based on well known theoretical angular distribution of Compton scattering including the radiative correction and double Compton contribution, detector resolution and acceptance. The same Monte Carlo program was also used in π^0 data analysis. The shape of the background is modeled with the out-of-time events selected from the data using the same cuts described above except for timing, which was changed to $|\text{tdiff}| > 5.35$ ns. Monte Carlo and background distributions were then fit to the data using maximum likelihood, as shown in figure 51. This two-parameter fit maximizes likelihood function by finding the best overall strengths for the signal and background. Then the yield is obtained by the number of events in the data after background subtraction.

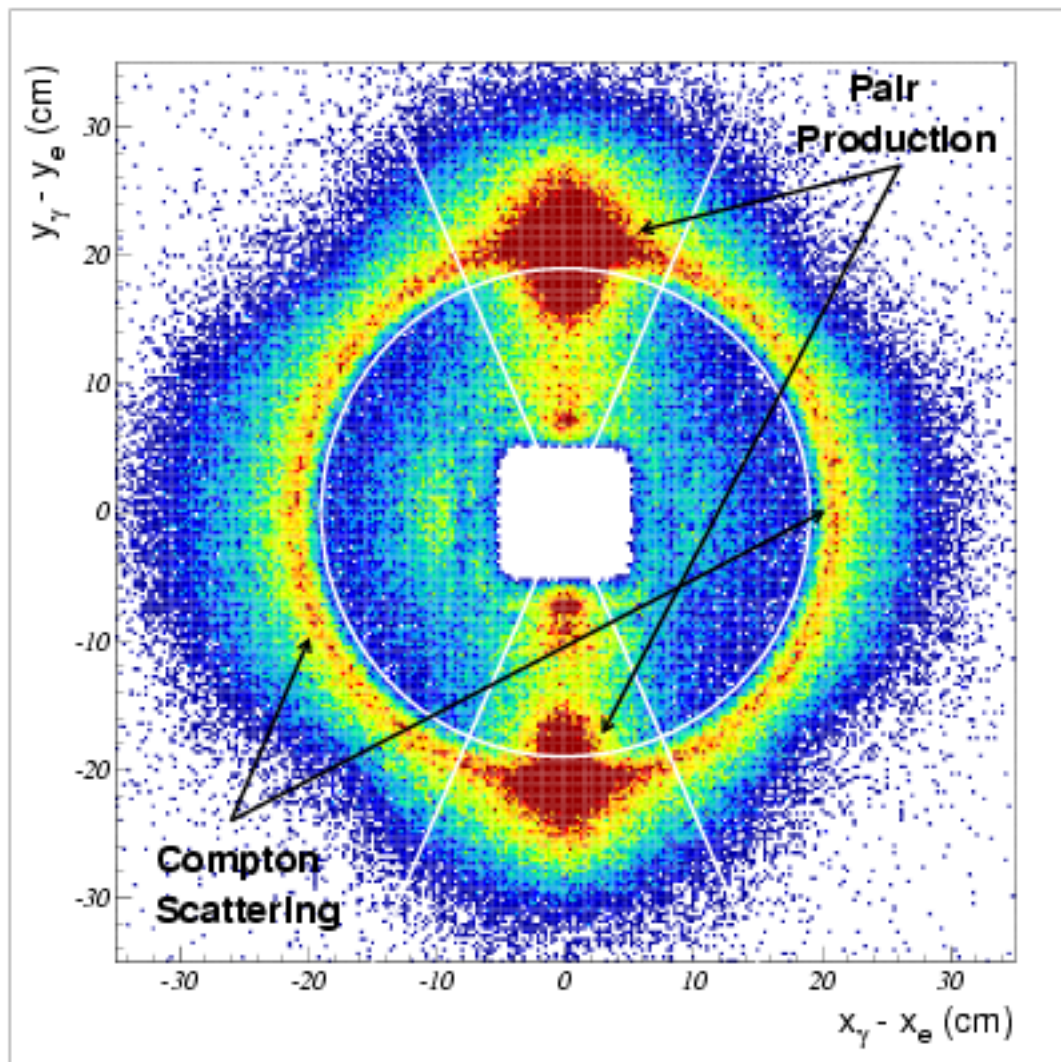


Figure 50: Event selection. Shown in the plot are two geometric cuts: (1) minimum separation cut - white circle, (2) criss-cross cut, white lines, that aims at removing pair production background events.

From the extracted yield combining with luminosity and detector acceptance, the preliminary results of total Compton cross section and average differential cross section in forward direction were obtained, see Figures 52 and 53. Both measured total cross section and forward differential cross section are consistently agree with theory predictions within 7%.

Various systematic error studies are performed for each measurement point with $\sim 1\%$ energy resolution defined by one tagger T-counter. It includes contributions listed below. The result of the systematic studies is detailed in Table 5. The average systematic error of one data point is 1.37%.

- incident photon flux,
- target composition and thickness,
- coincidence timing,

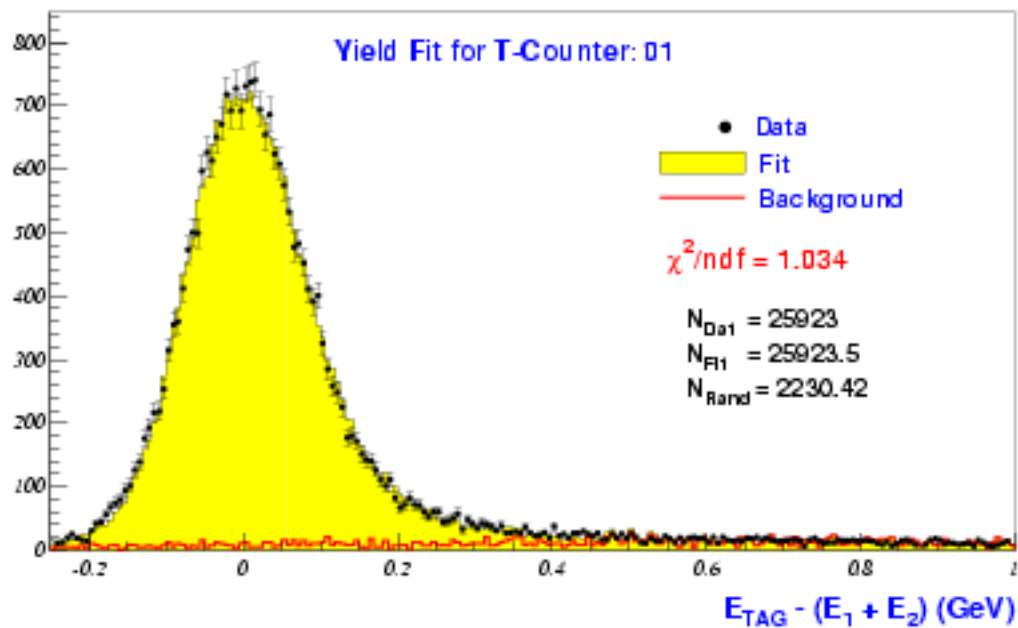


Figure 51: Yield fit, with background shown, for T counter 1.

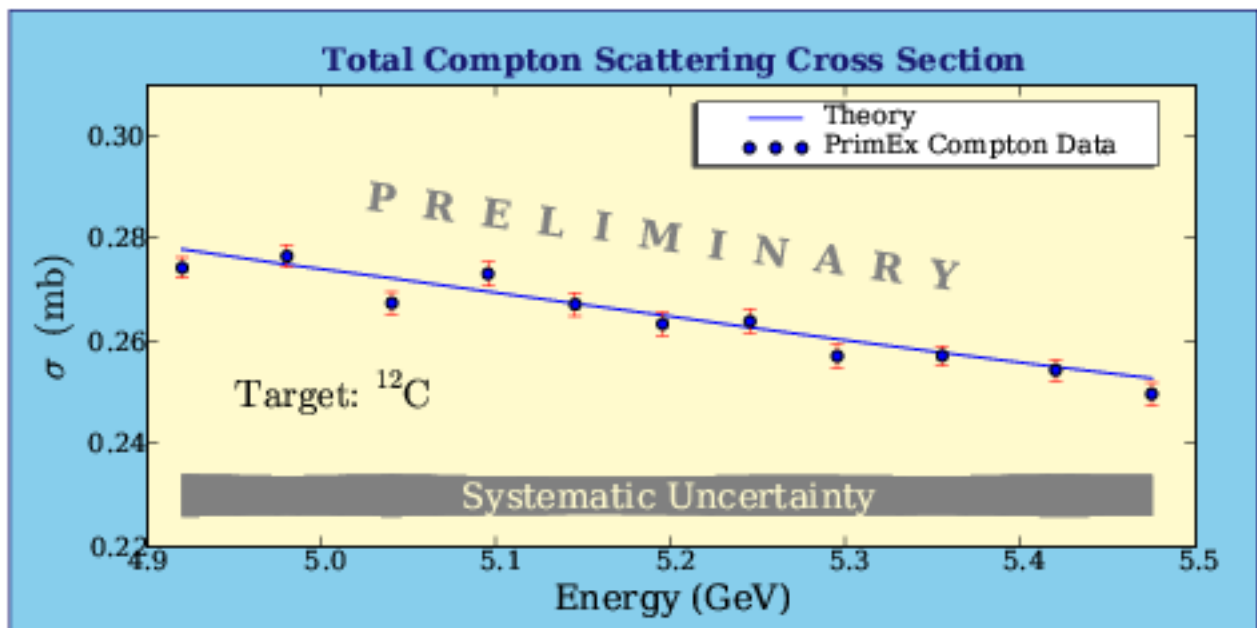


Figure 52: Total Compton cross section. The band on the plot represents the systematic uncertainty of the measurement. The energy resolution for each point is about 1%.

- coplanarity,
- the dependence of the cross section on radiative tail cut,
- geometric cuts stability,
- signal-background separation,

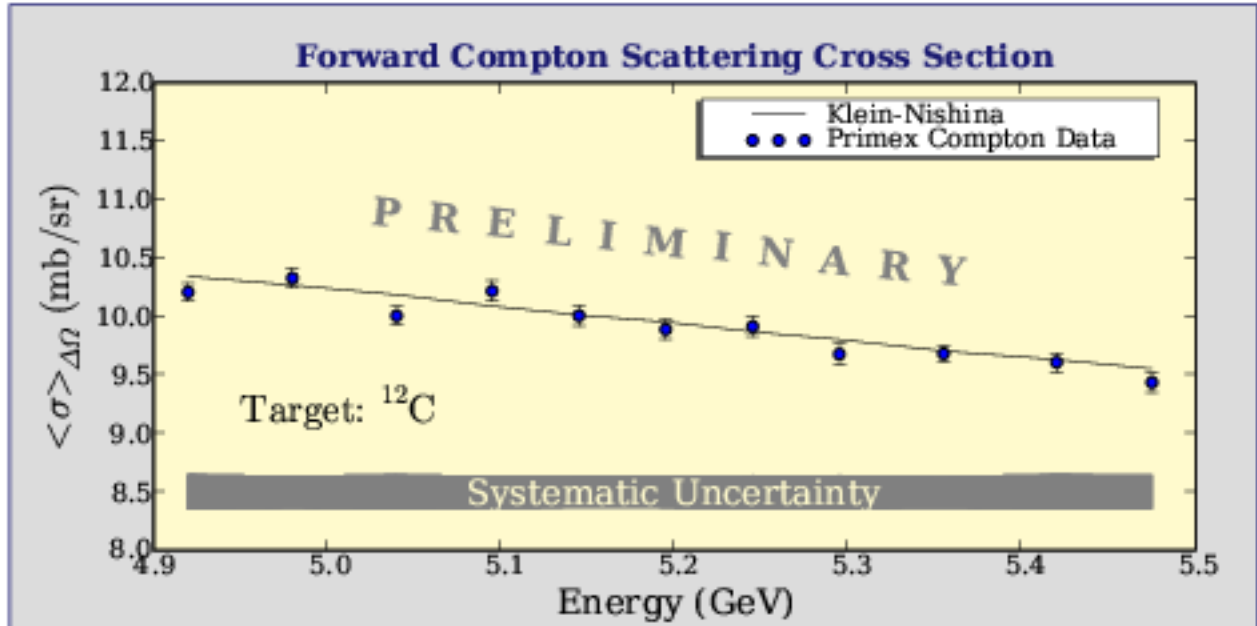


Figure 53: The forward Compton cross section averaged over the HyCal acceptance. The band on the plot represents the systematic uncertainty of the measurement.

- yield fit stability.

TCtr	Flux	Tgt	ΔT_{coin}	$\Delta\phi$	Rad. Tail	Geom.	Sg/Bg	Fit	Syst.	Stat.	Total
1	1.0	0.05	0.09	0.17	0.001	0.62	0.78	0.075	1.43	0.90	1.72
2	1.0	0.05	0.01	0.18	0.010	0.68	1.01	0.075	1.59	0.84	1.83
3	1.0	0.05	0.01	0.13	0.095	0.53	0.60	0.075	1.29	0.73	1.55
4	1.0	0.05	0.03	0.17	0.340	0.31	0.74	0.075	1.35	0.92	1.65
5	1.0	0.05	0.13	0.18	0.033	0.71	0.52	0.075	1.36	0.86	1.64
6	1.0	0.05	0.08	0.17	0.310	0.30	0.40	0.075	1.18	0.85	1.50
7	1.0	0.05	0.03	0.19	0.120	0.60	0.24	0.075	1.22	0.87	1.53
8	1.0	0.05	0.03	0.17	0.130	0.65	0.41	0.075	1.28	0.86	1.58
9	1.0	0.05	0.08	0.16	0.230	0.35	1.05	0.075	1.52	0.80	1.77
10	1.0	0.05	0.03	0.21	0.027	0.56	0.60	0.075	1.31	0.79	1.59
11	1.0	0.05	0.06	0.21	0.160	0.42	1.07	0.075	1.55	0.74	1.77

Table 5: Systematic uncertainties for each T-counter. All values are in %. Statistical error accounts for yield and photon flux fluctuations.

To increase the statistics, every two T-counts are combined together. The extracted total Compton cross sections are shown in figure 54. Both systematic and statistical errors of each data point are described in Table 6. The average total error is 1.41% for each point with $\sim 2\%$ energy resolution.

In addition, by measuring Compton cross section periodically allows one to monitor the stability of the experimental setup. Figure 55 shows the total Compton cross section

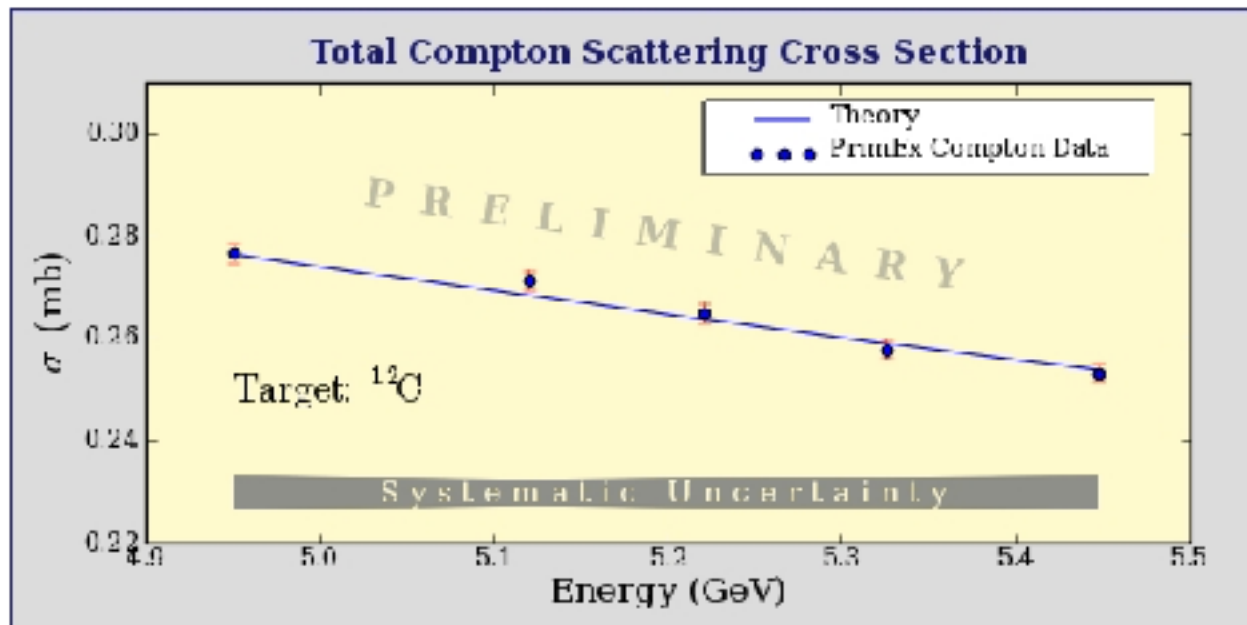


Figure 54: Total Compton cross section. The band on the plot represents the systematic uncertainty of the measurement.

TCtr	Flux	Tgt	ΔT_{coin}	$\Delta\phi$	Rad. Tail	Geom.	Sg/Bg	Fit	Syst.	Stat.	Total
1-2	1.0	0.05	0.03	0.065	0.098	0.91	0.46	0.063	1.44	0.61	1.56
3-4	1.0	0.05	0.03	0.065	0.098	0.68	0.42	0.063	1.29	0.57	1.41
5-6	1.0	0.05	0.03	0.065	0.098	0.46	0.40	0.063	1.18	0.60	1.32
7-8	1.0	0.05	0.03	0.065	0.098	0.33	0.37	0.063	1.13	0.61	1.28
10-11	1.0	0.05	0.03	0.065	0.098	0.85	0.36	0.063	1.37	0.54	1.47

Table 6: Systematic uncertainties for combined two T-counters. All values are in %. Statistical error accounts for yield and photon flux fluctuations.

changes over the run numbers. The measured values at latter runs consistently higher than predicted values, which can be directly associated with the beam leakage from other hall during the latter period of the experiment identified by the pair-production luminosity monitoring technique described in this proposal.

In conclusion, the total cross section and forward differential cross section of Compton scattering in 4.85 - 5.45 GeV energy range were measured with PrimEx setup. They are in excellent agreement with theory predictions with 7% precision. For each data point with a energy resolution of 2% defined by two T-counters, the average systematic error is 1.28%, the statistical error is 0.59%, and the average total error is 1.41% (see Table 6). Since Compton scattering in this energy range completely mimic the π^0 lifetime experiment, the precision obtained from the Compton measurement demonstrates that the PrimEx experimental setup has the capability to measure the absolute cross section π^0 production with a 1.4% accuracy.

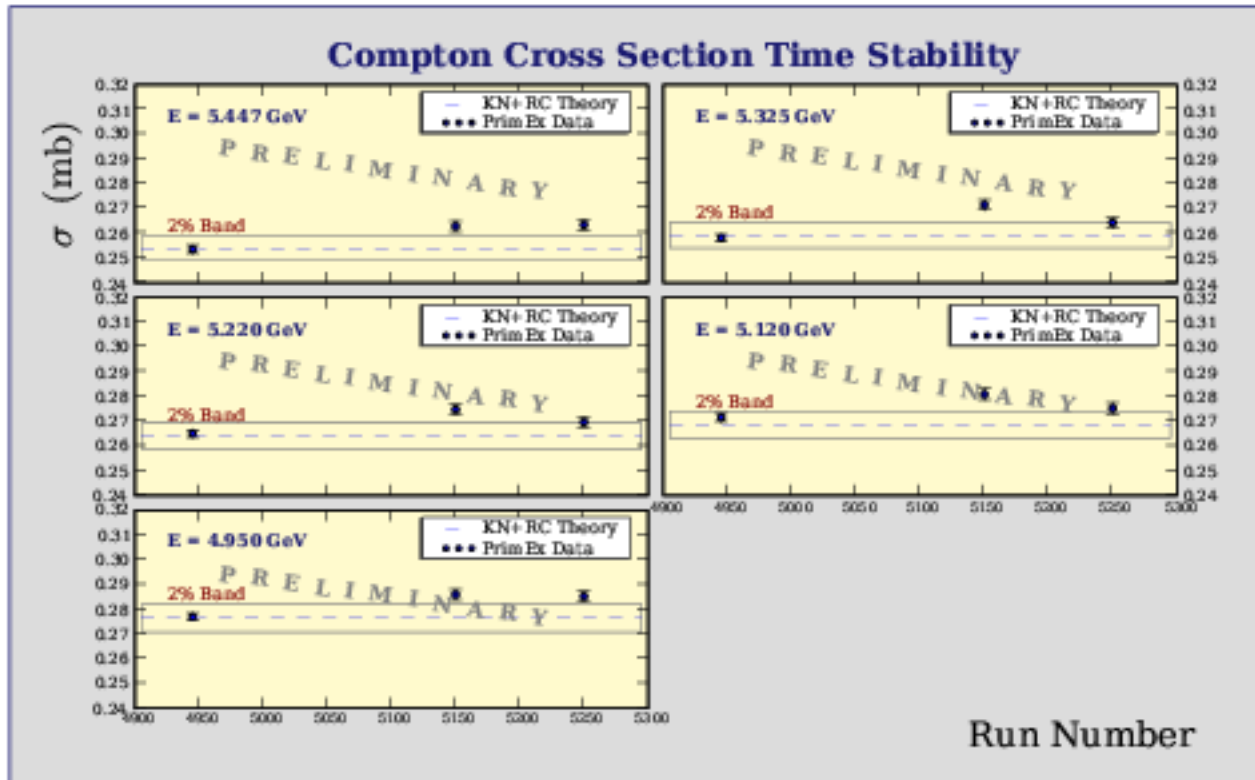


Figure 55: Total Compton cross sections change over the run numbers.

6 Plans for a future run

6.1 New improvements

6.2 Run time and schedule

Calibration and setup checkout	6 days
TAC (normalization) runs	1 day
Empty target (both Compton and π^0)	2 days
Compton and e^+e^-	4 days
^{208}Pb production running	6 days
^{12}C production running	7 days

7 Summary

We are requesting the continued support of the Jefferson Laboratory management for our efforts to perform a precision test of the axial anomaly in quantum chromodynamics. The fundamental importance of this experiment is evidenced by the fact that in anticipation of the results, three independent theoretical calculations on the decay rate have been performed. The calculations based on both next-to-leading order chiral theory and QCD sum rules have indicated an increase in the width from the leading order. In our view, this provides an in-

creased impetus to perform a measurement of this width with a precision commensurate with the theoretical knowledge. The PrimEx Collaboration is at present the only collaboration in a position to perform these measurements.

The Collaboration has designed, developed and constructed a multi-million dollars experimental setup which was commissioned during the first PrimEx run in 2004. The preliminary result from this data set has reached the error bar of $\sim 3\%$ on the π^0 lifetime. The analysis result indicates that the collaboration has the capability to control the systematic error. In order to reach our final goal of 1.4% precision, we are requesting for n days of 6 GeV beam time in Hall B. This will be one of very few fundamental tests of QCD can be performed at low energy region.

References

- [1] See *e.g.* Dynamics of the Standard Model, J.F. Donoghue, E. Golowich, and B.R. Holstein, Cambridge University Press (1992).
- [2] J.S. Bell and R. Jaciw, Nuovo Cimento 60A, 47 (1969). S.L. Adler, Phys. Rev. 177, 2426 (1969).
- [3] R.M. Barnett *et al.*, Review of Particle Physics, Phys. Rev. D54,1 (1996).
- [4] J. Bijnens, A. Bramon and F. Cornet, Phys. Rev. Lett. 61 (1988) 1453.
- [5] J.F. Donoghue, B.R. Holstein, Y.C.R. Lin, Phys. Rev. Lett., vol. 55, (1985), 2766; J.F. Donoghue, B. Wyler, Nucl. Phys., B316, (1989), 289.
- [6] H. Leutwyler, Phys. Lett. B378 (1996) 313 and hep-ph/9602255.
- [7] J. L. Goity, A. M. Bernstein, J. F. Donoghue, and B. R. Holstein, manuscript in preparation; J. L. Goity, talk at Baryons 2002.
- [8] B. Ananthanarayan and B. Moussallam, preprint hep-ph/0205232.
- [9] B.L. Ioffe and A.G. Oganesian, Phys. Lett. B647, (2007) 389.
- [10] H. Leutwyler, private communication.
- [11] B. Moussallam, Phys. Rev. D51 (1995) 4939.
- [12] G. von Dardel *et al.*, Phys. Lett., vol. 4, no. 1, (1963), 51.
- [13] D.A. Williams *et al.*, Phys. Rev. D, vol. 38, no. 5, (1988), 1365.
- [14] H.W. Atherton *et al.*, Phys. Lett., vol. 158B, no. 1, (1985), 81.
- [15] H. Primakoff, Phys. Rev. 81, 899 (1951).
- [16] A.M. Bernstein, Nucl. Phys. A623 (1997) 178c.

- [17] G. Bellettini *et al.*, *Il Nuovo Cimento*, vol. 66, no. 1, (1970), 243.
- [18] V.I. Kryshkin *et al.*, *Sov. Phys. JETP*, vol. 30, no. 6, (1970),1037.
- [19] G. Bellettini *et al.*, *Il Nuovo Cimento*, vol. 40, no. 4, (1965), 1139.
- [20] A. Browman *et al.*, *Phys. Rev. Lett.*, vol. 32(1974) 1067.
- [21] A. Browman *et al.*, *Phys. Rev. Letts.*, vol. 33, no. 23, (1974), 1400.
- [22] Available at the PrimEx web site: <http://www.jlab.org/primex/>
- [23] A. Gil and E. Oset, *Nucl. Phys. A580*, (1994) 517.
- [24] K. Mork and H. Olsen, *Phys. Rev.*, vol 140, number 6B, (1965), B1661.
- [25] Compact Muon Solenoid Technical Proposal, CERN/LHCC 94-38, LHCC/P1, (1994).
- [26] R.Y. Zhu, *et. al. IEEE Transactions on Nuclear Science*, v.45, no.3,(1998).
- [27] PrimEx Conceptual Design Report, 2000 (<http://www.jlab.org/primex/>).
- [28] Compact Muon Solenoid Technical Proposal, CERN/LHCC 94-38, LHCC/P1 (1994).
- [29] K. Mengel *et al. IEEE Trans. Nucl. Sci.* 45, 681-685 (1998).
- [30] R.Y. Zhu, *et al. IEEE Trans. Nucl. Sci.* 45, 686-691 (1998).
- [31] A. Gasparian, *Calorimetry in Particle Physics*, 208-214, Pasadena 2002.
- [32] A.V. Dolgoplov, *et al. Preprint IHEP*, IHEP-98-25, Protvino (1998)
- [33] S. Danagoulian, *The Light Monitoring System*, PrimEx Note 53.
- [34] O. Klein and Y. Nishina, *Z. Phys.*, 52, 853 (1929).
- [35] I. Tamm, *Z. Phys.*, 62, 545 (1930).
- [36] I.M. Brown and R.P. Feynman, *Phys. Rev.*, 85, 231(1952).
- [37] Till B. Anders, *Nucl. Phys.*, 87, 721 (1967).
- [38] K.J. Mork, *Phys. Rev.*, A4, 917 (1971).
- [39] F. Mfandl and T.H.R. Skyrme, *Proc. R. Soc. London*, A215, 497 (1952).
- [40] M. Ram and P.Y. Wang, *Phys. Rev. Lett.*, 26, 476 (1971); *ibid.* 26, 1210(E)(1971).
- [41] A. H. Compton, *Bull. Natl. Res. Counc. (U.S)* 20, 19 (1922); *Phys. Rev.*, 21, 483 (1923).
- [42] G. Bellettini *et al.*, *Il Nuova Cimento*, 66, no. 1, 243 (1970).
- [43] A. Browman *et al.*, *Phys. Rev. Lett*, 33, 1400 (1974).

[44] Mykhailo Konchatnyi, PrimEx Note 37, <http://www.jlab.org/primex/>.

[45] A. Tkabladze, M. Konchatnyi, and Y. Prok, PrimEx Note 42, <http://www.jlab.org/primex/>.

8 Appendix I: Previous Experiments

8.1 The direct method

A direct measurement of the π^0 lifetime can be made by observation of the decay distance between the production and decay points. This has proven difficult because of the high spatial resolution which is required due to the short lifetime, $\tau \simeq 10^{-16}$ sec. To be able to discern distinct production and decay points, one must take advantage of relativistic time dilation to have the pion survive long enough in the laboratory frame. Additionally, good knowledge of the energy distribution of the produced pions is necessary in order to extract the lifetime via this method.

The most recent result employed direct method was carried out at the CERN SPS in 1985 (shown in figure 1). In this experiment, a 450 GeV/c proton impinged upon two tungsten foils whose separation was variable. The first foil served as the π^0 production target, and the second foil converted the π^0 decay photons to electron-positron pairs, and the positrons were subsequently detected. By measuring the positron rates for three different foil spacings ranging from 5 to 250 μm , the authors were able to determine the lifetime. The dominant systematic errors arise from uncertainties in the π^0 spectrum which was not measured but was assumed to be the arithmetic mean of the π^+ and π^- spectra. In addition, corrections had to be made for the Dalitz decay of the π^0 's, conversion of the photons in the π^0 production target, prompt positron and photon production, and positrons from the decay of η 's. A pion lifetime of $\tau_{\pi^0} = (0.897 \pm 0.022 \pm 0.017) \times 10^{-16}$ seconds was reported[14], corresponding to a width of $\Gamma_{\pi^0} = (7.34 \pm 0.18 \pm 0.11)$ eV.

It is interesting to note that this experiment, the most precise of those performed to date, gives a result which is smaller than the leading order chiral anomaly prediction[1, 2]. Furthermore, with the latest calculations based on both next-to-leading order chiral theory and QCD sum rules described above, the discrepancy between this measurement and theory widens to more than three standard deviations. The experiment proposed here will directly address this discrepancy.

8.2 Measurements using $\gamma\gamma$ collisions

The π^0 width has been measured using electron-positron collisions at DESY via $e^+e^- \rightarrow e^+e^-\gamma^+\gamma^- \rightarrow e^+e^-\pi^0 \rightarrow e^+e^-\gamma\gamma$ [13]. The incident leptons are scattered at very small angles and are not detected in the final state. In so doing, they radiate quasi-real photons that couple to the π^0 which is subsequently identified in an invariant $\gamma\gamma$ mass spectrum. The photons were detected using the Crystal Ball detector which consists of a large array of NaI(Tl) crystals providing 93% solid angle coverage. Contributions to the systematic error included luminosity normalization, detector efficiencies, cosmic ray rejection, and beam-gas collisions. The latter effect arises from the production of π^0 's via the interaction of

the leptons with the residual gas in the beam pipe. The resulting width obtained was $\Gamma_{\pi^0} = (7.7 \pm 0.5 \pm 0.5) \text{ eV}$, very close to the prediction of the anomaly but with a relatively large error. The value obtained in this experiment is the same as the Particle Data Book average but was not included in this average[3].

8.3 Measurements using the Primakoff effect

The Primakoff effect, *i.e.* photopion production from the Coulomb field of a nucleus[15], has been used in a number of experiments to study the π^0 lifetime [43, 42, 18, 19]. The production of π^0 's in the Coulomb field of a nucleus by real photons is essentially the inverse of the decay $\pi^0 \rightarrow \gamma\gamma$, and the cross section for this process thus provides a measure of the π^0 lifetime.

Using bremsstrahlung beams of energy 4.4 GeV and 6.6 GeV at Cornell, Browman *et al.*[43] measured the Primakoff cross sections on several nuclei, and obtained a total decay width of $\Gamma_{\pi^0} = (8.02 \pm 0.42) \text{ eV}$. However, as was pointed out in [16, 13] the quoted error, does not have any contribution from uncertainties in the luminosity or detection efficiency (see table 1 of [43]), and is an underestimate. An analogous measurement of the η width[20] using the Primakoff effect employing a very similar setup and analysis procedure is not in agreement with other experiments.

The other two Primakoff measurements shown in figure 1 were performed with bremsstrahlung beams of 1.5 and 2.0 GeV at DESY[42] and 1.1 GeV at Tomsk[18]. From figure 1 it can be seen that the DESY measurement is high compared to the theoretical prediction and the Particle Data Book average. Although both of these measurements have relatively large errors they were included in the Particle Data Book average[3]. An older Primakoff experiment performed with 0.95 and 1.0 GeV bremsstrahlung beams at Frascati[19] has not been included in the Particle Data Book average and is not shown in figure 1.

In view of the strong interest in the subject, the dispersion of the previous results, and the recent availability of high intensity, high energy tagged photon beams, a high precision, state-of-the-art measurement of the π^0 lifetime is needed. In past several years, PrimEx collaboration has developed an experimental setup combining existing Hall B tagged photon facility at TJNAF with a newly developed a state-of-the-art, high resolution electromagnetic calorimeter. It will enable a measurement which will offer three distinct advantages over previous measurements involving bremsstrahlung beams: (1) the quasi-monochromatic nature of the tagged beam will enable a clean kinematical separation of the Primakoff mechanism from various background processes, (2) the tagging technique will enable significantly better control of systematic errors associated with the photon flux normalization, and (3) high resolution and high efficiency electromagnetic calorimeter will enable precise measurements on the invariance mass and production angle of the π^0 's. The first PrimEx experimental data set was collected in Hall B in fall 2004. The preliminary result is $\Gamma(\pi^0 \rightarrow \gamma\gamma) = 7.93 \pm 2.1\%(\text{stat}) \pm 2.0\%(\text{sys}) \text{ eV}$. More beam time is requested in this proposal to reach our final goal of $\sim 1.4\%$ precision.

9 Appendix II: Systematic Effects Relating to Photon Flux Determination

9.1 Effects of incident electron beam intensity on absolute tagging ratios

Due to the technical limitations of the TAC the absolute tagging ratios can be measured only at beam intensities which are $\sim 10^3$ times lower than the intensity of a regular production run. It is important to demonstrate that the tagging efficiencies obtained at beam intensities of $\sim 80\text{pAmps}$ are valid when applied to the data collected at the high beam intensities of about 80 to 130 nAmps . To investigate this, during our running period in Fall of 2004 we had normalization runs with various beam intensities (40 - 120 pAmps).

Figure 56 (top) shows the absolute tagging ratios as a function of T-counter number measured at different beam intensities. An artificial shift was introduced on the horizontal axis in order to be able to distinguish the different measurements. As a result, one has 11 groups of 4 points (one group per T-counter). The weighted average was calculated for each of the 11 groups. Figure 56 (bottom) shows the percent deviation of each measurement from the mean value for the relevant group. No noticeable systematic dependence of tagging ratios on the incident beam intensity was detected when varying the beam intensity from 40 pAmps to 120 pAmps .

9.2 Effects of collimator size

A decision was made for *PrimEx* to run with very loose collimation of the bremsstrahlung photon beam to cut out the beam halo. Together with careful monitoring of the beam position, collimation should increase the stability of the luminosity by keeping the photon beam focused at one spot on the target and thus reducing the effects of possible nonuniformity of the target thickness.

Two different sizes of copper collimators were available for this purpose. In Figure 57 (top) the relative tagging ratios are plotted versus T-counter ID for data taken with 2 different collimators. For reference purposes a result with no collimation is also plotted. For these measurements, the statistical error on each point is on the order of 0.15%. It is easy to see from Figure 57 (bottom) that the 12.7 mm collimator cuts out $\sim 1\%$ of the photon beam and 8.6 mm collimator cuts out $\sim 4\%$ of the photon beam.

9.3 Effects of collimator position misalignment

Figure 58 shows the position of the collimator on its ladder versus run number. One can easily see that the entire running period can be divided up on two groups of runs. The group 1) with run numbers from 4100 to 4295 with collimator at 7.075 in and the group 2) with run numbers from 4502 to 5447 with collimator at 7.02 in . Keeping in mind the required precision of 1% on the photon flux, it is important to investigate the extent to which the tagging ratios are affected by this shift.

The tagging ratios measured for 5 different positions are shown on Figure 59 (top). Figure 59 (bottom) shows the percent deviation of tagging ratios, measured at different

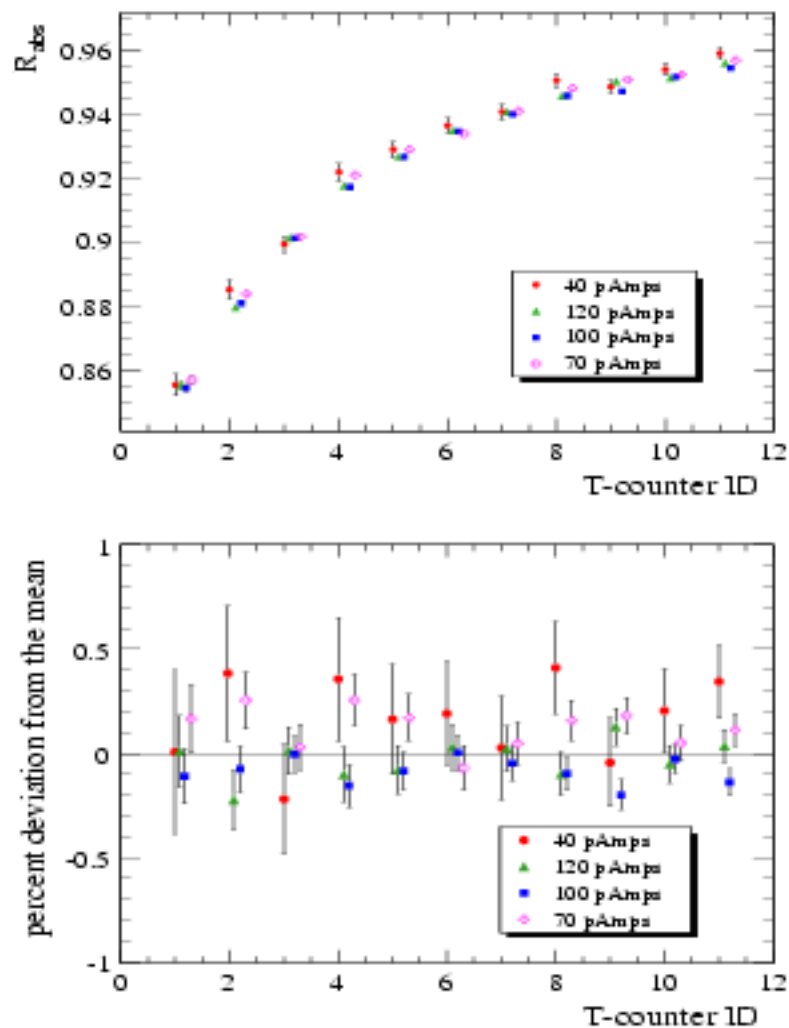


Figure 56: (top) Absolute tagging ratios plotted as a function of T-counter number for runs with different beam intensities, (bottom) The percent deviations from the mean for tagging ratio measurements made at different beam intensities for the first 11 T-counters.

positions of the collimator, from the value which was measured with the collimator in its nominal position (*i.e.* at $7.02in$). From Figure 59 (bottom) one can easily see that the shift in collimator position from $7.02in$ to $7.15in$ ($\sim 3.3mm$) lowers absolute tagging ratios by about 0.34% , hence if needed runs 4549, 4326, 4327 can all be used when calculating the final tagging ratios to reduce the the statistical error. One can also notice that larger shifts in collimator position result in $\sim 1.2\%$ and more reduction of R_{obs} .

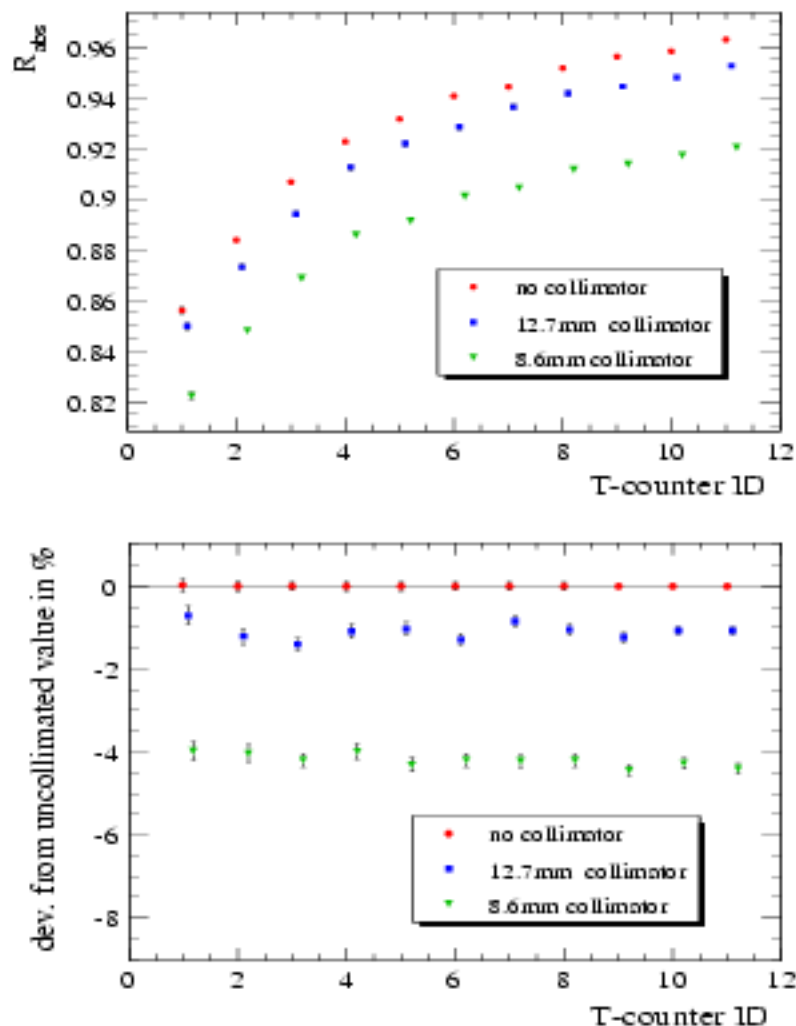


Figure 57: (top) R_{obs} , measured for 3 different collimator sizes, (bottom) Percent deviation from the uncollimated value.

9.4 Effects of HyCal scraping due to beam mis-steering (uncollimated beam)

As described in Section ?? the space between the Pair Spectrometer dipole vacuum window and the face of HyCal is taken up by a helium bag. The HyCal has a central opening to allow the uninteracted beam particles to pass through. A Gamma Profiler (GP) was installed directly behind the calorimeter to monitor the shape and the position of the photon beam during the experiment. Ideally one would place the TAC right at the position of the target but given the technical constraints in case of PrimEx, the TAC was mounted on the same moving platform as the GP behind HyCal and was placed in the path of the photon beam interchangeably with the GP to perform a normalization run. In this configuration the photons

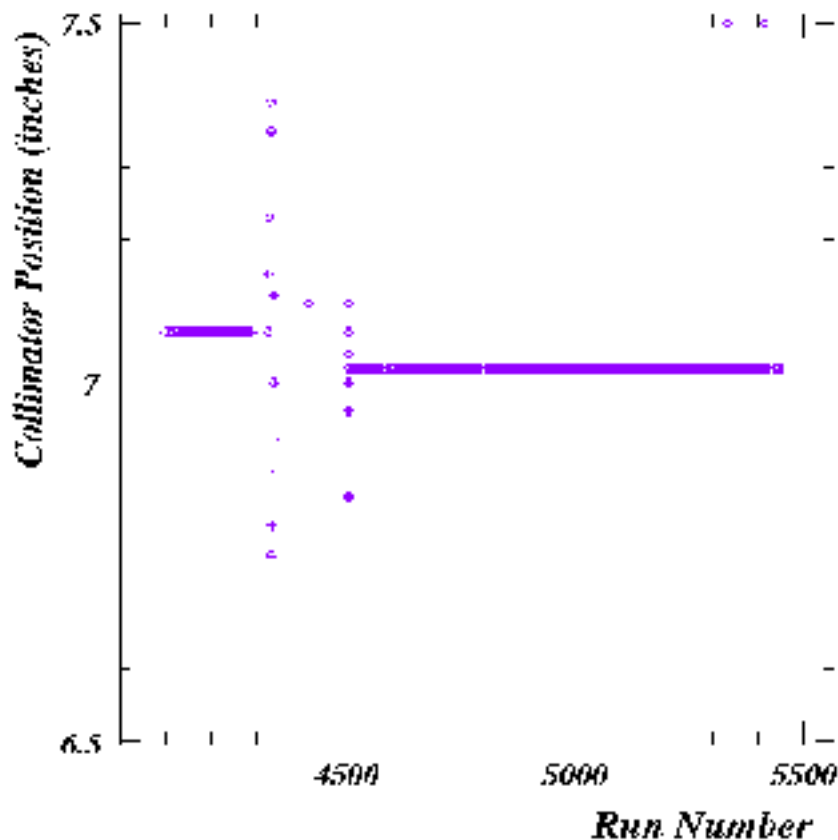


Figure 58: collimator position vs. run number.

must travel through a $4.15 \times 4.15 \text{cm}^2$ central opening in HyCal (see Section ??) before they can be registered in the TAC. Consequently it is necessary to evaluate to what extent the size of the HyCal central opening and the alignment of the photon beam with respect to the HyCal axis affect the results of normalization runs. For this purpose the direction of the photon beam was purposefully altered and the tagging ratios were measured. To allow for larger artificial shifts in beam position the collimator was retracted during this study. Due to the fact that this investigation was done with uncollimated beam it places an upper limit on the amount of the photon beam that can be cut by HyCal due to scraping. Because the GP was mounted on the same moving platform as the TAC, photon beam position measurements were possible only before and after a normalization run. In light of this, the study described in this section should be considered only as qualitative exercise.

It was determined that in the absolute coordinate system of the GP, the nominal photon beam position is: $X_{av} = -0.83 \text{mm}$ and $Y_{av} = -1.45 \text{mm}$. Figure 60 (top) shows several measurements of tagging ratios with different beam positions. Run # 4338 was taken with the beam at its nominal position. For run # 4340 the beam was steered a little over 5mm in positive Y direction to $(-0.93, 4.09)$. For run # 4341 the beam was at $(-6.54, -1.23)$. During run # 4342 beam was at $(-9.45, -1.52)$ - i.e. about 8.5mm off of its nominal

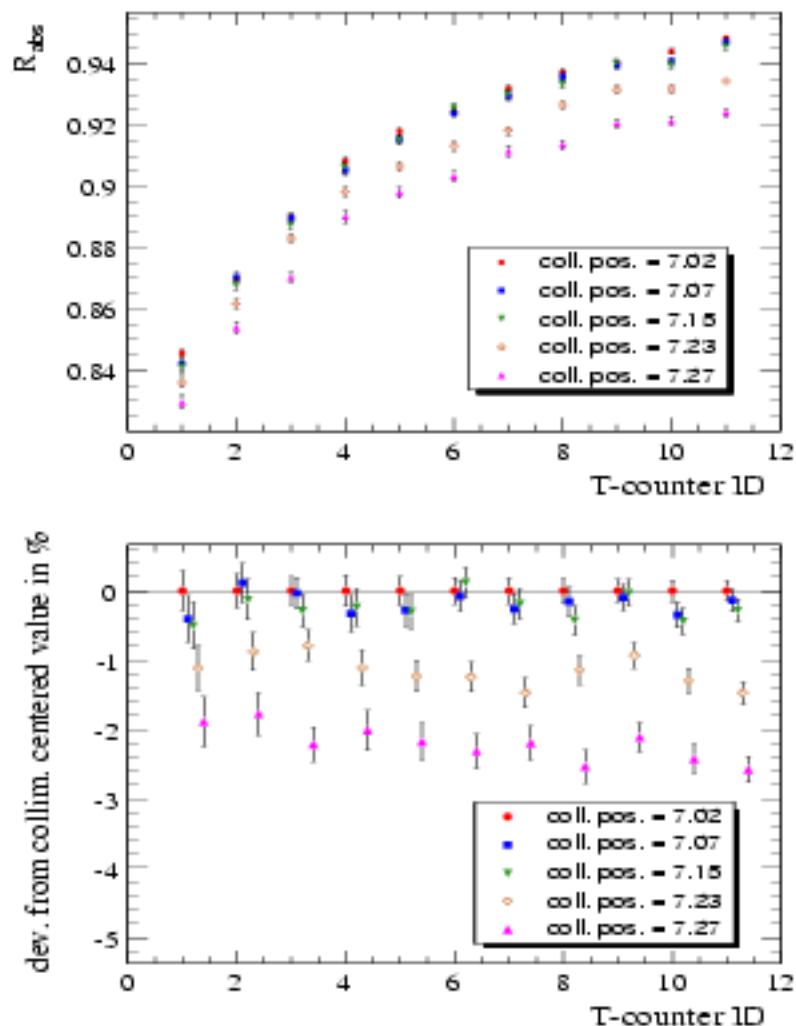


Figure 59: (top) R_{obs} , measured for 5 different collimator positions measured in inches. (bottom) Percent deviation from the measurement taken with collimator in its nominal position (7.02in).

position. For run # 4343 beam was at (5.12, -1.44) - *i.e.* about 6mm off of its nominal position.

This qualitative study indicates that the HyCal and the beam were not positioned ideally with respect to each other. Runs # 4342 and 4343 indicate that a $\sim 8.5mm$ shift in the beam position in negative direction has the same effect on the tagging ratios as a $\sim 6mm$ shift in the positive direction along the X axis. Also runs # 4340 and 4341 indicate a slight increase ($\sim 0.23\%$) in tagging ratios when the beam is steered 5mm in positive Y direction or 5mm in negative X direction.

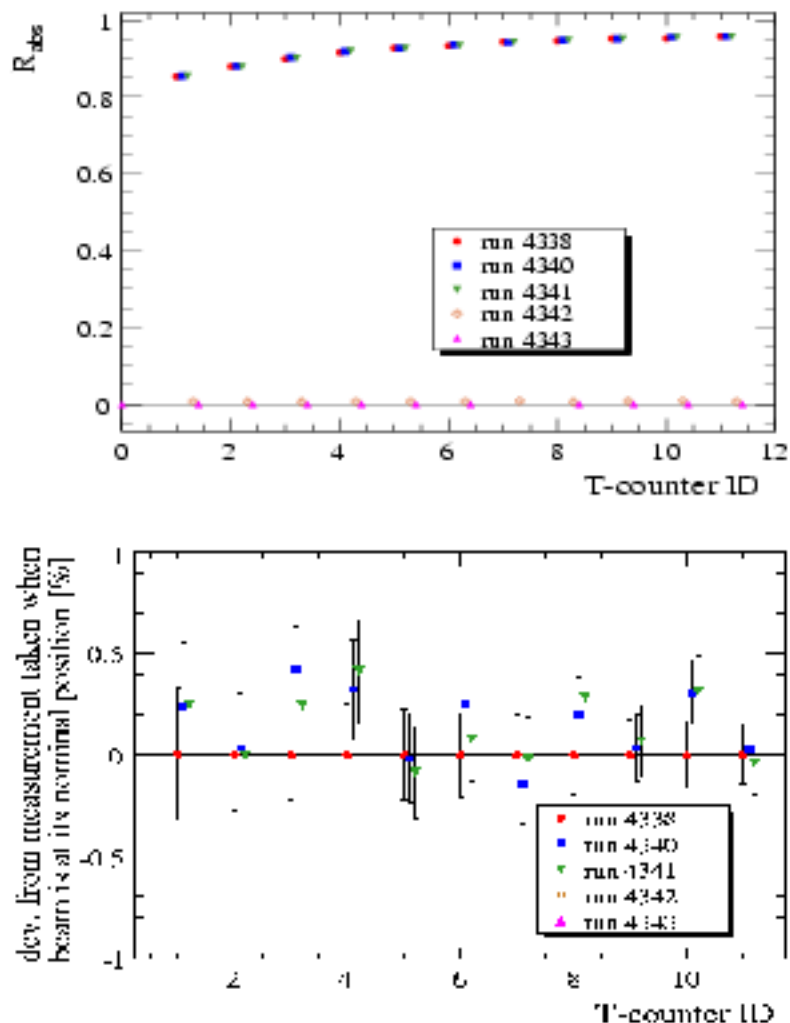


Figure 60: (top) R_{abs} measured for 5 different beam angles. (bottom) Percent deviation from the uncollimated value.

9.5 Long and short term reproducibility with uncollimated beam

To test our ability to perform a consistent measurement of the absolute tagging ratios, $R_{absolute}$, we had back-to-back normalization runs which were taken only 20 – 25 minutes apart. The pair spectrometer magnet was operating at ~ 900 Amps.

As it can be seen from Figure 61, the study shows that all 4 runs agree within the limits of required precision and statistical errors.

Figure 62 (top) shows the absolute tagging ratios measured for the first 11 T-counters. These runs were taken ~ 4 and half hours and 5 days apart from each other. Figure 62

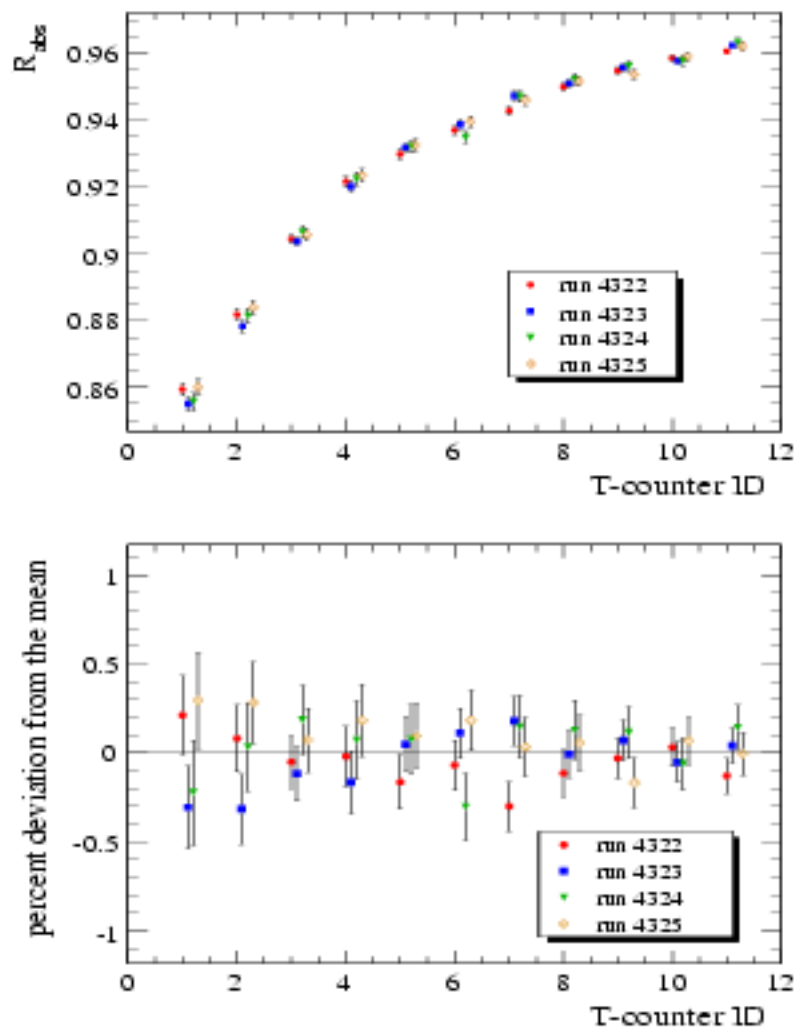


Figure 61: (top) R_{abs} measured for 4 consecutive runs. (bottom) Percent deviation from the mean.

(bottom) shows the percent deviation of the tagging ratio for each T-counter from the relevant average value. The statistical error for each point is on the order of 0.2%. As seen from the plots, all three measurements are in very good agreement with each other (better than 0.3%). Note that since since all three measurements were taken with different settings of Pair Spectrometer dipole, this study also shows that there is no detectable dependence of absolute tagging ratios on the magnetic field of the PS dipole when using an uncollimated photon beam.

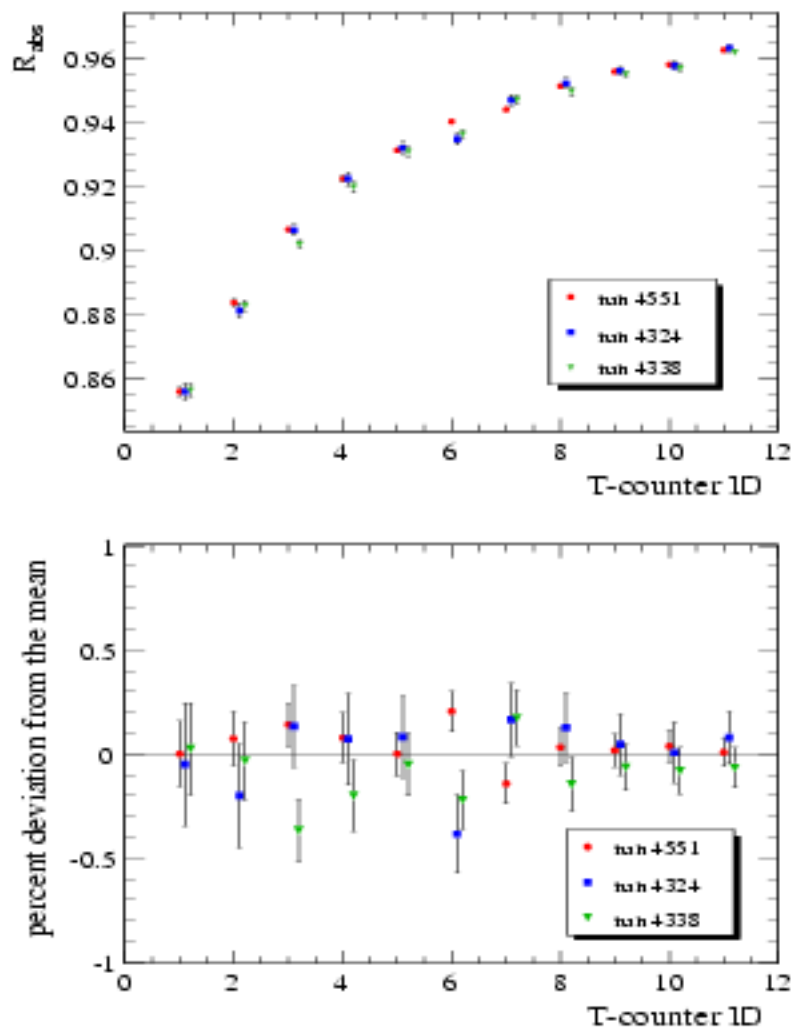


Figure 62: (top) R_{obs} measured for 3 runs which were spread in time during our data taking. (bottom) Percent deviation from the mean.

9.6 Effects of the PS dipole field with collimated beam

As was already demonstrated in Section 9.5, the PS dipole field has no measurable effect on the tagging efficiencies in the case of an uncollimated photon beam. Since, due to technical difficulties with the PS power supply, the normalization runs were performed at different values of the magnetic field of the PS dipole, and the production data for PrimEx were taken with a 12.7mm collimator, it is important to investigate the effect of the magnetic field on the tagging ratios measured for a collimated beam.

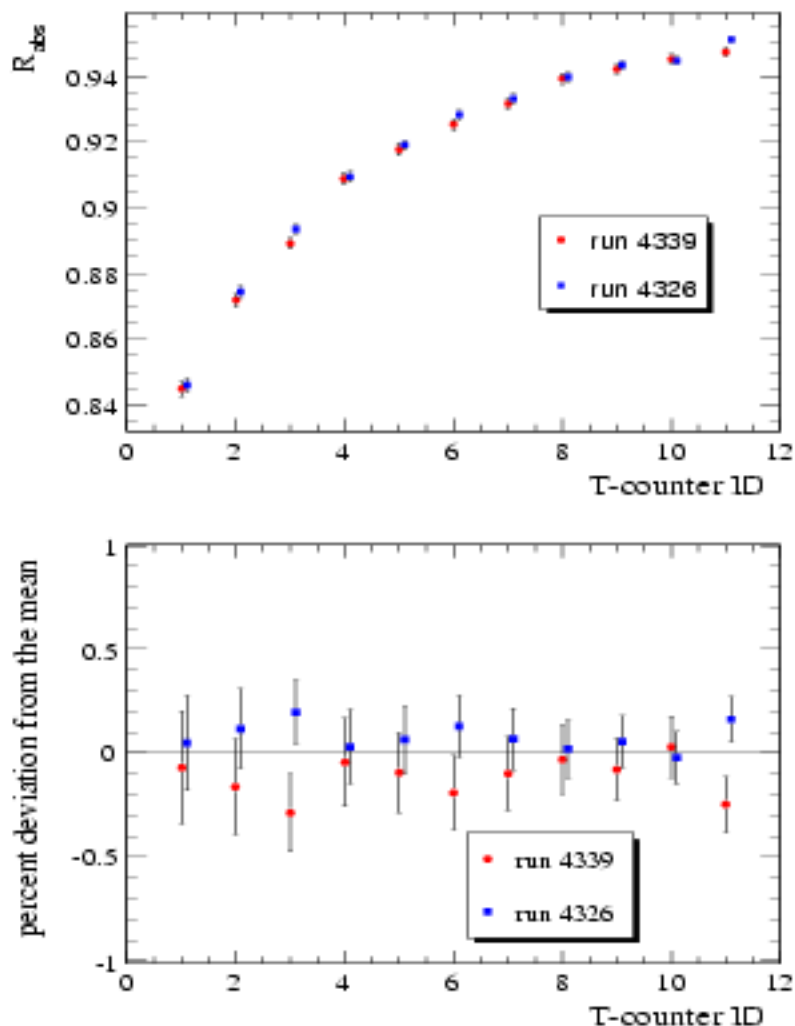


Figure 63: (top) R_{obs} , measured for 2 runs which were taken with different settings of PS dipole magnet. (bottom) Percent deviation from the mean value.

9.7 Absorption in the target

Some of the photons are absorbed in the target without producing a π^0 . Special TAC runs with a carbon target placed in the beam were performed to study this effect. Figures 64 and 65 show a comparison of tagging efficiencies measured for target in runs to those measured for target out runs for measurements performed without and with photon beam collimation. Both studies yield consistent results indicating that $\sim 3\%$ of photons are lost in the target.

Since PrimEx is aiming for a $\sim 1.5\%$ level absolute cross-section measurement one has to correct the yields for absorption of photons in the target. The main reaction of interest for PrimEx, ($\pi^0 \rightarrow \gamma\gamma$) and the consistency check reactions (Compton effect and e^+e^- production) are affected by the photon absorption in the target on different levels. In the

case of Compton and Primakoff effects not only the primary photon but also the secondary photons can be absorbed in the target. Since Compton scattering or π^0 -production can happen anywhere along the longitudinal direction of the target, the result of this study can be used to set an upper limit on the effect of photon absorption.

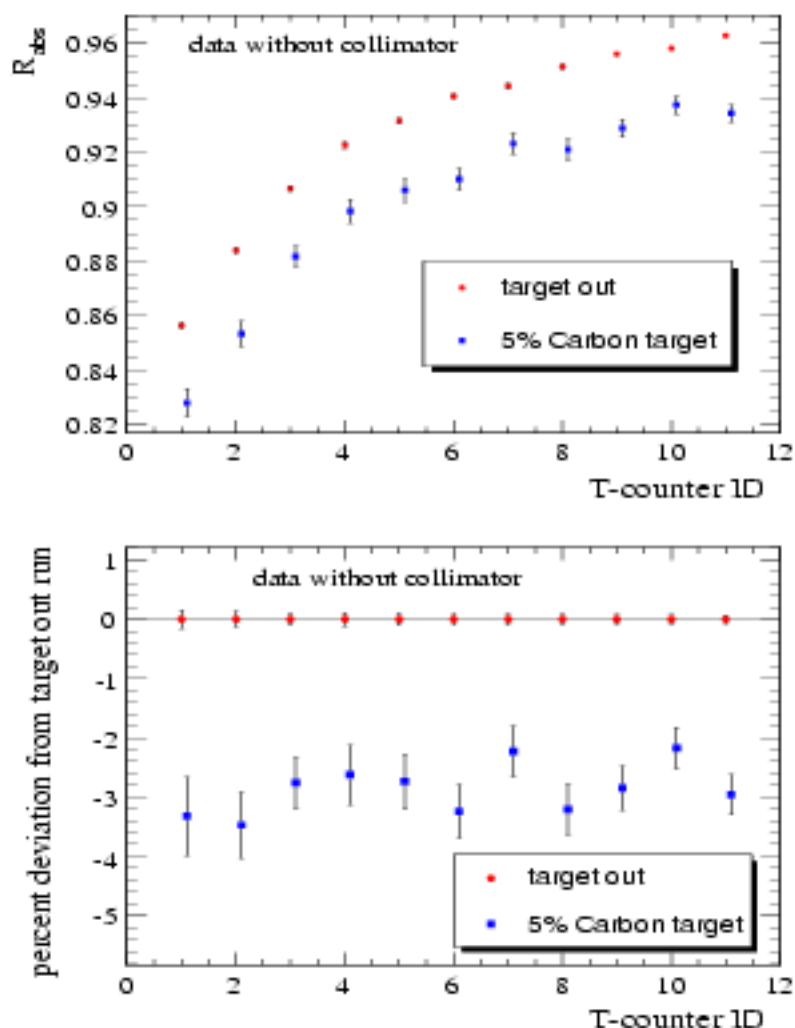


Figure 64: (top) R_{obs} measured for runs which were taken with target in and target out. (bottom) Percent deviation from the measurement obtained with physics target out; no photon collimation.

10 Appendix III: Target thickness determination

We propose to use two targets in this experiment, ^{12}C and ^{208}Pb . The carbon target is approximately 380 mil thick (5% R.L.) and uses Highly Ordered/Oriented Pyrolytic Graphite

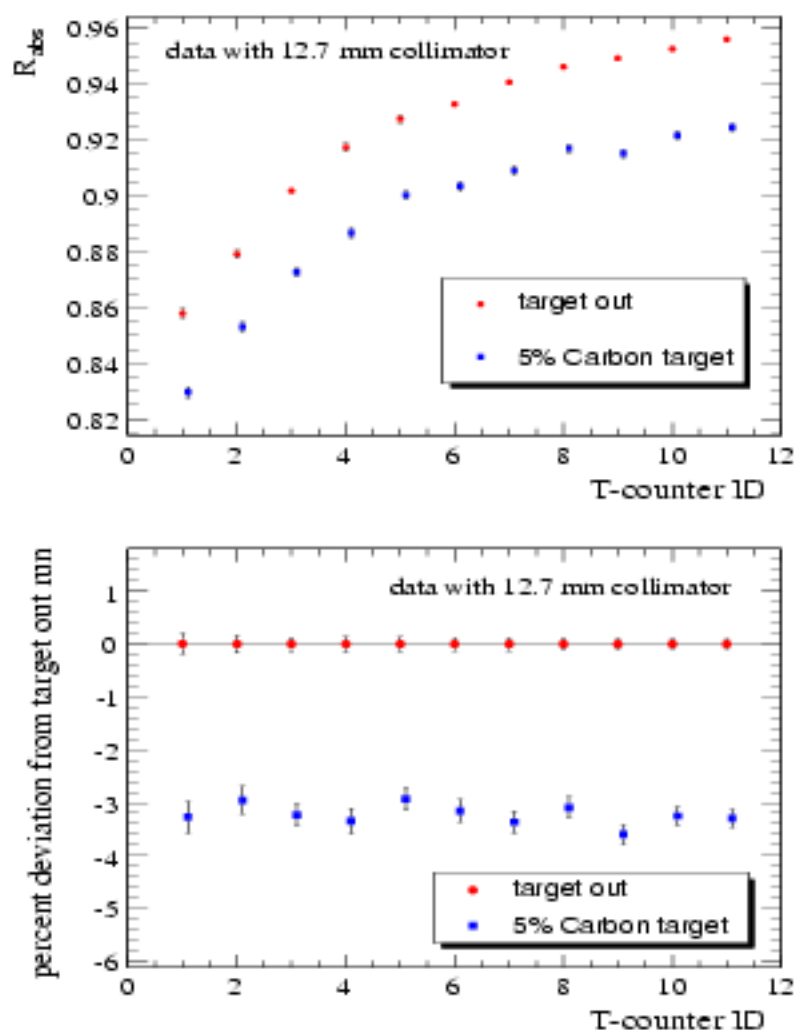


Figure 65: (top) R_{obs} , measured for runs which were taken with target in and target out. (bottom) Percent deviation from the measurement obtained with physics target out; with photon collimation.

(HOPG) as the target material. The lead target is a rolled metal target approximately 12 mils thick (5% R.L.) and uses 99% enriched ^{208}Pb as the target material. The uncertainties in the effective areal densities of the carbon and lead targets are 0.05% and 0.43%, respectively. Both targets were utilized in the first *PrimEx* run. In this section the methodology for mapping the effective areal densities of the targets (atoms/cm^2) and the estimated errors are described. Most details of the analysis can be found in *PrimEx* note #28.

A micrometer with precision of ± 0.05 mils was used to make a map of the thickness of the HOPG target. Figure?? shows the micrometer map points, and the measured thicknesses in the central region of the target are also shown. The thickness varies by approximately

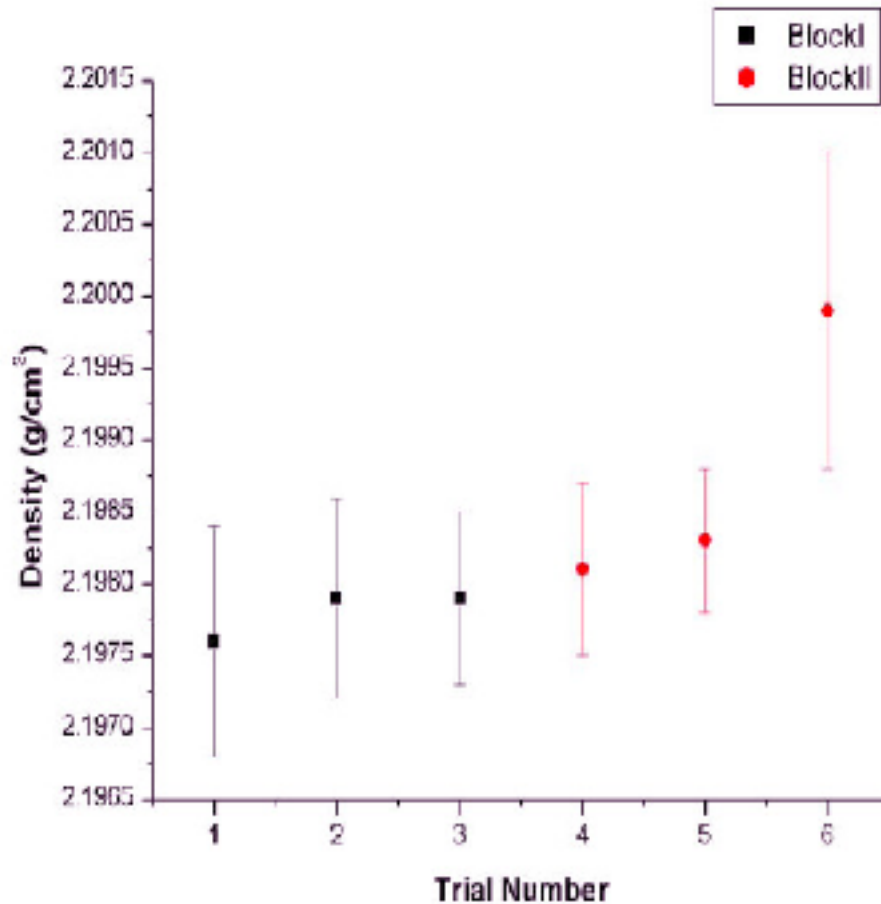


Figure 66: HOPG density measurements.

0.04% over the central region of the target. The mass density of the HOPG material was measured using the water immersion technique. HPLC grade water was used, which is submicron filtered, packed under inert gas, and has a maximum limit of impurities at 1 ppm. Corrections were made for the temperature dependence of the water density. A microgram scale was used to weight the target block in air and in the water. The mass densities of two identical HOPG blocks were measured three consecutive times, and the results are shown in figure 66. The HOPG mass density used in calculating the areal density of the target was the average of the first five measurements (trial #6 was excluded), and the error in mass density is taken from trial #3.

Two corrections were applied to ρT to obtain the effective areal density of the target. The first correction is for impurities in the target, which can produce neutral pions through the Primakoff process. The second accounts for the attenuation of the incident photon beam in the target. The NIST XCOM data base was used to calculate the effect of incident beam absorption. Magnetic Primakoff production from ^{13}C is very small compared to Coulomb Primakoff production, and can be neglected. The final result for the effective number of ^{12}C atoms/cm² in the target is: $N_{eff}(Z = 6) = 1.0461 \times 10^{23} \text{ atoms/cm}^2 \pm 0.05\%$

The lead target was manufactured by Oak Ridge National Laboratory, and is a rolled foil of isotopically enriched ^{208}Pb , with 99% purity. The thickness of the target is approximately 12 mils, which corresponds to 5% radiation length. Because the target is a thin foil that can be easily damaged, direct measurements of foil thicknesses using a micrometer were considered risky. For this reason, an alternative method was devised which utilized x-ray attenuation to measure the foil thickness. X-rays from the 60 keV line in ^{241}Am were collimated to a spot size approximately 2 mm in diameter. X-rays that passed through the target were detected in a 1 inch diameter NaI detector located behind the target foil. By comparing the attenuation of x-rays through the foil at various points, the thickness at these points can be determined. X-Y stepper motors were used to scan the lead target over the ^{241}Am source, and a map of x-ray attenuation versus target (x,y) was obtained. Two target scans were performed; the first was a run with 200 mil step sizes, and then a second run about a month later with 100 mil steps. Since the x-ray absorption constant for lead is not known with sufficient accuracy for our needs, the constant was measured at four off-center points on the target. This was done by taking x-ray attenuation and micrometer measurements at those points during the 200 mil and 100 mil step runs. Figure 67 shows the results of the study. For a given step size, the four measurements of x-ray absorption agree. However, there is a shift when comparing the results with the 200 mil step versus the 100 mil step size. To keep the analysis consistent, the 200 mil absorption constant was applied to the 200 mil step data, and the 100 mil absorption constant was applied to the 100 mil step data. The consistency of the analysis can be checked by verifying that the target thicknesses obtained in both scans agree within errors. The target thickness map from the 100 mil step scan is shown in Figure 68. The plot indicates a plateau near the center of the foil. The apparent increase in thickness at the very corners of the data is most likely caused by the target frame. Figures 69 and 70 show crosscuts through the lead target along the Y and X axes, respectively. Results from both the 100 mil and 200 mil step scans are shown on the plots, and there is good agreement between the two data sets. The crosscuts clearly indicate a plateau near the center of the target that extends out to a radius of 200 mil. During the 2004 Primex run, the target ladder was positioned so that the beam went through the center of the lead target to take advantage of the relatively uniform target thickness in this area of the target. The areal density of the lead target was calculated using the average of lead mass densities listed in the literature. Corrections were applied to account for the effects of impurities in the target, and for attenuation of the incident beam. The result is

$$N_{eff}(Z = 82) = 9.875 \times 10^{20} \pm 0.43\% \text{ atoms/cm}^2.$$

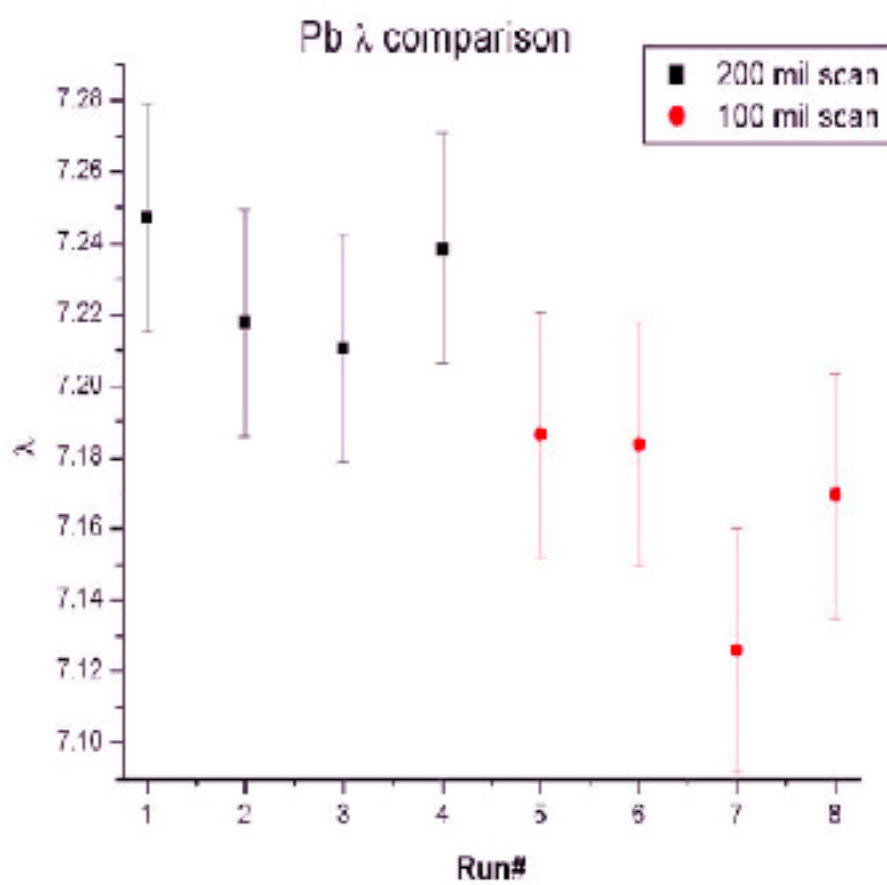


Figure 67: .

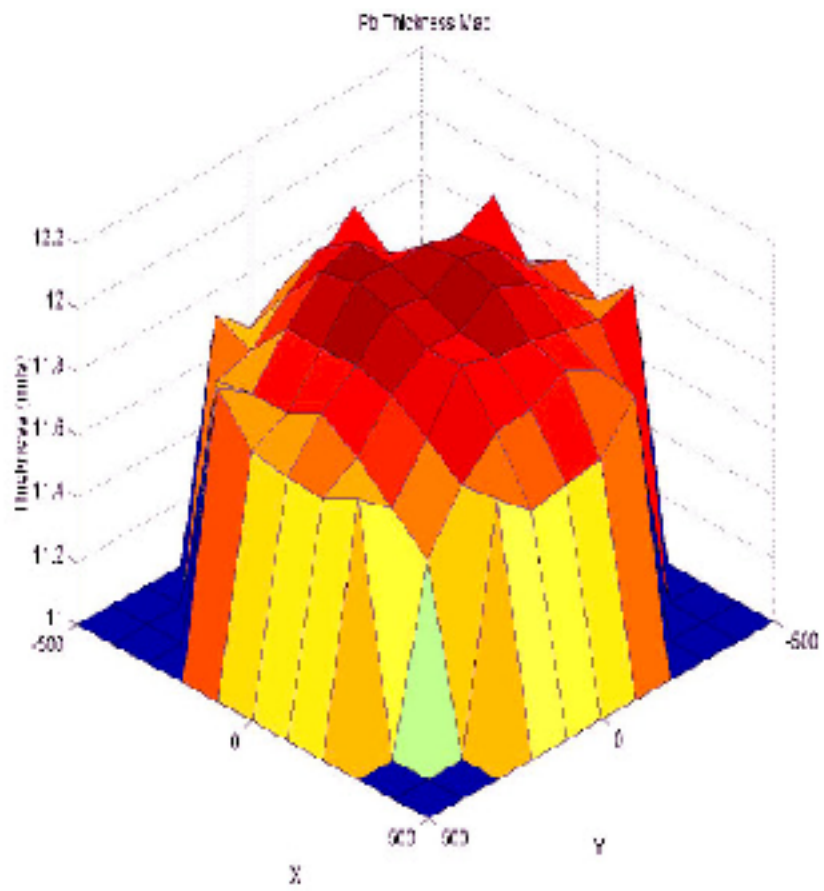


Figure 68: .

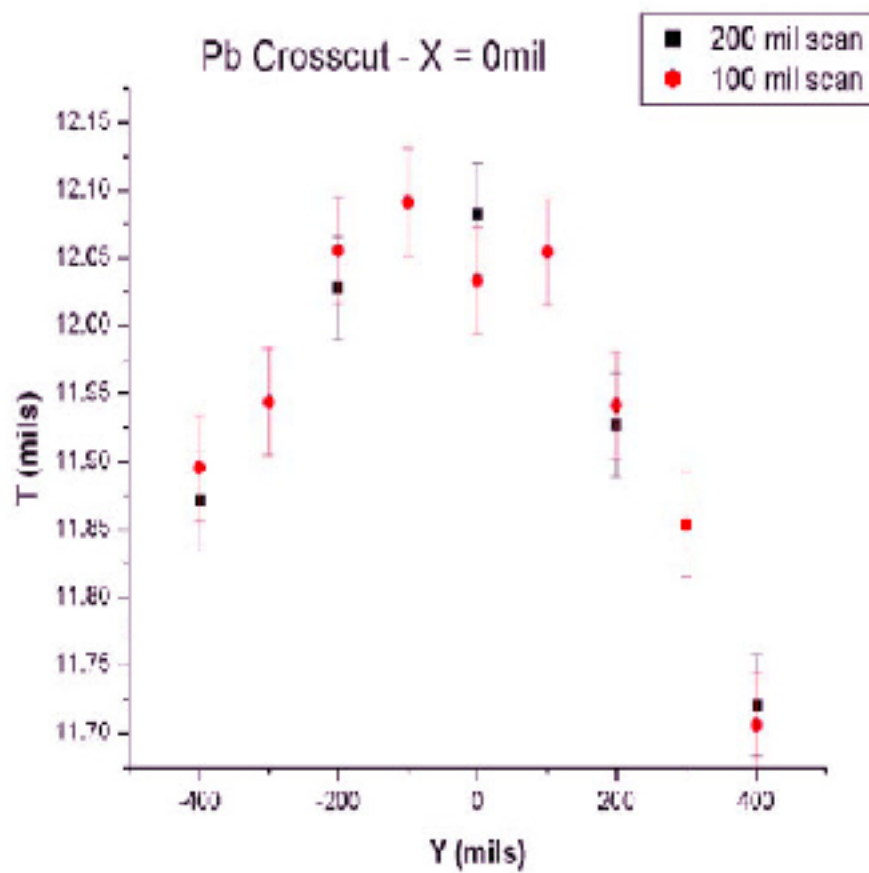


Figure 69: .

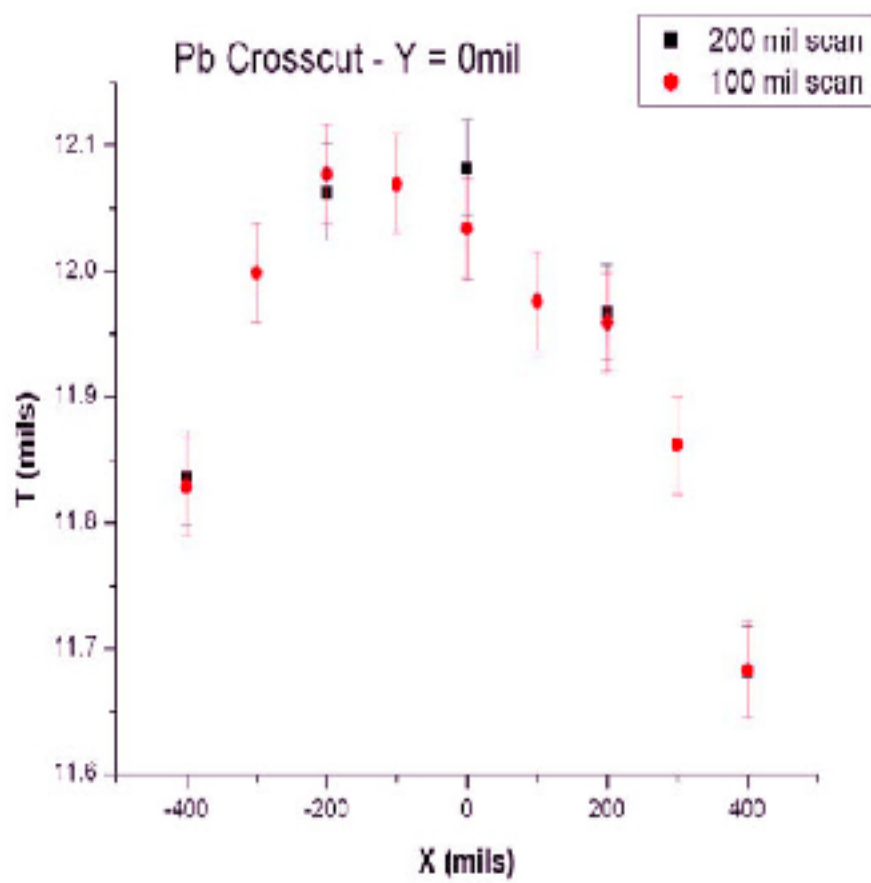


Figure 70: .